DEVELOPMENT AND EVALUATION OF A SPECT ATTENUATION CORRECTION METHOD USING AN OPEN TRANSMISSION SOURCE AND SCATTER CORRECTION.

by

Johannes Abraham van Staden

This thesis is submitted to meet the requirements for the degree Philosophiae Doctor (Ph.D.) in the Faculty of Health Science, Department of Medical Physics at the University of the Free State

June 2011

Promotor:	Dr. H du Raan
Co-promotor:	Prof A. van Aswegen

I declare that the thesis which is hereby submitted for the degree Philosophiae Doctor (Ph.D.) at the University of the Free State, is my own independent work and has not been handed in before for a degree at/in another university/faculty. I furthermore waive copyright of the thesis in favour of the University of the Free State.

Bloemfontein

August 2011

_____

Johan van Staden

DEDICATION

To my wife Annalene and daughter Inge

ACKNOWLEDGEMENTS

The acknowledgments have to be the most difficult for me to write, mainly due to the uncountable number of people who have helped and guided me.

Firstly, I would like to thank my promoter and co-promoter, Dr. Hanlie du Raan and Prof. Andries van Aswegen, for their guidance during my research and study. Their perpetual energy and enthusiasm in research had motivated me. In addition, they were always accessible and willing to help with the research. As a result, research life became more smooth and rewarding for me. I could not have imagined having better advisors and mentors for my study.

I would like to thank Prof. Charles Herbst and Dr. William Rae whose theoretical and practical knowledge of medical physics have been an invaluable resource. I would also like to express my gratitude to Prof. Thys Lötter for his continuous support, enthusiasm, and immense knowledge of medical physics.

Last but not the least, my wife Annalene and daughter Inge and the one above all of us, the omnipresent God, for answering my prayers for giving me the strength, thank you so much Dear Lord.

TABLE OF CONTENTS

LIST OF TABLES

Table

LIST OF FIGURES

Figure

LIST OF APPENDICES

APPENDIX

Chapter 1

Introduction

Nuclear medicine is a powerful tool for visualizing physiological functions or metabolism. The signal detected in a nuclear medicine scan originates from a three-dimensional radionuclide distribution of the organ of interest. The gamma camera which is used to record the three-dimensional radioactivity distribution is a two-dimensional detector. Two-dimensional planar imaging can be found in virtually every nuclear medicine facility. However, the three-dimensional structures in a two-dimensional planar image are superimposed and thus making diagnoses with planar imaging difficult. Rather than two-dimensional planar imaging, tomographic data acquired by rotating the gamma camera detector around the patient and collecting projection data from different views are used for reconstructing a three-dimensional image and is known as Single Photon Emission Computed Tomography (SPECT). Although SPECT imaging has certain advantages over planar imaging both imaging techniques suffer from image degradation due to physical limitations. The more important phenomena resulting in image degradation of planar as well as SPECT data include detector blur, photon scatter and photon attenuation.

Two major classes of image reconstruction algorithms that can be used for the reconstruction of emission tomography data exists, namely analytical and iterative methods. In the past the filtered back projection (FBP) method which is an example of an analytical method was often used for the reconstruction of emission data because it is relatively quick and easier to implement than iterative methods. A limitation of analytical methods is that they can yield inaccurate activity distributions due to assumptions that are made as part of the reconstruction process. An example of such an assumption is that the line of response for a collimator hole is an extended cylinder while the actual response for a collimator hole resembles a diverging cone. Filters that are incorporated in the reconstruction process also result in quantitative inaccurate results. Detector blur, photon attenuation and scatter are often ignored or handled incorrectly in analytical algorithms. It has been shown that iterative methods can drastically improve the

quality and quantitative accuracy of reconstructed images when these assumptions are omitted and detector blur, photon attenuation and scatter are compensated for. A number of iterative reconstruction algorithms are available and the choice of the algorithm is important. The maximum likelihood expectation maximisation algorithm has proven to be effective, but also to be too slow for routine use. Several methods have been proposed to speed up the algorithm (Hudson and Larkin, 1994; Byrne, 1996). Splitting up the measured dataset into different subsets and using only one subset per iteration can speed up the algorithm with a factor equal to the number of subsets (Hudson and Larkin, 1994). Since its introduction, the ordered subsets expectation maximization method (Hudson and Larkin, 1994) has become the most frequently used iterative reconstruction algorithm in SPECT.

Iterative reconstruction algorithms can be used to incorporate corrections for non-uniform attenuation, scattered radiation as well as collimator response in SPECT. Detector blur leads to poorer resolution with an increase in the source to collimator distance. Photon scatter results in energy loss and therefore a change in direction of the photon and hence an incorrect photon origin is reconstructed by the imaging system. Attenuation is defined as the reduction of the number of detected gamma rays due to photoelectric absorption and Compton scatter. Although attenuation is but one of the image degradations, it affects image quality severely and therefore receives much attention (King *et al.*, 1995; Bailey, 1998; Corbett and Ficaro, 2000; Hendel *et al.*, 2002). Photons with energy of 140 keV, originating from inside the body can be attenuated by as much as 25% before being detected by the gamma camera (Tsui *et al.*, 1994). Correction for attenuation is thus very important since it can improve quantitation accuracy as well as avoid image artefacts in SPECT reconstruction. This is especially relevant in bodily areas with non-uniform attenuation media such as the thorax. A quantitative accuracy of better than 10% can be obtained in planar imaging if scatter and uniform attenuation correction are applied to acquired data (Pereira *et al.*, 2010). On the other hand, incorrect compensation for photon attenuation may result in great inaccuracies in quantitative and qualitative SPECT data (Wackers, 1999; Celler *et al.*, 2005). Due to these improvements in the reconstruction algorithms and computer hardware, iterative reconstruction techniques are now routinely used in clinical SPECT.

Different attenuation correction procedures are available. The majority of procedures for attenuation correction in SPECT are applied either during or after the emission reconstruction. One well-known approach for attenuation correction is the method by Chang (1978) where a uniform attenuation medium is assumed and a constant attenuation coefficient is applied in the correction of the emission data. This is however not a valid assumption in the human body, especially in the thorax area with the presence of soft tissue, bone and lung tissue. In order to apply an appropriate attenuation correction it is necessary to know the attenuation coefficients in the body. The determination of an accurate, patient-specific attenuation coefficient map is fundamental in performing accurate attenuation correction. These attenuation coefficient maps can be obtained from transmission data. Transmission data is acquired using an external radiation source and an image is formed by the photons transmitted through the object of interest. For SPECT an attenuation coefficient map is obtained by means of transmission computed tomography (TCT). During TCT transmission data is acquired and reconstructed to produce the attenuation coefficient map. The map is then incorporated in the SPECT reconstruction process to compensate for photon attenuation. Attenuation coefficient maps can be determined by using transmission measurements with a Computed Tomography (CT) scanner which uses an X-ray tube or an external radionuclide transmission source (Zaidi and Hasegawa, 2003).

By using a CT scanner, attenuated X-rays passing through the body are collected at certain intervals around the patient. These acquired attenuated X-rays are used to reconstruct the attenuation coefficients. Attenuation coefficient maps can also be determined by using a radionuclide transmission source. Transmission tomography by means of radionuclides is similar to X-ray tomography whereby using an external radioactive source instead of an X-ray tube, an attenuation coefficient map can be reconstructed. Both CT as well as the external radionuclide source methods has certain advantages as well as limitations for the construction of attenuation coefficients.

With the goal of improving SPECT information, hybrid SPECT/CT systems were developed. These systems can provide anatomical as well as functional images of the patient in the same position and during a single procedure. The application of these systems in clinical use is twofold. The CT information can firstly be used to generate patient-specific attenuation coefficient maps in order to compensate for attenuation of emission photons. Secondly, additional anatomical information is obtained from the CT images. This anatomical information assists in the diagnosis of the patient studies. The first generation SPECT/CT systems used a low-resolution CT detector, since attenuation correction does not require high resolution CT information. However, newer SPECT/CT scanners have recently been expanded to include state of the art high resolution multi-slice imaging systems (Bocher *et al.*, 2000; Patton *et al.*, 2000) due to the benefit of additional anatomical information that is obtained.

Practical advantages of Hybrid SPECT/CT over transmission imaging with a radionuclide source for generating an attenuation coefficient map are the following:

(i) The photon fluency rate from the X-ray tube is several orders of magnitude higher than can be obtained from a radionuclide transmission source, resulting in low noise cross-sectional images in a very short imaging time.

(ii) The higher fluency rate from the X-ray tube allows the transmission data to be acquired after the patient is injected with the radiopharmaceutical. The gamma rays originating from the emission study do not influence the CT image.

(iii) The X-ray source does not decay and thus does not need frequent replacement.

(iv) The CT scanner produces transmission images of higher quality than that acquired from radionuclide transmission sources.

(v) Diagnostic quality images can be produced with the CT scanner that leads to additional diagnostic information of the patient.

Disadvantages that should be considered when CT information is used to generate attenuation coefficient maps of the patients are as follows:

(i) All studies with hybrid SPECT/CT systems are acquired sequentially as a result of the positioning of the SPECT and CT components which allow for possible image misalignment.

(ii) A CT system has a higher spatial resolution than SPECT systems and the reconstructed transmission image require down-sampling to the same image matrix size as the emission image.

(iii) A CT scanner gives a relatively high radiation dose to the patient in comparison to a transmission scan with a radionuclide. (Almeida *et al.*, 1998, Preuss *et al*., 2008)

(iv) CT projection data are obtained using a poly-energetic X-ray source. As the X-ray beam passes through the patient, a majority of the low energy photons are absorbed in the patient resulting in the ‘‘beam-hardening’’ artefact in which the raw values of the CT image are lower in the middle of an object than at the periphery, representing the higher mean energy and correspondingly lower attenuation coefficients obtained in thick body parts than those produced for thin regions of the body (Zaidi and Hasegawa, 2006).

(v) When CT data from a clinical scanner is used to obtain a patient-specific map of attenuation coefficients it is necessary to transform the CT image data so that it is expressed in terms of the linear attenuation coefficients and not Hounsfield numbers. This must be done for the energy of the emission radionuclide photon so that the attenuation data can be used to correct the emission data for photon attenuation (Zaidi and Hasegawa, 2006).

Radionuclide transmission systems have a number of limitations which include the following:

(i) Collimated radionuclide transmission systems require high source activity.

(ii) Complicated electronic equipment is required to separate transmission and emission images and can results in insufficient counting statistics in the transmission image (Zaidi and Hasegawa, 2003).

(iii) The source decays and requires frequent replacement which is dependent in the half life of the radionuclide that is being used.

Radionuclide transmission systems can overcome some of the limitations of hybrid SPECT/CT systems. Advantages of transmission imaging with a radionuclide source over hybrid SPECT/CT for generating an attenuation coefficient map are the following:

(i) Misalignment due to sequential imaging can be eliminated by simultaneous imaging with a radionuclide transmission system.

(ii) Image matrix size mismatch between transmission and emission imaging is eliminated by using radionuclide transmission systems.

(iii) X-rays emitted by CT are polychromatic and the CT numbers have to be converted to the gamma-ray linear attenuation coefficients by a table look-up method, which is not the case for attenuation maps acquired by radionuclide transmission sources. These attenuation coefficient maps only need to be scaled to the energy of the emission isotope which is a simpler relationship since the transmission isotopes that are used are mono-energetic.

(iv) Radionuclide transmission systems deliver lower radiation doses to the patient than the hybrid SPECT/CT systems.

It is evident from the discussion above that both hybrid SPECT/CT as well as radionuclide transmission systems have certain advantages and limitations. One mutual limitation of both hybrid SPECT/CT as well as radionuclide transmission imaging systems are that these systems are expensive to purchase and to maintain and therefore not readily available in every nuclear medicine clinic. A solution to this problem is to use an uncollimated, printed flood source for transmission imaging.

The major advantage of a printed, flood source is that:

(i) Older existing gamma cameras would require modest or no modification to the existing gantry systems to enable them to perform transmission imaging, since the weight of the source construction is negligible.

(ii) Furthermore, the intensity distribution of a printed radioactive source can be easily modified to be suitable for a specific patient. Celler *et al.* (1998) proposed the use of a series of collimated line sources with different intensities in order to create a non-

uniform transmission profile. This will result in a more uniform transmission image of the patient. An important advantage of this configuration is that the distribution of activity in the source system is tailored to the attenuation in the human body minimising the problem encountered when too few counts are recorded in some pixels of the transmission scan.

(iii) Printed radioactive sources can also be manufactured in house, at low cost to evaluate the use of different activity distributions in the transmission source. An optimal activity distribution can then be identified.

(iv) The photon-flux with an uncollimated transmission source system is much higher than a collimated system and therefore less activity is required for the transmission source.

The disadvantages of an uncollimated transmission source include firstly the additional radiation dose to the patient (Cao and Tsui, 1992) (although still much lower than doses obtained from a CT system). Secondly, added scattered events may be present in the transmission images which need to be eliminated. The additional scattered events will lead to broad beam attenuation coefficient values which will underestimate the true attenuation coefficient values. Kojima *et al*. (2004) proposed the use of an appropriate scatter correction which can be applied to the transmission data acquired with an uncollimated flood source to correct for the scatter in the transmission data.

The primary focus of this research was to develop an uncollimated printed transmission flood source system which can be used for TCT. Presently, TCT cannot be conducted in our clinic due to the lack of transmission imaging systems on the older SPECT systems. Attenuation corrections for these systems can only be performed assuming a constant attenuation coefficient value. As mentioned before this is not a valid assumption in the thorax area with the presence of soft tissue, bone and lung tissue and can result in errors in the attenuation corrected emission images.

The purpose of this work is, therefore, the development and evaluation of an uncollimated printed transmission flood source system which would enable the user to perform TCT on older

cameras without purchasing commercial transmission imaging systems. The uncollimated transmission flood source system was evaluated for planar as well as tomographic imaging.

The first stage of the research was the development and evaluation of Tc-99m printed flood sources. The development started with the construction of uniform printed flood sources. The evaluation of these printed flood sources included tests for the uniformity and reproducibility of these sources. A non-uniform flood source for transmission imaging was constructed by depositing higher amounts of radioactivity at the cental areas of the flood source. The evaluation of this non-uniform transmission flood source resulted in a more uniform transmission image of the scanned object.

The second stage of the research was the implementation of the printed flood source for planar transmission imaging. An uncollimated source configuration was used for transmission imaging. As part of the study the contribution of scattered events in the transmission images was evaluated. The effect of the distance between the uncollimated transmission flood source and the object being imaged on the amount of scatter present in the transmission image was evaluated. The planar transmission images obtained with the uncollimated flood source were evaluated by comparing the scatter contribution in the images and the attenuation coefficient values obtained at different source object distances with the values obtained with a collimated transmission flood source.

The third stage of this research was to evaluate the application of two different scatter correction techniques on the planar transmission images. An evaluation of the scatter present in the transmission images and the attenuation coefficient values obtained after applying these two scatter corrections to the transmission data was done by comparing the results to the results obtained with a collimated transmission flood source. From these results an appropriate scatter correction was proposed for transmission imaging with an uncollimated printed flood source.

Finally, the study was extended by using an uncollimated printed flood source for TCT. The proposed scatter correction was applied to the acquired transmission data. The image quality

and accuracy of the reconstructed attenuation coefficient maps obtained after applying the selected scatter correction to the transmission data acquired with the uncollimated printed transmission source was compared with the results obtained with a collimated transmission source.

1.1 References

Almeida P, Bendriem B, de Dreuille O, Peltier A, Perrot C, Brulon V (1998). Dosimetry of transmission measurements in nuclear medicine: a study using anthropomorphic phantoms and thermoluminescent dosimeters. *Eur J Nucl Med;* **25:** pp1435–1441.

Bailey DL (1998). Transmission scanning in emission tomography. *Eur J Nucl Med;* **25**: pp774–787.

Bocher M, Balan A, Krausz Y, Shrem Y, Lonn A, Wilk M, Chisin R (2000). Gamma camera mounted anatomical X-ray tomography: Technology, system characteristics and first images. *Eur J Nucl Med;* **27:** pp619–627.

Byrne CL (1996). Block-iterative methods for image reconstruction from projections. *IEEE Trans Image Proc;* **5**: pp792–794.

Cao Z, Tsui BMW (1992). Performance characteristics of transmission imaging using a uniform sheet source with parallel-hole collimation. *Med Phys;* **19**: pp1205–1212.

Celler A, Dixon KL, Chang Z, Blinder S, Harrop R (2005). Problems created in attenuation-corrected SPECT images by artifacts in attenuation maps: A simulation study. *J Nucl Med;* **46**: pp335–343.

Celler A, Sitek A, Stoub E, Hawman P, Harrop R, Lyster D (1998). Multiple line source array for SPECT transmission scans: simulation, phantom, and patient studies. *J Nucl Med;* **39:** pp2183–2189.

Chang LT (1978). A method for attenuation correction in radionuclide computed tomography. *IEEE Trans Nucl Sci;* **25:** pp638–643.

Corbett J, Ficaro EP (2000). Attenuation correction: a better cardiac SPECT. *ACC Curr J Rev;* **9(Suppl. 1):** pp25S–31S.

Hendel RC, Corbett JR, Cullom SJ, DePuey EG, Garcia EV, Bateman TM (2002). The value and practice of attenuation from the American Society of Nuclear Cardiology and the Society of Nuclear Medicine. *J Nucl Med;* **43**: pp273–280.

Hudson HM, Larkin RS (1994). Accelerated image reconstruction using ordered subsets of projection data. *IEEE Trans Med Imaging;* **13:** pp601–609.

King MA, Tsui BM, Pan TS (1995). Attenuation compensation for cardiac single photon emission computed tomographic imaging. Part 1. Impact of attenuation and methods of estimating attenuation maps. *J Nucl Cardiol;* **2**: pp513–524.

Kojima A, Matsumoto M, Tomiguchi S, Katsuda N, Yamashita Y, Motomura N (2004). Accurate scatter correction for transmission computed tomography using an uncollimated line array source. *Ann Nucl Med;* **18**: pp45–50.

Patton JA, Delbeke D, Sandler MP (2000). Image fusion using an integrated, dual-head coincidence camera with x-ray tube-based attenuation maps. *J Nucl Med;* **41**: pp1364–1368.

Pereira JM, Stabin MG, Lima FRA, Guimarães MICC, Forrester JW (2010). Image Quantification for Radiation Dose Calculations – Limitations and Uncertainties. *Health Phys;* **99**: pp688–701.

Preuss R, Weise R, Lindner O, Fricke E, Fricke H, B Wolfgang (2008). Optimisation of protocol for low dose CT-derived attenuation correction in myocardial perfusion SPECT imaging. *Eur J Nucl Med Mol Imaging;* **35**: pp1133–1141.

Tsui BM, Zhao X, Frey EC, McCartney WH (1994). Quantitative single-photon emission computed tomography: basics and clinical considerations. *Semin Nucl Med*; **24**: pp38–65.

Wackers F (1999). "Attenuation correction, or the emperor's new clothes?" *J Nucl Med;* **40**: pp1310–1312.

Zaidi H, Hasegawa B (2003). Determination of the attenuation map in emission tomography. *J Nucl Med;* **44:** pp291–315.

Zaidi H, Hasegawa B (2006). Chapter 6: Attenuation correction strategies in SPECT. In: "*Quantitative Analysis in Nuclear Medicine*". Ed: Zaidi H, Springer, USA.

Chapter 2

Single Photon Emission Computed Tomography.

2.1 Introduction

Tomography is the imaging of the internal structures of an object through the observation of the different effects these structures have on the passage of waves of energy impinging on them. The medical applications of tomography utilize the non-invasive nature of the procedure, which makes it possible to examine living objects in vivo. Different tomographic imaging modalities provide different kinds of information depending on the data recording means. The traditional X-ray based computerized tomography (CT) produces images of photon attenuation in tissue. These images provide general anatomical information because they reveal the physical structure of the tissue. Single Photon Emission Computed Tomography (SPECT) is intended to express functional properties of the tissue. Emission refers to the fact that the energy source is not external but it is brought into the tissue as a part of the body metabolism. This is done by a tracer which is a chemical compound labelled with a radioactive isotope. The spatial distribution of the radiating source is the object of interest since it represents the concentration of the tracer in the tissue. Thus, functional SPECT images are generally different from anatomical images. Primarily, SPECT images do not express what the tissue looks like, but how it functions. Figure 2.1.(a) illustrates the anatomy of a two-dimensional slice of the human brain from a computerized tomography scan while Figure 2.1.(b) shows a slice of a functional brain image reconstructed from a nuclear medicine scan.

(a) (b)

Figure 2.1: *(a) A single slice of a computerized tomography image shows anatomical information of the brain structure, and (b) a single slice from a SPECT image shows corresponding functional information of the brain.*

Since the concept was first introduced in the 1960s, SPECT has become a routine procedure in most nuclear medicine departments (Kuhl and Edwards, 1963). SPECT imaging requires a gamma camera, a method of display, a gantry for rotating the detector around the patient and a means of performing image reconstruction. The GE Starcam 400AT (General Electric Medical Systems, Milwaukee) single headed gamma camera can be seen in Figure 2.2.

Figure 2.2: *A GE Starcam 400AT gamma camera linked to an ALFA NUCLEAR acquisition station.*

The first SPECT systems were developed in the mid 1970s using circular orbits and filtered back projection (FBP) reconstruction methods (Jaszczak *et al.*, 1977; Keyes *et al.*, 1977). Until

recently FBP has remained the most popular image reconstruction method due to its efficiency and ease of implementation. However, as iterative reconstruction methods have improved, both in terms of reconstructed image quality and speed of reconstruction, they are now practical for routine use (Stansfield *et al.*, 2010; Madsen MT, 2007; Shepp and Vardi, 1982).

After image reconstruction, SPECT scans can be displayed as slices, or a three-dimensional representation of the organ surface or a volume can be rendered. The main advantage of SPECT imaging is that out-of-plane information is removed and not simply distorted as in earlier forms of tomography in nuclear medicine (Vogel *et al.*, 1978). By removing out-of-plane information, a significant increase in image contrast can be obtained with SPECT over planar imaging techniques and visual interpretation of the SPECT scans benefits from the improved contrast as shown in Figure 2.3 (Whitehead, 1978; Jaszczak *et al.*, 1982). An example of the improved contrast of SPECT over planar images of the myocardium can be seen from the higher signal-to-noise ratio of the SPECT count rate profile Figure 2.3.(b) compared to the planar profile (Figure 2.3.(a) and (b)).

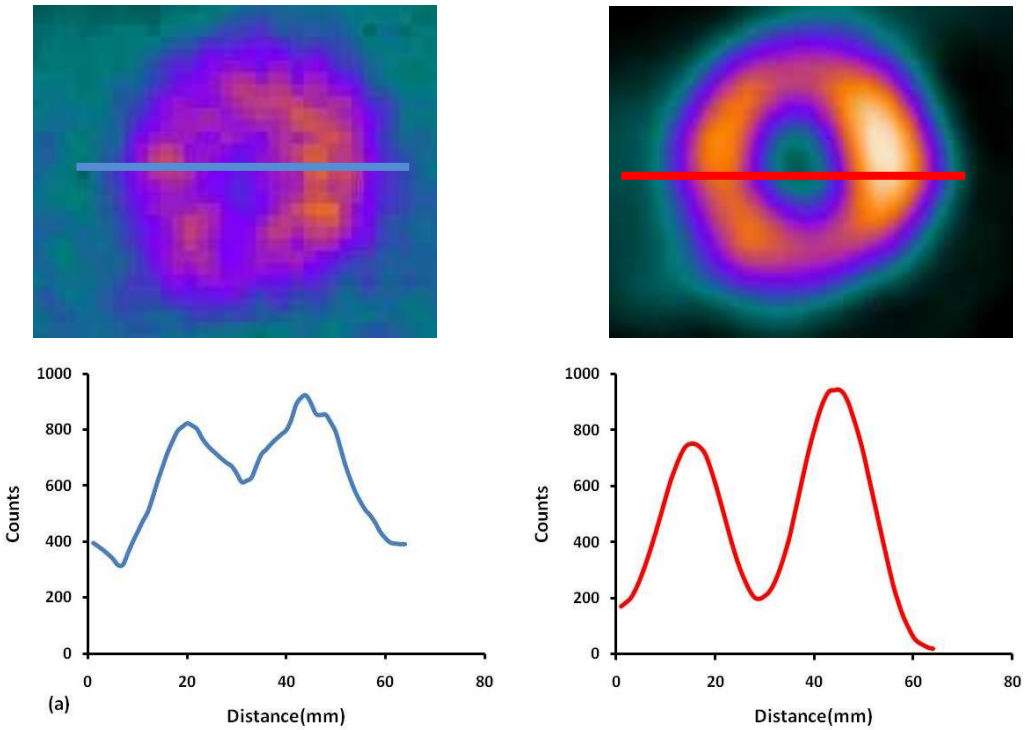

Figure 2.3: *(a) A planar image and (b) a SPECT reconstructed slice of the myocardium with corresponding horizontal count rate profiles.*

It is important to recognize that spatial resolution is not fundamentally improved by SPECT imaging and that the primary benefit of SPECT scanning lies in the improved image contrast. A further advantage of SPECT is the improved quantification of radioisotope uptake (Burdine *et al.*, 1979; Garcia *et al.*, 1985). Problems of gamma-ray attenuation and scatter may be better handled by SPECT over planar projection imaging, due to the ability of SPECT imaging to assess the amount of attenuating tissue between the skin surface and the organ of interest (Hendel *et al.*, 1999). Some improvements in SPECT technology, since the introduction of the first single-head gamma camera system, have included the use of multiple gamma camera heads as well as the application of non-uniform attenuation correction methods. In this chapter a brief overview of the SPECT camera, its performance characteristics as well as the acquisition parameters and reconstruction algorithms needed for emission and transmission imaging will be presented.

2.2 Gamma camera

2.2.1 The design of a gamma camera

Since the invention of the gamma camera by Hal Anger in the late 1950s (Anger, 1958) it has become the most widely used nuclear imaging instrument for clinical applications. Although many innovations have been made since 1958, clinical gamma cameras are often called Anger cameras because they share many of the essential features of Anger's early designs. The basic components of an Anger camera are depicted in Figure 2.4. The operation of a gamma camera is as follows.

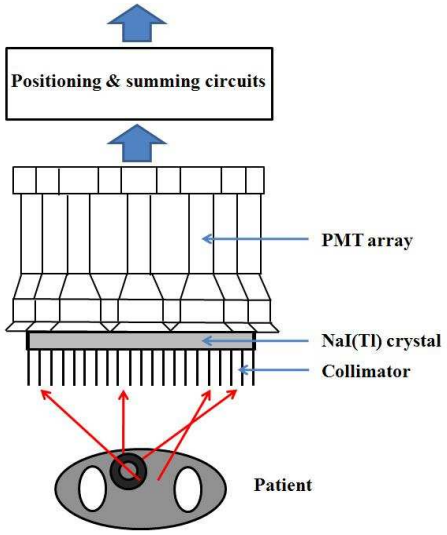

Figure 2.4: *Basic components of an Anger camera with photons emanating from the object.*

To obtain an image with a gamma camera it is necessary to project the gamma photons emitted from the patient onto the gamma camera detector. Gamma photons that do not travel in the proper direction are absorbed by the collimator of the gamma camera. The collimator is made of highly absorbing material with a high atomic number and a high density. The design parameters of a collimator are a compromise between the resolution and the sensitivity of the collimator and a trade-off between these parameters has to be found for any given type of acquisition. The remaining gamma photons then reach a scintillation crystal made of sodium iodide, doped with thallium NaI(Tl). The crystal is coated with a thin layer of Al at the front

and the edges to protect it from outside light and moisture. The gamma photons that interact with the crystal produce an amount of light photons that are proportional to the energy deposited in the NaI(Tl) crystal. These light photons are recorded by an array of photomultiplier tubes (PMTs) that is optically coupled to the back of the NaI(Tl) crystal. Light photons are converted to electrons by the photocathode of the PMT. A series of curved dynodes in the PMT amplify the number of electrons to produce a measurable electronic signal at the anode. The signals of the PMTs are used to produce the X- and Y-coordinates of the point of the photon interaction. The Z-pulse, which is proportional to the energy of the detected photon, is produced by summing the signals from the different PMTs. If the Z-pulse is of selected magnitude the X- and Y-pulses are digitized and used to increment an address location corresponding to X- and Y- coordinates in the computer memory. When a sufficient amount of photons has been detected a planar image can be displayed.

2.2.2 Performance characteristics of a gamma camera

A gamma camera is not capable of producing perfect images. Certain inherent imperfections arise from the performance characteristics of the detector, its associated electronic circuitry and the collimator. In general image uniformity, spatial resolution, energy resolution, system sensitivity and count rate performance are the indicators used to assess the system performance.

2.2.2.1 Uniformity

The flood field uniformity of a gamma camera demonstrates the ability of the camera to produce a uniform image when exposed to a homogeneous spatial distribution of gamma rays. The NEMA (NEMA, 2001) protocol for intrinsic flood field uniformity analyzes both differential and integral uniformity over the useful and central fields of view. The integral uniformity represents the maximum pixel count rate change over the indicated field of view (FOV) expressed as a percentage. The differential uniformity is the maximum change over a five pixel distance in either the X or Y directions thereby representing the maximum rate of change of the regional count rate.

2.2.2.2 Spatial resolution

The term spatial resolution of a gamma camera refers to the ability of the instrument to distinguish between two closely spaced point sources and display them as two separate points. The response of the collimated camera to a fixed point source is called the point spread function. Spatial resolution is described by the full width at half maximum (FWHM) of the point spread function of the gamma camera system. The gamma camera spatial resolution is the combined effect of the collimator resolution as well as the intrinsic resolution of the detector and the electronics. The spatial resolution is influenced by the collimator, the number of PMTs as well as the parameters defining the energy window.

2.2.2.3 Energy resolution

Energy resolution is defined as the ratio of the FWHM of the measured photo-peak to the photon energy expressed as a percentage. The energy resolution of a gamma camera is determined by the degree of fluctuation of PMT output resulting from variations in the signal generation process that starts with the photon-crystal interaction. Energy resolution is an important parameter that affects the image quality because improved energy resolution leads to better rejection of scattered photons. Successful rejection of scattered photons from the photo-peak improves the contrast of the images.

2.2.2.4 Count rate performance

The count rate performance of a gamma camera describes the non-linear relationship between the count rate and the intensity of incident gamma radiation on the crystal surface of the gamma camera. Due to pulse pile-up that occurs at high count rates, the gamma camera is unable to respond linearly when high incidence of gamma radiation arises. This non-linear response of the gamma camera due to high incidents of gamma radiation can influence the accuracy of quantification. At high count rates the resolution can also be degraded due to spatial displacements in the image.

2.2.2.5 System sensitivity

The sensitivity of a gamma camera refers to its response to a distributed source of radiation. Sensitivity is measured as the number of detected counts per unit time per unit source activity for a specified energy window and geometry of measurement. High count rates in gamma cameras can lead to pulse pile-up which can provide count losses as well as image distortions. For this reason the activity should be low enough so that count losses because of pulse pile-up is negligible. Count losses can influence the quantitative accuracy of studies acquired with the camera. Image distortions due to high count rates can also affect the uniformity as well as the spatial resolution of the gamma camera.

2.3 Acquisition parameters for emission computed tomography

There are two types of orbits which SPECT systems utilize for emission tomography namely circular and noncircular orbits. The detector(s) of a SPECT system with a circular orbit maintains a fixed radius of rotation which on average result in the detector(s) being further from the object. A circular orbit will therefore reduce the spatial resolution because the detector-to-object distance is on average larger than with a noncircular orbit. The detector(s) of a SPECT system with a noncircular orbit will follow the contour of the patient by moving the detector(s) of the gamma camera closer to the object and thereby improving the spatial resolution.

The standard matrix size for emission tomography images of a SPECT system is 64×64 or 128×128 pixels, resulting in pixel sizes ranging from $3 - 8$ mm. Larger matrix sizes (128×128), thus smaller pixel sizes, would be recommended for higher resolution studies. The matrix size should be chosen so that the pixel size Δs is less than half the spatial resolution expected which would ensure that the sampling theorem is satisfied and that the maximum spatial frequency in a study is preserved.

The optimal number of projections for tomographic studies depends on matching the number of projections to the resolution of the system. A low resolution study due to a low resolution collimator or a small matrix size (64 × 64) requires a smaller number of projection images. A high resolution study which uses a high resolution collimator or a larger matrix size (128 × 128) needs a higher number of projections images. The optimum number of projections which would prevent angular aliasing during image reconstruction is:

$$N \geq \frac{\pi D}{\Delta s / 2} \tag{2.1}$$

where N is the number of projection angles in 360°, D is the diameter of the circle enclosing the object of interest and Δs is the smallest linear dimension that can be resolved by the gamma camera. There are two modes of tomographic acquisition namely ‘‘step-and-shoot’’ and “continuous” methods. For the ‘‘step-and-shoot’’ mode the gamma camera acquires a projection image for a certain preset condition. It stops recording data when the preset condition is reached and moves the detector to the next angular position where it starts recording the next projection image. This acquisition mode results in a small amount of dead time since the gamma camera is not acquiring data while it is moving. The alternative to this mode is the ‘‘continuous’’ mode where the camera moves continuously and acquires each projection image over a certain angular increment. Although “continuous” mode eliminates the dead time and increases the image counts per projection it is at the expense of resolution due to the motion of the detector during acquisition.

2.4 Reconstruction algorithms for emission computed tomography

Tomographic images reconstructed from planar projections are superior to traditional planar views because they enable a separation of two-dimensional projections to generate a three-dimensional view of organ volumes. Due to the rich diagnostic information that can be extracted from three-dimensional images, numerous algorithms for reconstructing emission images were invented and

investigated over the past decades and many of them have been implemented on commercial SPECT gamma camera systems. The two main reconstruction categories are analytic and iterative algorithms. Analytical methods are based on exact mathematical solutions to reconstruct the radionuclide distribution. In Nuclear Medicine departments the FBP is the most popular analytical method. Iterative methods like the maximum likelihood expectation maximization (MLEM) and the ordered subsets expectation maximization (OSEM) techniques estimate the distribution through successive approximations. These algorithms are based on the process of matching the measured projections to the calculated projections. This section briefly describes the reconstruction techniques most frequently used for emission computed tomography.

2.4.1 Filtered back projection

Filtered Back Projection is an image reconstruction algorithm for reconstructing three-dimensional images from a series of two-dimensional projections (Herman, 1980). A two-dimensional projection is defined as line integrals of activity in a three-dimensional volume and usually simplified as a stack of one-dimensional projections. Thus, three-dimensional images of an object can usually be reconstructed slice by slice from a set of one-dimensional projections. Mathematically, the relationship between a two-dimensional image and one-dimensional projection can be described using the Radon Transform (RT) (Brooks and Di Chiro, 1976) achieved by integrating a two-dimensional distribution to form one-dimensional projections:

$$p(\theta, s) = \int_{l: x\cos\theta + y\sin\theta = s} f(x, y)dl \tag{2.2}$$

and

$$p(\theta, s) = \iint f(x, y)\delta(x\cos\theta + y\sin\theta - s)dxdy \tag{2.3}$$

where $p(\theta,s)$ is a projection at a specific angle θ, $l: x\cos\theta + y\sin\theta = s$ is the line equation of projection rays in the x-y domain and $f(x,y)$ is the activity distribution of an object.

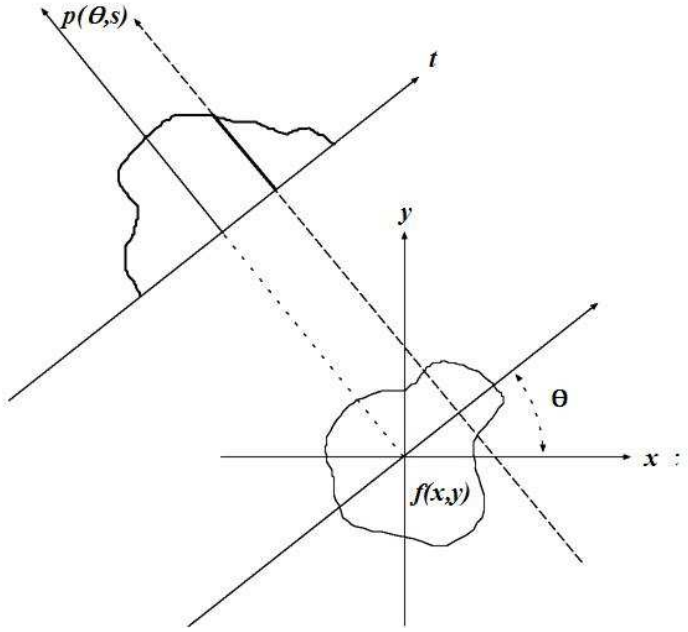

Figure 2.5: *The Radon Transform or line integral p(θ,s) of a radioactivity distribution f(x,y).*

With an inversion of Equation (2.3), by inverting the RT, the activity distribution of an object *f(x,y)* can be reconstructed from measured projections *p(θ,s)*. This inversion involves applying a Fourier Transform (FT) and an inverse FT to the RT. In the first step of the inversion, the FT needs to operate on both sides of the RT to reverse the relation of projections and activity distribution in the frequency domain based on Fourier slice theory. The projection data can then be projected back to generate the activity distribution by the inverse FT of the RT.

FT of RT:

Left side of inverse Equation (2.3):

$$P(\theta,\omega) = FT(p(\theta,s)) = \int p(\theta,s)\exp(-i\omega s)ds \qquad (2.4)$$

Right side of inverse Equation 2.3:

$$
\begin{aligned}
&FT(\iint f(x,y)\delta(x\cos\theta + y\sin\theta - s)dxdy) \\
&= \iint f(x,y)dxdy \int \exp(-i\omega s)\delta(x\cos\theta + y\sin\theta - s)ds \\
&= \iint f(x,y)\exp[-i\omega(x\cos\theta - y\sin\theta)]dxdy
\end{aligned}
\tag{2.5}
$$

Inverse FT of (FT of RT):

$$
f(x,y) = \iint P(\theta,\omega)\exp[i\omega(x\cos\theta + y\sin\theta)]|\omega|d\omega d\theta \tag{2.6}
$$

Equation (2.6) is well known as FBP with a ramp filter $|\omega|$. The ramp filter itself is a mathematically necessary component in the FBP algorithm as the name "filter" of FBP implies. The ramp filter is a correction filter for image blurring that occurs due to the process of back projection. It provides an increasing weight to higher frequency components in order to remove image blurring and therefore also amplifies noise in the image. Generally, this filter can be modified by other filters depending on the desired effect to weight specific Fourier frequencies for sharpening or smoothing images. If the projection data needs to have the noise reduced, a noise filter for example a Butterworth filter can be applied pre- or post-FBP reconstruction. For real application to reconstructing images, FBP needs to be implemented in a discrete form. This can be given by:

$$
P(\theta,\omega) = \sum_{-L/2}^{L/2} p(\theta,s)\exp(-i\omega s)\Delta s \tag{2.7}
$$

$$
f(x,y) = \sum_{-\omega_m}^{\omega_m}\sum_{o}^{\pi} P(\theta,\omega)\exp[i\omega(x\cos\theta + y\sin\theta)]|\omega|\Delta\omega\Delta\theta \tag{2.8}
$$

where L is the total length of a detector array and Δs is the size of detector element. For a detector matrix of 128×128, Δs is equal to $L/128$ and the highest sampling frequency or Nyquist frequency ω_m is equal to $1/(2\Delta s)$. For a certain number of projections N as defined in Equation (2.1) the angular sampling rate $\Delta\theta$ in 360° is defined as $2\pi/N$. For a 360° orbit, SPECT study linear sampling requires a matrix size set to 64 or 128 depending on the spatial resolution requirements of the study. From Equation (2.1) it is evident that for a smaller pixel size and a larger object of interest more projections angles are needed to prevent reconstruction streak artefacts than for a smaller object and larger pixel size.

The main reason for using FBP is that it is a fast and validated method for reconstructing SPECT images. However, due to a low rate of angle sampling, SPECT images reconstructed by FBP are usually blurred. While corrections for image artefacts are required, FBP is unable to achieve this because it lacks adequate models to correct for attenuation, scatter and collimator blurring artefacts. At present, due to improved computer processing speed the FBP algorithm is being replaced in most clinics with alternative algorithms which will be described in the following section. These algorithms can correct efficiently for attenuation, scatter and collimator blurring artefacts which are present in uncorrected SPECT images.

2.4.2 Iterative reconstruction techniques

2.4.2.1 Iterative maximum likelihood expectation maximization approach

Image reconstruction using the maximum likelihood approach seeks a converged solution of the final reconstruction by iteratively maximizing the log likelihood function created from the projection data and imaging models. In an Expectation Maximization (EM) algorithm, the emission process is usually modelled with the Poisson probability distribution. This model is given as:

$$P = f(b|a) = e^{-(a\Delta t)} \frac{(a\Delta t)^b}{b!} \tag{2.9}$$

where a is the mean of the number of emitted photons, and b is the number of photons emitted in a period of time Δt. This model defines a probability describing an expectation of emitted photon numbers b in a period of time Δt based on the mean of emitted photons a. For the case of a detection process, a is the mean of detected photons and b becomes the number of detected photons in a period of time. Using Poisson probability, an EM algorithm can properly model the noise texture of projections into reconstruction images. The next section describes the OSEM.

2.4.2.2 Ordered subsets expectation maximization

In 1994, Hudson and Larkin (1994) proposed a novel idea to accelerate the slow reconstruction of MLEM by using partial information from grouped projections. Using this approach, an image can be updated several times toward convergence in a single iteration, thus the iteration number can be reduced. This algorithm is known as OSEM:

$$\lambda_j^{new} = \frac{\lambda_j^{old}}{\sum_{i \leftarrow S_n} C_{ij}} \sum_{i \leftarrow S_n} C_{ij} \frac{Y_i}{\sum_m C_{im} \lambda_m^{old}} \tag{2.10}$$

where λ_j represents the estimated intensity at pixel j, Y_i represents the measured events in projection bin i, and C_{ij} represents the relative contribution of pixel j to the measurement in projection bin i. The *new* and the *old* superscripts indicate new and former estimates. Non-uniform attenuation, detector response or scatter can be represented by the elements C. S_n represent the the n^{th} grouped subset of the projection bins. The back projection is done for a subset S_n of the projection bins. OSEM utilizes subsets S_n grouped from skipped projections in the back projection step and still sums over all projections in the forward projection step. Thus if an image is reconstructed using 4 subsets of 32 projections in a 180° acquisition, the way to group 4 subsets is indicated as: subset 1 (1, 2, 9,10, 17, 18, 25, 26), subset 2 (3, 4, 11, 12, 19, 20, 27, 28), subset 3 (5, 6, 13, 14, 21, 22, 29, 30) and subset 4 (7, 8, 15, 16, 23, 24, 31, 32). Reconstructing an image from the grouped subsets S_n is like imparting partial information that can update the image faster in a single iteration, thus requires a smaller number of iterations. A rule of thumb indicates that the image quality and noise property of OSEM with n subsets and m iterations is close to MLEM with $m \times n$ iterations (Lalush and Tsui, 2000). Even with the great advantage of speedy reconstruction, OSEM actually does not guarantee convergence. In fact, accelerating a reconstruction rather than approaching the fixed point (convergent solution) slowly enough may eventually result in non-convergent solutions. This incompleteness has been reviewed carefully based on two parameters: the number of subsets and the number of iterations. Because of a similarity to MLEM, but with a faster reconstruction speed comparable to FBP, OSEM is growing in recognition and is today available on most commercial SPECT cameras.

2.5 Discussion

This chapter briefly describes the nature of nuclear medicine and provides a brief overview of the instrumentation and properties of the gamma camera. The main focus of this thesis is transmission computed tomography and a brief summary of the image reconstruction techniques used in this study for emission computed tomography was discussed.

The FBP algorithm is efficient but does not provide for physical effects like attenuation, scatter and collimator detector response that deteriorate SPECT images. In emission tomography, the measured data have a strong noise component due to the statistical nature of the decay of the radiating source. This is why the FBP images are often contaminated by noise and reconstruction artefacts. In order to take into account the acquisition process of emission tomography, iterative reconstruction methods utilize a statistical model. The main problem with iterative algorithms is the increase of noise in the image when the number of iterations increases. This is unfortunate because the quantitative accuracy requires a reliable evaluation of the concentration value of a region of interest of the image. On the other hand, iterative reconstruction techniques use a more general linear model that can compensate for the physical effects like attenuation, scatter and collimator detector response.

The slow convergence of the MLEM has led to the creation of accelerated iterative methods. OSEM is one example of an accelerated iterative method that makes use of partial information to speed up the reconstruction process.

By incorporating the physical effects into the image reconstruction process, one can improve the quality and quantitative accuracy of SPECT images at the cost of added processing time. Photon attenuation and scatter are two sources of SPECT image degradation that will be reviewed in next chapter.

2.6 References

Anger HO (1958). Scintillation camera. *Rev Sci Instr;* **29:** pp27–33.

Brooks RA, Di Chiro G (1976). Principles of computer assisted tomography (CAT) in radiographic and radioisotopic imaging. *Phys Med Biol;* **21:** pp689–732.

Burdine JA, Murphy PH, DePuey EG (1979). Radionuclide computed tomography of the body using routine radiopharmaceuticals. II Clinical applications. *J Nucl Med;* **20:** pp108–114.

Garcia EV, Van Train K, Maddahi J, Prigent F, Friedman J, Areeda J, Waxman A, Berman DS (1985). Quantification of rotational thallium-201 myocardial tomography. *J Nucl Med;* **26:** pp17–26.

Hendel RC, Berman DS, Cullom SJ, Follansbee W, Heller GV, Hosen K, Groch MW, Mahmarian JJ (1999). Multicenter clinical trial to evaluate the efficacy of correction for photon attenuation and scatter in SPECT myocardial perfusion imaging. *Circ;* **99:** pp2742–2749.

Herman GT (1980). The Algebraic reconstruction techniques. In: *Image reconstruction from Projections: The fundamentals of computerized tomography.* Academic Press, New York, USA.

Hudson HM, Larkin RS (1994). Accelerated image reconstruction using ordered subsets of projection data. *IEEE Trans Med Imaging;* **13:** pp601–609.

Jaszczak RJ, Murphy PH, Huard D, Burdine JA (1977). Radionuclide emission computed tomography of the head with ^{99m}Tc and a scintillation camera. *J Nucl Med;* **18:** pp373–380.

Jaszczak RJ, Whitehead FR, Lim CB, Coleman RE (1982). Lesion detection with single-photon emission computed tomography (SPECT) compared with conventional imaging. *J Nucl Med;* **23**: pp97–102.

Keyes JW Jr, Orlandea N, Heetderks WJ, Leonard PF, Rogers WL (1977). The Humongotron: A Scintillation-Camera Transaxial Tomograph. *J Nucl Med;* **18:** pp381–387.

Kuhl DE, Edwards RQ (1963). Image separation radioisotope scanning. *Radiol;* **80:** pp653–662.

Lalush DS, Tsui BMW (2000). Performance of ordered-subsets reconstruction algorithms under conditions of extreme attenuation and truncation in myocardial SPECT. *J Nucl Med;* **41:** pp737–744.

Madsen MT (2007). Recent Advances in SPECT Imaging. *J Nucl Med;* **48**: pp661–673.

National Electrical Manufacturers Association (NEMA) (2001). Performance Measurements of Scintillation Cameras. (Washington, D.C. National Electrical Manufacturers Association).

Shepp LA, Vardi Y (1982). Maximum likelihood reconstruction for emission tomography. *IEEE Trans Med Imaging;* **1:** pp113–122.

Stansfield EC, Sheehy N, Zurakowski D, Vija AH, Fahey FH, Treves ST (2010). Pediatric ^{99m}Tc-MDP Bone SPECT with Ordered Subset Expectation Maximization Iterative Reconstruction with Isotropic three-dimensional Resolution Recovery. *Radiol;* **257**: pp793–801.

Vogel RA, Kirch D, LeFree M, Steele P (1978). A new method of multiplanar emission tomography using a seven pinhole collimator and an Anger scintillation camera. *J Nucl Med;* **19:** pp648–654.

Whitehead FR (1978). Minimum detectable gray-scale differences in nuclear medicine images. *J Nucl Med;* **19:** pp87–93.

Chapter 3

Attenuation and Scatter Correction in SPECT

3.1 Introduction

Single Photon Emission Computed Tomography (SPECT) imaging has limitations and therefore is not ideal. Accuracy of SPECT images is degraded by these limitations that include physical effects of attenuation, Compton scatter, detector response and patient movement. Compensation for attenuation (Tsui *et al.*, 1989) has been studied at great length, and several methods have been proposed (Bailey *et al.*, 1987; Cao and Tsui, 1992; Celler *et al.*, 1998; Tan *et al.*, 1993; Tung *et al.*, 1992; Jaszczak *et al.*, 1993). Figure 3.1.(a) shows an example of a patient with a partially reversible perfusion defect inferiorly on the non-attenuation corrected horizontal long axis slice images, whereas Figure 3.1.(b) shows normal inferior wall uptake after attenuation correction in the corresponding images.

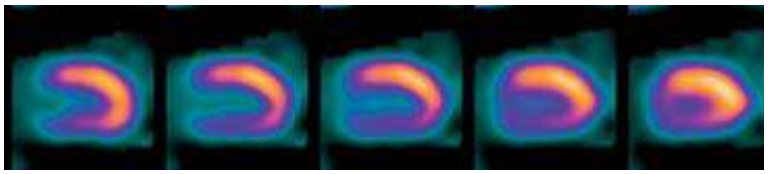

(a)

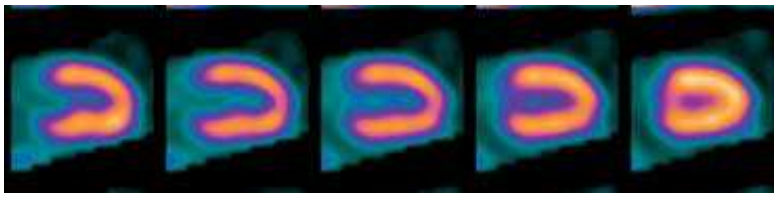

(b)

Figure 3.1: *(a) An example of an inferior myocardial perfusion defect in non-attenuation corrected images (b) and uniform inferior count distribution after applying an attenuation correction.*

However, correcting for attenuation only is not sufficient because the erroneous information given by scattered photons can produce an over-compensation. This is seen as the major source of apparent overcorrection in the inferior wall of the left ventricle of the heart, which is associated with hepatic uptake (King *et al.,* 1996) in myocardial perfusion SPECT studies. Consequently, it is necessary to correct simultaneously for attenuation and scatter. It has been shown that when accurate scatter correction models are used the over-correction in the heart is improved (Tsui *et al.,* 1994**a**) and the signal to noise ratio of small low activity lesions is also improved (Beekman *et al.,* 1996; Hutton, 1997). In addition, it has been known for some time that the geometric response of the collimator produces a spatially varying partial volume effect in SPECT images (Cherry *et al.,* 2003**a**; Tsui *et al.*, 1998). It was found, for example in dynamic cardiac SPECT that the correction for geometric response reduces the partial volume effect and reduces the bias in estimated kinetic parameters (Kadrmas *et al.*, 1999). While some methods perform pre-subtraction of the scatter component from projection data before the reconstruction process, linear algebraic methods allow the incorporation of attenuation, scatter and geometric response corrections in the reconstruction process. This chapter will focus on two of the causes of image degradation, namely attenuation and scatter, and how they can be compensated for.

3.2 Attenuation

Although attenuation is but one of several causes of image degradation, it affects image quality severely and hence it receives much attention. As photons travel through body tissues, they are attenuated due to the photo-electric effect and Compton scattering (Cherry *et al.,* 2003**b**; Tsui *et al.,* 1994**b**). Attenuation is defined as the reduction of the number of detected gamma rays due to the photoelectric effect and Compton process. The photo-electric effect is an atomic absorption process in which the energy of an incident photon is absorbed totally by the atom and an electron is ejected. Compton scattering is a collision between a photon and a free electron. The photon loses part of its energy and changes direction after the scattering process, and some of the photons are scattered out of the field of view (FOV) and are never detected. Therefore, those photons absorbed totally by the

tissue, and those scattered out of the FOV contribute to attenuation. Attenuation, usually measured in terms of a linear attenuation coefficient with units of cm^{-1}, measures the fractional reduction of the number of detected gamma rays by the photo-electric process and Compton scatter per unit thickness of the attenuator in question. If a narrow "pencil" beam of photons, of intensity I_0, is transmitted through a medium with a constant attenuation coefficient, the intensity of the beam drops according to Beer's Law (Cherry *et al.*, 2003**c**):

$$I(x) = I_0 e^{-\mu x} \tag{3.1}$$

where $I(x)$ is the photon intensity after passing a distance x through the medium. Beer's Law only calculates the number of primary photons and do not include the scattered photons transmitted through the medium. In order to correct for attenuation correctly it is necessary to correct for scattered photons before applying an attenuation correction. The attenuation coefficient depends on a number of factors including photon energy, scattering cross-section of the material and electron density. The attenuation effect is extremely important, because it causes significant data loss and resulting image errors (Stodilka *et al.*, 1998**a**).

Patient specific information on the spatial distribution of attenuation coefficients is required in order to calculate and model the attenuation. The attenuation map is usually not uniform, but varies with position in a complicated way. For example, in the thorax, with very different attenuation coefficients for lung, muscle and bone, the attenuation effect is much more complicated. Transmission computed tomography (TCT) is implemented to obtain the attenuation map.

3.3 Transmission computed tomography (TCT)

An attenuation map must be available to be able to perform an attenuation correction during tomography. An attenuation map is an image of attenuation coefficients in the patient's

body. During TCT transmission data is acquired, and reconstructed to produce the attenuation map. The map is then incorporated in the SPECT reconstruction process to compensate for photon attenuation. The determination of an accurate, patient-specific attenuation map is fundamental to performing accurate attenuation correction. According to literature the most reliable method to determine non-uniform attenuation maps is by using transmission measurements with either a radionuclide transmission source or a Computed Tomography (CT) scanner which uses an X-ray tube as a source of radiation (Zaidi and Hasegawa, 2003).

3.3.1 TCT measurements with a radionuclide source

To obtain an attenuation map with a radionuclide, two separate scans are acquired with the transmission source. The first scan is acquired with no object in the FOV of the SPECT camera. This is referred to as the blank or reference scan. The second scan is acquired with the object of interest in the FOV. This is the transmission scan. The relationship between the reference I_{ref} and transmission I_{trans} counts in any particular projection element is given by the usual exponential relationship for γ-ray attenuation:

$$I_{trans} = I_{ref} e^{-\mu x} \tag{3.2}$$

Taking the natural logarithm of the ratio of the two scans results in:

$$\ln\left(\frac{I_{ref}}{I_{trans}}\right) = \mu x \tag{3.3}$$

Projection profiles of μx represent the sum of the attenuation coefficients along each line of response:

$$\mu x = \sum_i \mu_i \Delta x_i \tag{3.4}$$

where μ_i is the linear attenuation coefficient for the i^{th} pixel and Δx_i is the path length of the line response through the i^{th} pixel. Using reconstruction methods described in Chapter 2 the projection profiles of μx can then be reconstructed using FBP or iterative techniques.

Sequential emission–transmission scanning is technically easier to perform than simultaneous scanning, but it increases the imaging time and suffers from image registration problems caused by patient misalignment or motion. Simultaneous acquisition requires no additional time for the emission and transmission measurements, which is important for routine clinical studies. However, errors may be introduced due to cross-talk between the transmission and emission data. It has been shown that the attenuation coefficients and activity concentrations are not significantly different when estimated with sequential and simultaneous emission transmission imaging (Tung *et al.*, 1992). The following sub-sections describe the different transmission sources and data acquisition geometries that have been proposed.

Radionuclide transmission-based methods in SPECT predominantly use (i) gadolinium-153 (97 keV, 103 keV) (Tan *et al.*, 1993; Gallowitsch *et al.*, 1998) as the external source but may also use cobalt-57 (122 keV, 137 keV) (Shotwell *et al,*. 2002), (ii) barium-133 (356 keV) (Beekman *et al,*. 1998), (iii) americium-241 (59 keV) (Ficaro *et al,*. 1994), (iv) technetium-99m (140 keV) (Frey *et al,*. 1992) and (v) cerium-139 (165.9 keV) (Du Raan *et al.*, 2000).

The difference in emission and transmission photon energies necessitates that the measured attenuation coefficients must be scaled to match the emission radionuclide. The accuracy of the transmission and emission maps produced when different transmission–emission source combinations are used has been the subject of a long debate (Van Laere *et al.*, 2000; Ficaro *et al.*, 1994). In addition, various approaches have been proposed to eliminate contamination of emission data by transmission photons and to reduce spill-over of emission data into the transmission energy window (Bailey *et al.*, 1987; Gilland *et al.*, 1998).

The first configuration is shown in Figure 3.2 and is that of a sheet transmission source opposite a parallel-hole collimator on the camera head. This configuration was investigated for a number of years for use with SPECT systems (Bailey *et al.*, 1987; Maeda *et al.*, 1981; Malko *et al.*, 1985).

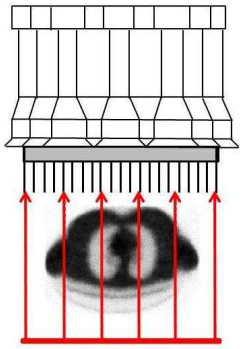

Figure 3.2: *A sheet transmission source opposite a parallel-hole collimator of the detector.*

Its major advantage was that it provided a transmission source which fully irradiated the camera head opposed to it, and needed no motion of the source beyond that provided by the rotation of the gantry. The disadvantages of this configuration were that it was cumbersome to work with and required source collimation to reduce scatter.

The second configuration illustrated in Figure 3.3 is that of the multiple line-source array (Celler *et al.*, 1998). With this configuration, the transmission flux comes from a series of collimated line sources aligned parallel to the axis of rotation of the camera.

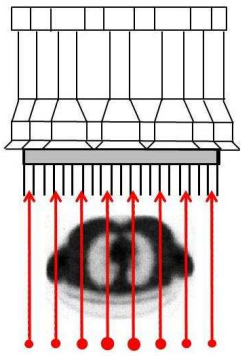

Figure 3.3: *A multiple line-source array opposite a parallel-hole collimator.*

The spacing and activity of the line sources are tailored to provide a greater flux near the centre of the FOV, where the attenuation from the patient is greater. A major advantage of the multiple line-source array is that the distribution of activity in the source system is tailored to the attenuation in the human body minimizing the problem encountered when too few counts are recorded in some pixels of the transmission scan. Another advantage is that no scanning motion of the sources is required. A major disadvantage of this system is the amount of cross-talk between the emission and transmission photons.

In the third configuration (Figure 3.4) the sheet or multiple-line transmission source is replaced by a scanning-line source (Tan *et al.*, 1993). The camera head opposite the line source is electronically windowed to store only the events detected in a narrow region opposite to the line source in the transmission image.

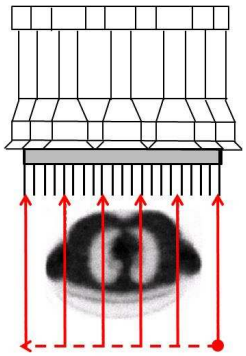

Figure 3.4: *A scanning-line source opposite a parallel-hole collimator.*

The electronic window moves in synchrony with the line source thereby allowing transmission imaging across the entire FOV. The result is a significant reduction in the amount of scattered transmission radiation imaged in the transmission energy window. The transmission counts are concentrated in this moving spatial window thereby increasing their relative contribution compared to the emission events. By using only the portion of the FOV outside the transmission electronic window for emission imaging, a significant reduction in the amount of cross-talk between transmission and emission images were obtained. The scanning-line source does have the disadvantage of requiring synchronized mechanical motion of the source with the electronic windowing employed to accept the

transmission photons. However, the significant advantages of this method compared to its disadvantages are such that it is currently the dominant configuration offered commercially.

The need for lateral motion of the transmission source can be avoided by using convergent collimation. A fan-beam collimator with a line transmission source at its focal distance as illustrated in Figure 3.5 has a certain advantage over parallel collimation for emission imaging.

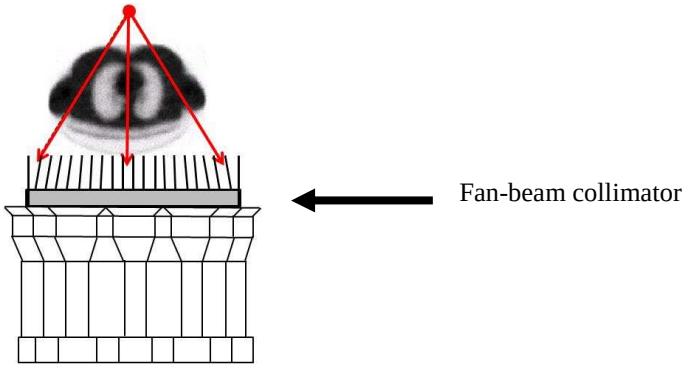

Figure 3.5: *A fan-beam collimator with a line transmission source at its focal distance.*

This configuration has better spatial resolution and only line or point sources are needed for imaging (Tung *et al.*, 1992; Jaszczak *et al.*, 1993; Gullberg *et al.*, 1998). There are also potential disadvantages with this configuration. These include possible truncation of images, the need to keep the transmission source at its convergence location and cross contamination between emission and transmission imaging.

By using an asymmetric fan-beam collimator as shown in Figure 3.6 truncation can be eliminated (Gilland *et al.*, 1998; Chang *et al.*, 1995; Hollinger *et al.*, 1998; LaCroix and Tsui , 1999).

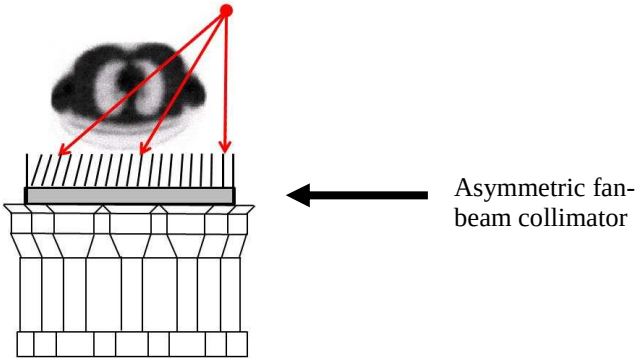

Figure 3.6: *An asymmetric fan-beam collimator with a point source with electronic collimation.*

By rotating the collimator 360º around the patient, conjugate views will fill in the truncated region. If a point source with electronic collimation is employed instead of a line source, then a significant improvement in cross-talk can also be obtained with this configuration (Beekman *et al.*, 1998). Other benefits are that point sources cost less than line sources, and are easier to shield and collimate.

In summary, it is evident from the above mentioned transmission configuration that each system has its unique advantages and shortcomings. For this reason gamma camera manufacturers are still optimizing the systems that are being used to acquire the transmission data. One transmission system that has emerged as an alternative to the above mentioned TCT with a radionuclide is the hybrid SPECT/CT system.

3.3.2 TCT measurements with a CT scanner

Recently, hybrid SPECT/CT systems as shown in Figure 3.7 consisting of multi-detector SPECT scanners coupled to conventional CT systems have been introduced (Lang *et al.*, 1992; Bocher *et al.*, 2000). Developed primarily for anatomical and metabolic image fusion in the oncology community, these systems use the CT image for attenuation correction of, for instance, myocardial perfusion SPECT images.

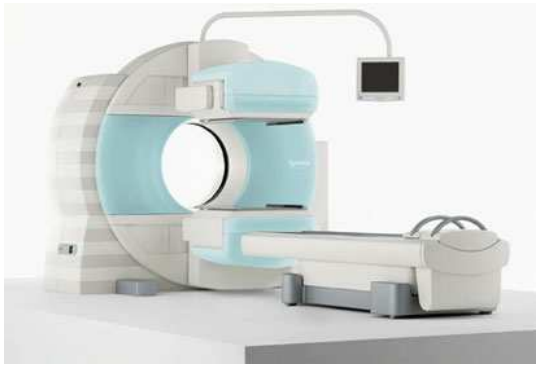

Figure 3.7: *A Siemens Symbia® SPECT/CT system consisting of multidetector SPECT scanners coupled to a conventional CT system.*

Early systems utilized low energy CT capabilities, but have recently been improved to include high-quality multi-slice imaging systems (Bocher *et al.*, 2000; Patton *et al.*, 2000). All studies are acquired sequentially on these systems as a result of the tandem positioning of the SPECT and CT components. Because of the very high photon flux from the X-ray source, the attenuation map may be acquired using fast (few seconds) or slow (few minutes) protocols with spiral and indexed modes. CT image-based attenuation maps have a high spatial resolution and a low noise level compared with attenuation maps measured using transmission measurements with a radionuclide. A dedicated CT scanner however, gives a relatively high radiation dose to the patient (Preuss *et al.*, 2008; Almeida *et al.*, 1998) in comparison to a radionuclide transmission scan. The X-ray tubes in some SPECT/CT hybrid cameras operate on a lower dose-level compared with a dedicated CT scanner, and the acquired CT images are also used for localisation of radionuclide distributions.

Hybrid SPECT/CT offers practical advantages over transmission imaging with a radionuclide source for generating an attenuation map. First, the photon fluency rate from the X-ray tube is several orders of magnitude higher than that obtained from a radionuclide transmission source. This allows the transmission data to be acquired faster and with a higher statistical quality than transmission data from radionuclide transmission scanning. Second, the higher fluency rate from the X-ray tube also allows the transmission data to be acquired after the patient is injected with the radiopharmaceutical. Errors caused by cross-

contamination by emission photons that can occur when the transmission data are acquired using an external radionuclide source are also eliminated by SPECT/CT systems. Finally, the X-ray source does not decay, is more stable, does not need frequent replacement, and produces transmission data of higher quality than that acquired from radionuclide transmission sources. However, as pointed out before, a CT scanner gives a relatively high dose (Huda *et al.*, 2000) to the patient and is also more expensive than SPECT systems with external radionuclide sources.

3.4 Attenuation correction methods

In general, attenuation correction can be applied in different ways. The correction can be applied before the reconstruction (pre-processing method), during reconstruction (intrinsic method) and after the reconstruction (post-processing method). For pre-processing and post-processing methods, simple analytical methods for attenuation correction are commonly used for SPECT, in combination with FBP.

3.4.1 Pre-processing method

Attenuation correction of the projection data prior to reconstruction is used in many commercial SPECT software packages (Sorensen, 1974). The method is easy to apply and fast. In the pre-processing method, conjugate views can be used, under the assumption that the source and tissue distribution is uniform. The technique gives good results in the case of a single source in a uniform attenuating medium. When there are multiple sources, at different depths in the object, the methods can create artefacts by giving counts in the region between the individual sources. Modifications in the Fourier transform of the sinogram have improved this technique (Glick and Xia, 1997). The disadvantage of these methods is that they produce streak artefacts in the presence of noisy data and have difficulties in coping with non-uniform attenuation.

3.4.2 Post-processing method

A well-known post-reconstruction technique is the method by Chang (1978) The Chang attenuation correction is currently the most widely applied method in clinical SPECT. The post-processing method corrects for attenuation after image reconstruction by multiplying each image voxel by an attenuation scaling factor. These factors can be derived from the average attenuation factors from each point of the object towards the detector, over all the angles. For this calculation the body outline has to be known, together with the attenuation coefficient.

It is also possible to calculate the average attenuation factor from a non-uniform object, assuming the distribution of the attenuation coefficients is known (Cao and Holder, 1998). This approach can never be exact, unless an iterative algorithm is used. The technique was improved by implementing multiple iteration of the Chang algorithm (Pan *et al.*, 1993). Because of noise amplification by this method it is recommended not to exceed two iterations. Under these restrictions the technique works well for homogeneous media with small regions of interest and low background activity. The Chang algorithm takes a first step toward non-uniform attenuation correction. It is well known, however, that the human body is not uniform. For brain imaging it might be possible to assume a uniform distribution of attenuation coefficients in the brain itself, but the surrounding skull and lower structures can create artefacts when using uniform attenuation correction (Rajeevan *et al.*, 1998; Stodilka *et al.*, 1998**b**). At present, in clinical practice, most image reconstructions are performed with analytic methods because they are relatively quick and easier to implement than iterative methods. However, the images produced by analytic algorithms tend to be streaky and display interference between regions of low and high tracer concentration.

3.4.3 Intrinsic methods

Intrinsic methods for attenuation correction incorporate attenuation effects directly into the reconstruction algorithm. These methods are more sophisticated than the pre- and post-

reconstruction methods and require more computational time. These methods can take account of non-uniform attenuation. Intrinsic methods, which properly model the attenuation process, have the potential for accurate quantification of the source distribution in the body. Two basic approaches as described in Chapter 2 have been proposed namely a modified FBP method and iterative reconstruction techniques. Iterative reconstruction is more and more becoming the standard reconstruction technique. The attenuation correction process can be integrated within the transition matrix of an iterative reconstruction algorithm. The acquired attenuation map contains information about the distribution of linear attenuation coefficients and accurately delineates the contours of structures in the body. The iterative reconstruction algorithm uses this information to calculate the attenuation to the boundary of each attenuating region. This is done for each pixel along the ray between the points of emission and detection. These values are then summed to estimate the projected or back projected pixel values. The natural approach for implementing attenuation and scatter models within an iterative reconstruction algorithm incorporates these effects in both the forward-projection and the back-projection steps. The estimated projection values are calculated for each iteration and compared against the measured projection values. The comparison process is used to generate a correction term that is applied to update the estimate of radionuclide concentrations in the image. This procedure iteratively improves the accuracy of the estimated images by modelling photon attenuation that is present in the measured projection data. By applying only an attenuation correction to the acquired data, the scattered photons would deteriorate the image quality. Therefore correction algorithms for attenuation, scatter and detector response cannot be used solely, but have to be combined with each other (Tsui *et al.,* 1998).

3.5 Scatter

The attenuation effect is associated with a photon that is absorbed (i.e. photo electric absorption) or scattered (i.e. Compton scatter) and not detected by any detector. Some attenuated photons are not absorbed, and are scattered in a new direction such that they do interact with the detector. For a Compton scattered photon, its energy is related to the

scattering angle θ under the law of energy and momentum conservation, and this can be given by (Cherry *et al.*, 2003**a-d**):

$$E_s = \frac{E_0}{\left[1+\left(\frac{E_0}{0.511}\right)(1-\cos\theta)\right]} \tag{3.5}$$

where E_o and E_s are the energies (in keV) of the incident and scattered photons, respectively. Therefore, after Compton scattering, a photon will lose some of its energy and change its direction. The larger the scattering angle, the greater the loss of energy from the incident photon. Scatter depends on source location, the geometry and composition of the medium, energy of the photon, energy resolution of the detector, and energy window used in imaging (King *et al.*, 1995). Since scattered photons have less energy than the unscattered photons, one can thus separate them using energy discrimination. However, because of the finite energy resolution of the detector, a certain number of scattered photons are still detected (Tsui *et al.*, 1994**b**).

The imaging of scattered photons degrades contrast and signal-to-noise ratio (SNR), and must be accounted for if attenuation compensation is to be accurate (Jaszczak *et al.*, 1982). The methods for estimating attenuation maps, available commercially, try to estimate "good geometry" attenuation coefficients. In the past**,** the use of an effective (reduced) attenuation coefficient approximately accounted for the presence of scattered as well as primary photons in the projections when performing attenuation correction (Cherry *et al.*, 2003**a-d)**. The use of an effective attenuation coefficient to compensate for the presence of scatter is only, at best, a very approximate solution since the scatter distribution that is detected depends not only on the attenuator but also on the source distribution. Thus instead of using an effective attenuation coefficient it is better to perform both scatter correction and attenuation correction in conjunction because this leads to more accurate quantitative and qualitative results (Tsui *et al.*, 1998).

The best way to reduce the effects of scatter would be to improve the energy resolution of the imaging systems by using an alternative to the NaI(Tl) scintillator so that fewer scattered photons are acquired (Cherry *et al.*, 2003**a-d**).

A number of scatter correction methods have been proposed for SPECT systems that employ NaI(Tl) detectors. These scatter correction methods can be categorized by the number of energy windows used for data acquisition (Ogawa, 2004).

3.5.1 Scatter estimation methods

In the deconvolution method (Axelsson *et al.*, 1984), a conventional energy window is used and the scattered photons are removed from measured photons by a deconvolution process. The kernel used for the deconvolution is approximated to an exponential function and this kernel is applied to the planar image or a reconstructed image. The point spread function (kernel) is a function of position, and this is influenced by the distribution of activity and attenuation coefficients. This method may therefore cause under- or over-correction for scatter.

The methods that use two energy windows include the dual energy window subtraction method (DEWS) (Jaszczak *et al.*, 1984; Lowry and Cooper, 1987; Pretorius *et al.*, 1993) and the dual photo-peak window method (DPW) (King *et al.*, 1992). In the DEWS method two planar images are acquired, the photo-peak energy window and a scatter window, and half of the counts in the scatter window are subtracted from the counts in the photo-peak window on a pixel by pixel basis. This method is simple and works well when the source is distributed uniformly in an object. In this method the photo-peak window measures the primary photons as well as mainly the first- and second order scattered photons. The scatter window however measures the higher order Compton scattered photons. The distribution of lower order scattered photons differs from that of the higher order scattered photons, so that the accuracy of this method is not always adequate. The DPW method measures photons with two energy windows dividing the photo-peak symmetrically into

two parts and estimates the counts of scattered photons by a regression method. This method is sensitive to photo-peak energy and since the high voltage of the PMTs can sometimes vary slightly, this method needs careful implementation in clinical situations.

The method which is based on an artificial neural network (Ogawa and Nishizaki, 1993) uses five energy windows set around the photo-peak. With training data generated by a Monte Carlo simulation, the artificial neural network estimates the amount of primary photons in the measured data. This method withstands statistical noise because the energy window is relatively wide and it estimates the counts of primary photons in a manner similar to pattern recognition. On the other hand, there are some methods that use more than five narrow energy windows.

The holospectral method (Gagnon *et al.*, 1989) measures an energy spectrum at each pixel position using narrow windows with a width of 2 keV, and estimates the counts of primary photons by means of the principal component analysis method. The counts measured with the narrow energy window are strongly influenced by statistical noise, so this method is not effective except in the case of adequate counts.

The energy weighted acquisition method (Hamill and DeVito, 1989) compensates for scattered photons by adding the counts of acquired photons multiplied by a weighing factor determined in advance. Actually this weighing factor varies according to the activity distribution and attenuation map, so that this method may not yield quantitative accurate results.

The spectrum fitting method (Koral *et al.*, 1988) estimates an energy spectrum of primary photons with the principle that the energy spectrum of the primary photons can be approximated by the normal distribution. In this method the statistical noise that is introduced in the projection data measured with narrow energy windows degrades the accuracy of estimation.

The inverse Monte Carlo method (Floyd *et al.*, 1986) calculates an original source location from the energy of an observed photon and its position with the help of the Monte Carlo simulation. This method requires a heavy computational load and is not easily applicable to clinical studies.

The other scatter correction methods include the transmission dependent scatter correction (TDSC) method (Meikle *et al.*, 1994; Narita *et al.*, 1996) and the iterative correction method which eliminates scattered photons in the image reconstruction with MAP-EM or ordered subsets expectation maximization (Tsui *et al.*, 1998; Kadrmas *et al.*, 1998). The TDSC method iteratively estimates the distribution of scattered photons with the help of the attenuation map. This method is well established but requires more information on the attenuation map. A statistical approach such as the MLEM method requires a model for distribution of scattered photons and is time consuming when using a three-dimensional kernel.

With the above observations it is clear that the accurate estimation of scattered photons requires knowledge of the accurate shape of the energy spectrum, but too narrow an energy window introduces statistical noise into acquired data. So a compromise is needed between spectral accuracy and statistical noise.

3.5.2 Scatter correction methods used in this project

3.5.2.1 Triple Energy Window (TEW) method

The Triple Energy Window (TEW) method (Ogawa *et al.*, 1991; Ichihara *et al.*, 1993) uses three energy windows (one main window and two scatter sub-energy windows) set around the photo-peak. It estimates the scattered photons measured in the main window on a pixel by pixel basis using the counts measured in the two scatter sub-energy windows. In the TEW method, the scatter image, $C_{scatter}$, is defined as:

$$C_{scatter}(x,y) = \left(\frac{C_{left}(x,y)}{W_{left}} + \frac{C_{right}(x,y)}{W_{Right}} \right) \times \frac{W_{photo-peak}}{2} \tag{3.6}$$

where C_{left} and C_{right} are counts in the left and right energy windows next to a photo-peak window with energy width W_{left} and W_{right} respectively. $W_{photo\text{-}peak}$ is the energy width of the photo-peak window, (Figure 3.8).

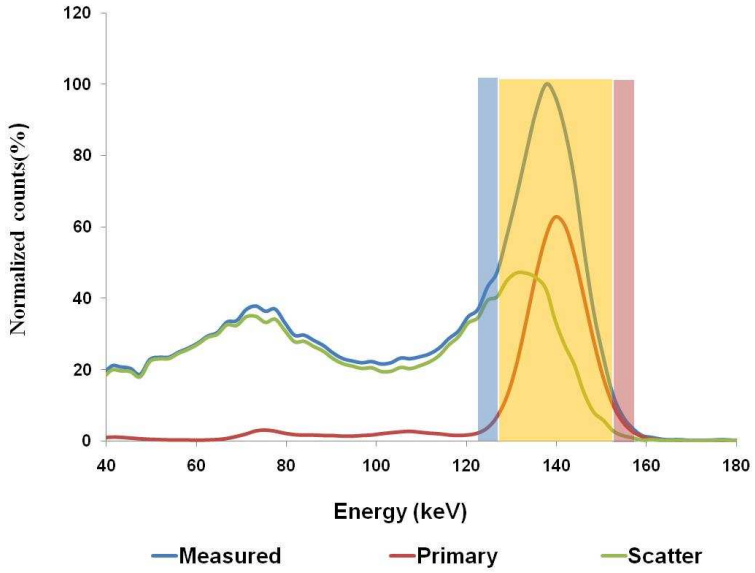

Figure 3.8: *A technetium-99m energy spectrum with the three energy windows W_{left} (**blue**), $W_{photo\text{-}peak}$ (**yellow**)and W_{right}.(**red**).*

Selecting a smaller sub-energy window and placing it just below the photo-peak window can minimize the difference in the distribution of scatter between the scatter - and the photo-peak window. With this arrangement, the two-energy window variant of the TEW method is obtained. The two-energy window variant is useful when down-scatter from a higher energy photon is not present as in the case of imaging solely Tc-99m. In this method, the scatter in a pixel is estimated as the area under a triangle whose height is the average count per keV in the window below the photo-peak window, and whose base is the width of the photo-peak window in keV. The smaller sub-energy window results in fewer counts and therefore a noisier scatter image. Thus heavy low-pass filtering of the scatter estimate is required to reduce the noise in the estimate. Hence it is desirable to apply an

appropriate low-pass filter to the scatter-eliminated measured data (planar images). The primary image, $C_{primary}$ as a scatter-corrected image is estimated as:

$$C_{primary}(x,y) = C_{total}(x,y) - C_{scatter}(x,y) \tag{3.7}$$

where C_{total} is the number of total counts in a photo-peak window.

3.5.2.2 Photon Energy Recovery (PER) method

The theory of Photon Energy Recovery (PER) was developed by Hannequin and Mas (1998). This theory is able to decompose a photo-peak and the scatter components of an energy spectrum by iteratively fitting the spectrum using two-dimensional linear regression.

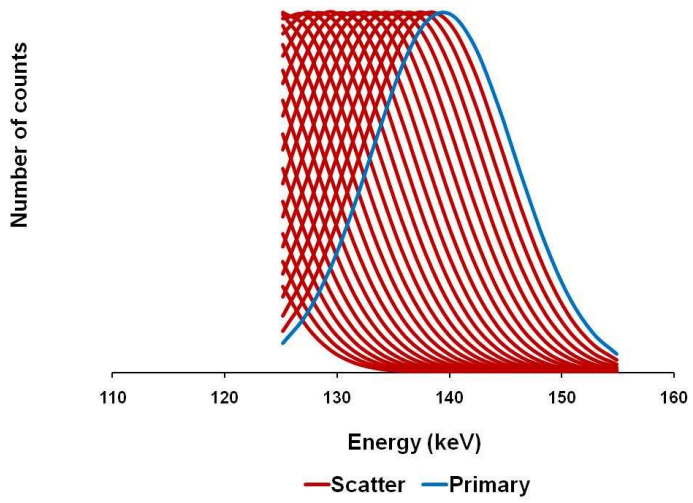

Figure 3.9: *The energy impulse response functions for technetium-99m from 115 to 139 keV (**red**) and the energy impulse response function at 140 keV (**blue**) for Tc-99m.*

In the PER theory, a detected energy spectrum (*DES*) is assumed as a combination of weighted energy impulse response functions (*EIR*), (Figure 3.9).
This relation is given as:

$$DES(E) = \sum_{e=l}^{h} a_e EIR_e(E) \tag{3.8}$$

where l and h are the lowest and highest energies in a photo-peak energy window, a_e is the *e-th* energy component and E is the sub-energy window used to sample an energy spectrum. In PER, the *EIR* is modelled as a Gaussian distribution:

$$\text{standard deviation of } EIR_e = er/(2.35) \tag{3.9}$$

where r is the energy resolution of gamma camera at the photo-peak energy e. It is determined by measuring the energy spectrum of a point source in air with a gamma camera. Once r is determined at an arbitrary energy, other *EIRs* can be created from the Gaussian model. The two-dimensional linear regression of PER is iteratively performed by fitting dual-clustered data in regression steps. This regression is given as:

$$z = ax + by \tag{3.10}$$

At the initial step of the first iteration, *DES* is separated into two clusters:

$$DES = \alpha^1 \sum_{e=l}^{h-1} EIR_e + \beta_h^1 EIR_h \tag{3.11}$$

where α^1 and β_h^1 are coefficients determined by regressing data points acquired from sub-energy windows. After a single regression step, the new *DES* becomes:

$$DES_{new} = DES - \beta_h^1 EIR_h = \alpha \sum_{e=l}^{h-2} EIR_e + \beta_{h-1}^1 EIR_{h-1} \tag{3.12}$$

A single iteration is defined when the regression runs from h to l energies. At the first regression of the second iteration, the regression is given as:

$$DES = \alpha^2 \sum_{e=l}^{h-1} \beta_1^e EIR_e + \beta_h^2 (\beta_h^l EIR_h) \tag{3.13}$$

and the second step of the second iteration can be derived based on Equation (3.12). As the regression is performed after *m* iterations, the reconstructed energy spectrum (*RES*) is presented as:

$$^m RES(E) = \sum_{e=l}^{h} {}^m a_e EIR_e \tag{3.14}$$

where $^m a_e$ is equal to

$$^m a_e = \prod_{n=1}^{m} \beta_e^n \tag{3.15}$$

In PER, a square error after *m* iterations is defined to check the difference between a reconstructed spectrum and a detected spectrum. This error is given as:

$$SE = \sum_{E=L}^{H} (^m RES(E) - DES(E))^2 \tag{3.16}$$

Theoretically, when *RES* is very close to *DES*, *SE* can stop changing in successive iterations. The spectrum theory generated by PER can be a milestone of energy-based scatter correction approaches because it performs scatter correction by decomposing energy components of an energy spectrum rather than extrapolating scatter components from additional energy windows, thus a more robust performance can be expected than other energy-based methods. Performance of PER in correcting simultaneous dual-isotope imaging was published by Hannequin *et al*. (2000). PER is limited by certain assumptions that may restrict the optimal performance of this technique in routine clinical use. Firstly, PER uses a Gaussian distribution to model *EIRs* rather than directly measuring *EIRs* of a gamma camera system. Secondly, an energy window is only sampled in several sub-energy windows which can lead

to unstable solutions when fitting an energy spectrum. Thirdly, the linear regression used by PER does not adequately fit Poisson variance in spectrum samples, thus Poisson noise can limit PER's performance or PER needs a high-count energy spectrum to perform a scatter correction (Hannequin *et al.*, 2001).

3.6 Discussion

Although many different solutions to attenuation corrections have been proposed, practical obstacles exist in the routine clinical implementation of an attenuation correction. One of the problems is that the geometry of SPECT detectors does not always lend itself to the performance of transmissions scans. Even if the geometry is accommodating, custom hardware modifications to the gantry are necessary in order to accommodate these transmission scans. Such hardware changes are often beyond the capability of many nuclear medicine departments due to the high cost involved. Furthermore the gantry does not always permit major modifications. One proposal would be to use a transmission configuration that requires no or limited modifications to the existing gantry system to perform transmission imaging.

Currently, as mentioned in Section 3.3.1, there are a number of radionuclide transmission-based imaging configurations that make use of parallel-hole collimation. The most popular one is the scanning line source mechanism shown in Figure 3.4. Unfortunately, this system requires synchronized mechanical motion of the radionuclide source with the electronic window on the detector. Communication and synchronization between the gamma camera and the moving line source can be challenging. If a multiple line source configuration is used the relative ease of support and collimation of the single scanning line source is compromised by the need for extra support and collimation for the multiple line sources. This additional collimation of the multiple line source array can restrict the gantry motion. A suitable radionuclide transmission-based configuration would be an uncollimated transmission source opposite the parallel-hole collimator as proposed by Bailey *et al.* (1987). Since the non-collimation of the flood source results in broad beam

attenuation coefficients, it would be preferable to collimate the transmission source. However, this configuration would then require large amounts of radioactivity in the transmission source and lacks the flexibility of an uncollimated source.

Our proposal for transmission imaging is an uncollimated, non-uniform, transmission sheet source configuration. The sheet source would be printed on paper with an inkjet printer. This configuration would require modest or no gamma camera modifications and therefore would be appropriate for most gamma cameras and be affordable for most nuclear medicine clinics. The system would require accurate scatter correction in order to produce “narrow beam” attenuation coefficients which are necessary for accurate quantitative SPECT imaging. The construction and evaluation of the printed transmission sheet source with an appropriate scatter correction is the subject of discussion in the next chapters.

3.7 References

Almeida P, Bendriem B, de Dreuille O, Peltier A, Perrot C, Brulon V (1998). Dosimetry of transmission measurements in nuclear medicine: a study using anthropomorphic phantoms and thermoluminescent dosimeters. *Eur J Nucl Med;* **25:** pp1435–1441.

Axelsson B, Msaki B, Israelsson A (1984). Subtraction of Compton-scattered photons in single-photon emission computerized tomography. *J Nucl Med;* **25:** pp490–494.

Bailey DL, Hutton BF, Walker PJ (1987). Improved SPECT using simultaneous emission and transmission tomography. *J Nucl Med;* **28:** pp844–851.

Beekman FJ, Kamphuis C and Viergever MA (1996). Improved SPECT quantitation using fully three-dimensional iterative spatially variant scatter response compensation. *IEEE Trans Med Imag;* **15:** pp491–499.

Beekman FJ, Kamphuis C, Hutton BF, van Rijk PP (1998). Half-fanbeam collimators combined with scanning point sources for simultaneous emissiontransmission imaging. *J Nucl Med;* **39:** pp1996–2003.

Bocher M, Balan A, Krausz Y, Shrem Y, Lonn A, Wilk M, Chisin R (2000). Gamma camera mounted anatomical X-ray tomography: Technology, system characteristics and first images. *Eur J Nucl Med;* **27:** pp619– 627.

Cao Z, Holder L (1998). Effects of the attenuation map used in the Chang algorithm on quantitative SPECT results. *J Nucl Med Tech;* **26:** pp178–185.

Cao ZJ, Tsui BMW (1992). Performance characteristics of transmission imaging using a uniform sheet source with a parallel-hole collimator. *Med Phys;* **19:** pp1205–1212.

Celler A, Sitek A, Stoub E, Hawman P, Harrop R, Lyster D (1998). Multiple line source array for SPECT transmission scans: simulation, phantom, and patient studies. *J Nucl Med;* **39:** pp2183–2189.

Chang LT (1978). A method for attenuation correction in radionuclide computed tomography. *IEEE Trans Nucl Sci;* **25:** pp638–643.

Chang W, Loncaric S, Huang G, Sanpitak P (1995). Asymmetric fan transmission CT on SPECT systems. *Phys Med Biol;* **40:** pp913–928.

Cherry SR, Sorenson JA, Phelps ME (2003a). Interaction of Radiation with Matter. In: "*Physics in Nuclear Medicine"*. 3rd edition, W.B. Saunders company, USA. 2003. pp77–78.

Cherry SR, Sorenson JA, Phelps ME (2003b). Interaction of Radiation with Matter. In: "*Physics in Nuclear Medicine"*. 3rd edition, W.B. Saunders company, USA. 2003. pp80–84.

Cherry SR, Sorenson JA, Phelps ME (2003c). Interaction of Radiation with Matter. In: "*Physics in Nuclear Medicine"*. 3rd edition, W.B. Saunders company, USA. 2003. pp77–78.

Cherry SR, Sorenson JA, Phelps ME (2003d). Single Photon Emission Computed Tomography. In: "*Physics in Nuclear Medicine"*. 3rd edition, W.B. Saunders company, USA. 2003. pp317–319.

Du Raan H, du Toit PD, van Aswegen A, Lötter MG, Herbst CP, van der Walt TN, Otto AC (2000). Implementation of a Tc-99m and Ce-139 scanning line source for attenuation correction in SPECT using a dual opposing detector scintillation camera. *Med Phys;* **27:** pp1523–1534.

Ficaro EP, Fessler JA, Rogers WL, Schwaiger M (1994). Comparison of americium-241 and technetium-99m as transmission sources for attenuation correction of thallium-201 SPECT imaging of the heart. *J Nucl Med;* **35:** pp652–663.

Floyd CE, Jaszczak RJ, Greer KL, Coleman RE (1986). Inverse Monte Carlo as a unified reconstruction algorithm for ECT. *J Nucl Med;* **27:** pp1577–1585.

Frey EC, Tsui BM, Perty JR (1992). Simultaneous acquisition of emission and transmission data for improved thallium-201 cardiac SPECT imaging using a technetium-99m transmission source. . *J Nucl Med;* **33**: pp2238–2245.

Gagnon D, Todd-Pokropek AE, Arsenault A, Dupras G (1989). Introduction to holospectral imaging in nuclear medicine for scatter subtraction. *IEEE Trans Med Imag;* **8:** pp245–250.

Gallowitsch HJ, Sykora J, Mikosch P, Kresnik E, Unterweger O, Molnar M, Grimm G, Lind P (1998). Attenuation-corrected thallium-201 single-photon emission tomography using a gadolinium-153 moving line source: clinical value and the impact of attenuation correction on the extent and severity of perfusion abnormalities. *Eur J Nucl Med;* **25:** pp220–228.

Gilland DR, Jaszczak RJ, Greer KL, Coleman RE (1998). Transmission imaging for nonuniform attenuation correction using a three-headed SPECT camera. *J Nucl Med;* **39:** pp1105–1110.

Glick S, Xia W (1997). Iterative restoration of SPECT projection images. *IEEE Trans Nucl Sci;* **44:** pp204–211.

Gullberg GT, Morgan HT, Zeng GL, Christian PE, Di Bella EVR, Tung C-H, Maniawski PJ, Hsieh YL, Datz FL (1998). The design and performance of a simultaneous transmission and emission tomography system. *IEEE Trans Nucl Sci;* **45:** pp1676–1698.

Hamill JJ, DeVito RP (1989). Scatter reduction with energy weighted acquisition. *IEEE Trans Nucl Sci;* **36:** pp1334–1339.

Hannequin P, Mas J (1998). Photon energy recovery: a method to improve the effective energy resolution of gamma cameras. *J Nucl Med;* **39:** pp555–562.

Hannequin P, Mas J, Germano G (2000). Photon energy recovery for crosstalk correction in simultaneous 99mTc/201Tl imaging. *J Nucl Med*; **41:** pp728–736.

Hannequin P, Weinmann P,Mas J, Vinot S (2001). Preliminary clinical results of photon energy recovery in simultaneous rest Tl-201/stress Tc-99m sestamibi myocardial SPECT. *J Nucl Cardiol;* **8:** pp144–151.

Hollinger EF, Loncaric S, Yu D-C, Ali A, Chang W (1998). Using fast sequential asymmetric fanbeamtransmission CT for attenuation correction of cardiac SPECT imaging. *J Nucl Med;* **39:** pp1335–1344.

Huda W, Scalzetti EM, Roskopf M (2000). Effective doses to patients undergoing thoracic computed tomography examinations. *Med Phys;* **27**: pp838–844.

Hutton BF (1997). Cardiac single-photon emission tomography: is attenuation correction enough? *Eur J Nucl Med;* **24:** pp713–715.

Ichihara T, Ogawa K, Motomura N, Hasegawa H, Hashimoto J, Kubo A (1993). Compton-scatter compensation using the triple energy window method for single and dual isotope SPECT. *J Nucl Med;* **34:** pp2216–2221.

Jaszczak RJ, Whitehead FR, Lim CB, Coleman RE (1982). Lesion detection with single-photon emission computed tomography (SPECT) compared with conventional imaging. *J Nucl Med;* **23:** pp97–102.

Jaszczak RJ, Greer KL, Floyd CE, Harris CC, Coleman RE (1984). Improved SPECT quantification using compensation for scattered photons. *J Nucl Med;* **25:** pp893–900.

Jaszczak RJ, Gilland DR, Hanson MW, Jang S, Greer KL, Coleman RE (1993). Fast transmission CT for determining attenuation maps using a collimated line source, rotatable air-copper-lead attenuators and fanbeam collimation. *J Nucl Med;* **34:** pp1577–1586.

Kadrmas DJ, Frey EC, Karimi SS, Tsui BMW (1998). Fast implementations of reconstruction-based scatter compensation in fully 3D SPECT image reconstruction. *Phys Med Biol;* **43:** pp857–874.

Kadrmas DJ, DiBella EVR, Huesman RH, Gullberg GT (1999). Analytical propagation of errors in dynamic SPECT: estimators, degrading factors, bias and noise. *Phys Med Biol;* **44:** pp1997–2014.

King MA, Hademenos GJ, Glick SJ (1992). A dual-photopeak window method for scatter correction. *J Nucl Med;* **33:** pp605–612.

King MA, Tsui BMW, Pan T-S (1995). Attenuation Compensation for Cardiac Single-Photon Emission Computed Tomographic Imaging: Part 1. Impact of Attenuation and Methods of Estimating Attenuation Maps. *J Nucl Cardiol;* **2:** pp513–524.

King MA, Xia W, de Vries DJ, Pan T-S, Villegas BJ, Dahlberg S, Tsui BMW, Ljunberg MH Morgan HT (1996). A Monte Carlo investigation of artifacts caused by liver uptake in SPECT perfusion imaging with Tc-99m-labelled agents. *J Nucl Cardiol;* **3:** pp18–29.

Koral KF, Wang X, Rogers WL, Clinthone NH, Wang X (1988). SPECT Compton-scattering correction by analysis of energy spectra. *J Nucl Med;* **29:** pp195–202.

LaCroix KJ, Tsui BMW (1999). Investigation of 90 dual-camera half-fanbeam collimation for myocardialSPECT imaging. *IEEE Trans Nucl Sci;* **46:** pp2085–2092.

Lang TF, Hasegawa BH, Liew SC, Brown JK, Blankespoor SC, Reilly SM, Gingold EL, Cann CE (1992). Description of a prototype emission-transmission computed tomography imaging system. *J Nucl Med;* **33:** pp1881–1887.

Lowry CA, Cooper MJ (1987). The problem of Compton scattering in emission tomography: a measurement of its spatial distribution. *Phys Med Biol;* **32:** pp1187–1191.

Maeda H, Itoh H, Ishii Y, Makai T, Todo G, Fujita T, Torizuka K (1981). Determination of the pleural edge by gamma-ray transmission computed tomography. *J Nucl Med;* **22:** pp815–817.

Malko JA, Van Heertum RL, Gullberg GT, Kowalsky WP (1985). SPECT liver imaging using an iterative attenuation correction algorithm and an external flood source. *J Nucl Med;* **26:** pp701–705.

Meikle SR, Hutton BF, Bailey DL (1994). A transmission dependent method for scatter correction in SPECT. *J Nucl Med;* **35:** pp360–367.

Narita Y, Eberl S, Iida H, Hutton BF, Braun M, Nakamura T, Bautovich G (1996). Monte Carlo and experimental evaluation of accuracy and noise properties of two scatter correction methods for SPECT. *Phys Med Biol;* **41:** pp2481–2496.

Ogawa K, Harata Y, Ichihara T, Kubo A, Hashimoto S (1991). A practical method for position-dependent Compton-scatter correction in single photon emission CT. *IEEE Trans Med Imag;* **10:** pp408–412.

Ogawa K, Nishizaki N (1993). Accurate scatter compensation using neural networks in radionuclide imaging. *IEEE Trans Nucl Sci;* **40:** pp1020–1024.

Ogawa K. Image distortion and correction in single photon emission CT (2004). *Ann of Nucl Med;* **18:** pp171–185.

Pan X, Wong W, Chen C, Liu J (1993). Correction for photon attenuation in SPECT: analytical framework, average attenuation factors, and a new hybrid approach. *Phys Med Biol;* **38:** pp1219–1234.

Patton JA, Delbeke D, Sandler MP (2000). Image fusion using an integrated, dual-head coincidence camera with x-ray tube-based attenuation maps. *J Nucl Med;* **41:** pp1364–1368.

Pretorius PH, van Rensburg AJ, van Aswegen A, Lötter MG (1993). The channel ratio method of scatter correction for radionuclide image quantitation. *J Nucl Med;* **34:** pp330–335.

Preuss R, Weise R, Lindner O, Fricke E, Fricke H, Wolfgang B (2008). Optimisation of protocol for low dose CT-derived attenuation correction in myocardial perfusion SPECT imaging. *Eur J Nucl Med Mol Imaging;* **35:** pp1133–1141.

Rajeevan N, Zubal I, Ramsby S, Zoghbi S, Seibyl J, Innis R (1998). Significance of nonuniform attenuation correction in quantitative brain SPECT imaging. *J Nucl Med;* **39:** pp1719–1726.

Shotwell M, Singh BM, Fortman C, Bauman BD, Lukes J, Gerson MC (2002). Improved coronary disease detection with quantitative attenuation-corrected Tl-201 images. *J Nucl Cardiol;* **9:** pp52–62.

Sorensen JA (1974) Quantitative measurement of radioactivity in vivo by whole-body counting. *Instrum Nucl Med;* **2:** pp311–341.

Stodilka R, Kemp B, Msaki P, Prato F, Nicholson R (1998**a**). The relative contributions of scatter and attenuation corrections toward improved brain SPECT quantification. *Phys Med Biol;* **43:** pp2991–3008.

Stodilka RZ, Kemp BJ, Prato FS, Nicholson RL (1998**b**). Importance of bone attenuation in brain SPECT quantification. *J Nucl Med;* **39:** pp190–197.

Tan P, Bailey DL, Meikle SR, Eberl S, Fulton RR, Hutton BF (1993). A scanning line source for simultaneous emission and transmission measurements in SPECT. *J Nucl Med;* **34:** pp1752–1760.

Tsui BMW, Gullberg GT, Edgerton ER, Ballard JG, Perry JR, McCartney WH, Berg J (1989). Correction of nonuniform attenuation in cardiac SPECT imaging. *J Nucl Med;* **28:** pp497–507.

Tsui BMW, Zhao XD, Gregoriou GK, Lalush DS, Frey EC, Johnston RE, McCartney WH (1994**a**). Quantitative cardiac SPECT reconstruction with reduced image degradation due to patient anatomy. *IEEE Trans Nucl Sci;* **41:** pp2838–2844.

Tsui BMW, Zhao XD, Frey EC, McCartney WH (1994**b**). Quantitative single-photon emission computed tomography: basics and clinical considerations. *Semin Nucl Med;* **24:** pp38–65.

Tsui BMW, Frey EC, LaCroix KJ, Lalush DS, McCartney WH, King MA, Gullberg GT (1998). Quantitative myocardial perfusion SPECT. *J Nucl Cardiol;* **5:** pp507–522.

Tung C-H, Gullberg GT, Zeng GL, Christian PE, Datz FL, Morgan HT (1992). Nonuniform attenuation correction using simultaneous transmission and emission converging tomography. *IEEE Trans Nucl Sci;* **39:** pp1134–1143.

Van Laere K, Koole M, Kauppinen T, Monsieurs M, Bouwens L, Dierck R (2000). Nonuniform transmission in brain SPECT using 201Tl, 153Gd, and 99mTc static line sources: anthropomorphic dosimetry studies and influence on brain quantification. *J Nucl Med;* **41:** pp2051–2062.

Zaidi H, Hasegawa B (2003). Determination of the attenuation map in emission tomography. *J Nucl Med;* **44:** pp291–315.

Chapter 4

Production and Evaluation of a Radioactive Flood Source for Transmission Imaging

4.1 Introduction

Compton scatter, due to high tracer uptake in the liver, stomach and bowl can compromise the diagnostic accuracy of conventional Single Photon Emission Computed Tomography (SPECT). Scatter from organs with high tracer uptake into the inferior wall of the left ventricle can lead to an increase in the counts in the inferior wall. Artefacts due to the reconstruction algorithm can also result in a decrease in the count density in structures close to organs with high tracer uptake. It is therefore evident that for SPECT imaging corrections for attenuation and scatter are essential to ensure qualitative and quantitative accurate imaging (Nuyts *et al.*, 1995). The most reliable method to determine attenuation maps for attenuation correction is by using transmission measurements with either a radionuclide or a Computed Tomography (CT) scanner (Zaidi and Hasegawa, 2003). As was discussed in Chapter 3 transmission measurements with radionuclides predominantly use gadolinium-153 (97 keV, 103 keV, 241.6 d) as the external source but can also use americium-241 (59 keV, 432.2 y), gold-195 (99 keV, 130 keV, 183.0 d), cobalt-57 (122 keV,137 keV, 271.8 d), barium-133 (356 keV, 10.52 y) and cerium-139 (165.9 keV, 137.7 d).

The geometry of the transmission source can vary from extended flood sources to line sources and point sources, combined with the use of parallel or converging collimators. From the discussion in Chapter 3 it is evident that each of these source geometries along with its collimators has its unique advantages and drawbacks.

As discussed in Chapter 3 early designs of transmission systems for SPECT cameras used uncollimated flood or sheet sources (Bailey *et al.*, 1987). The main advantage of this

configuration is that the source fully irradiates the opposite detector. This configuration also requires no source motion other than that provided by the rotation of the gamma camera gantry. This transmission configuration also has limitations associated with the high proportion of scattered photons in the transmission data due to the broad beam imaging conditions. As a result, the attenuation map estimates an effective linear attenuation coefficient rather than the value that would be calculated from narrow beam geometry. This difficulty has been partly overcome by collimating the transmission source to produce a geometry that more accurately represents narrow beam transmission geometry (Cao and Tsui, 1992). Collimation of the transmission source however requires gamma camera alteration and much higher source activity. Lower flood source activity along with lower cost due to limited gamma camera alterations has renewed the interest in uncollimated flood sources (Kojima *et al.*, 2004) for transmission imaging. Kojima *et al.* (2004) have also shown that with an uncollimated flood source a scatter correction would reduce the scatter contribution in the transmission image. In our clinic there is currently no mechanism available for transmission imaging. The need to perform transmission computed tomography has forced us to investigate the possibility of developing a transmission system for the existing gamma cameras in our clinic. The proposal in this chapter is to use an uncollimated printed source as a transmission source.

The transmission flood sources were designed and produced in-house for the transmission systems. These transmission sources were printed on paper with a digital inkjet printer and therefore the production process and printed sources had to be evaluated. Printed transmission flood sources have a number of potential advantages over conventional transmission sources. These potential advantages are firstly that the activity distribution of the radioactive source can be modified to be suitable for a specific patient. This will result in a more uniform transmission image of the patient. An important advantage of this configuration is that the distribution of activity in the printed source can be tailored to the attenuation in the human body minimising the problem encountered when too few counts are recorded in some pixels of the transmission scan. The activity distribution of printed flood sources is more flexible than the fixed series of line sources proposed by Celler *et al.*

(1998). Secondly, the printed radioactive source can be manufactured at low cost to evaluate the use of different activity distributions in the transmission source. After the evaluation an optimal activity distribution for the transmission source can be identified. In this study Tc-99m has been used for the preliminary evaluation of a transmission source; however, a long lived radionuclide may be used once the required non-uniform configuration has been determined. Another advantage of a printed uncollimated transmission flood source is that since the weight of the paper source is negligible, older existing gamma cameras can easily be customized to allow transmission imaging. Kojima *et al*. (2004) have also shown that with an uncollimated non-uniform source, transmission computed imaging time can be reduced. This reduction in transmission imaging time would result in a lower radiation exposure to the patient in comparison to a uniform transmission source.

The disadvantages associated with the use of an uncollimated transmission source include the additional radiation dose to the patient (Cao and Tsui, 1992) compared to using a collimated source. Another weakness of an uncollimated transmission source is the added scattered events that will lead to broad beam attenuation coefficient values. Scattered events in the transmission data can be corrected for by applying a scatter correction to the transmission data as being proposed by Kojima *et al.* (2004).

In this chapter the production and construction of a transmission flood source was investigated. Tc-99m was used for the initial evaluation of the constructed flood source.

4.2 Material and methods.

4.2.1 Flood source construction.

The ink used to print the flood source was obtained by adding a well-mixed solution of black ink and Tc-99m pertechnetate to the cartridge of a Hewlett-Packard inkjet printer (HP1220C). The cartridge of the printer was altered by adding a tightly sealed plastic plug

to the cartridge, (Figure 4.1). This allow for easy filling of the cartridge which is important to maintain low radiation risk to the user.

Figure 4.1: *Prototype of the ink cartridge that was altered to allow for easy filling by adding a solution of black ink and Tc-99m.*

Commercial MS Powerpoint (Microsoft™) software was used to create a digital image of the transmission source on the screen of a personnel computer that was representative of the radioactive distribution required. The required radioactive distribution was then printed on A4 sized paper (80 $g.m^{-2}$) using the radioactive ink mixture. All radioactive sources were placed in a plastic sheath to prevent them causing any possible contamination. Imaging was performed with a GE Starcam 400AT (General Electric Medical Systems, Milwaukee) camera fitted with a low energy all purpose collimator (LEAP) and IM512P acquisition software (Alfanuclear SAIYC, Buenos Aires).

4.2.2 Transmission source configuration

The printed transmission flood source was fixed to the gamma camera by a frame attached to the detector of the gamma camera. A LEAP collimator was used for imaging, (Figure 4.2). The frame which supports the printed flood source attaches directly to the edge of the collimator and positions the printed flood source 0.75 m from the collimator.

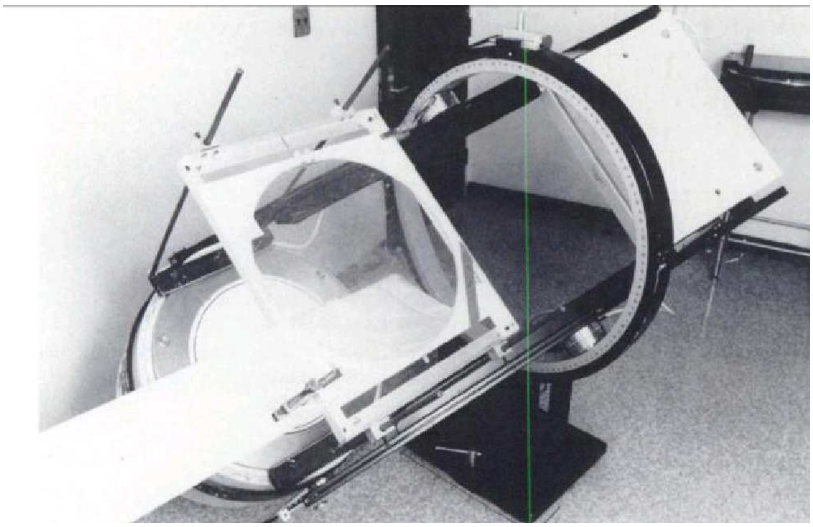

Figure 4.2: *A tomographic gamma camera with transmission source frame.*

At a distance of 0.75 m, the printed source and frame does not interfere with patient positioning or compromise patient-to-detector distance for optimal resolution. This configuration also ensures that the patient is always located between the transmission source and the gamma camera detector. The GE Starcam 400AT gamma camera has a manual counter-weight mechanism to support any additional weight which is added to the gamma camera detector. This manual counter-weight mechanism was used to balance the gamma camera detector when the flood source configuration was fixed to the detector of the gamma camera.

4.2.3 Characteristics of the flood source

4.2.3.1 Amount of ink and radioactivity deposited

To predict the amount of radioactivity required to obtain a specific activity on the final printed flood source, it is necessary to (i) determine the amount of ink deposited per unit area on the printout and (ii) how much activity should be added.

The amount of ink was obtained as follows: the ink cartridge was filled with ±5 ml non-radioactive ink, weighed and then used to consecutively print four uniform flood source

phantoms of 22.8 × 16.7 cm^2. The cartridge was weighed after each individual printout. The average mass of ink required for each printed flood source phantom and subsequently the average mass of ink deposited per unit area was determined.

To ensure that the cartridge was empty, additional flood sources were printed until the ink was used up.

The following procedure was then followed to predict the amount of radioactivity per printed phantom. The radioactive ink was prepared by adding a known activity of Tc-99m to ±10 ml ink. The radio-active ink was divided into two syringes of ±5 ml each. The radioactive ink in the first syringe was added to a cartridge (refill 1) and four uniform radioactive flood sources, with the same dimensions as above, were printed. The cartridge was weighed before and after adding the ink to determine the mass of ink added. The predicted activity (*PA*) in MBq deposited on each printed flood source was estimated using the following formula:

$$PA = \frac{A_c * m_p}{m_t} \qquad (4.\ 1)$$

where A_c is the activity in the cartridge (MBq), m_p is the average mass of ink deposited for each flood source (mg), and m_t is the total mass of the Tc-99m ink (mg) in the cartridge. The procedure was repeated using a second syringe and this batch was named refill 2. This procedure, starting with a non-radioactive 'dry' cartridge was repeated twice in order to evaluate the reproducibility. Two data sets were obtained, each with two refills, refill 1 and refill 2, with four flood sources each.

The activity of each printed flood source (*MA*) was subsequently measured in a source calibrator. The printed flood source was folded to fit into the source calibrator. The measured values were corrected for decay and were compared to the *PA* values.

4.2.3.2 Uniformity of printed flood sources

Five radioactive flood sources (22.8 × 16.7 cm^2) were created on a personnel computer and printed as describe in Section 4.2.1. Approximately 1200 MBq (32 mCi) Tc-99m was deposited equally onto each paper sheet with the inkjet printer. Each source inside its plastic sheath was placed directly on the camera detector and imaged using a 64 × 64 matrix until a maximum pixel count of 10 000 counts was obtained. The integral (IU) and differential uniformities (DU) were calculated according to NEMA specifications (NEMA 2001) for each flood source in the central 75% field of the radioactivity distribution.

Furthermore, the system uniformity of the camera was determined according to the NEMA protocol (NEMA 2001) using a Co-57 (C-Thru Series™) flood source (62 × 42 cm^2).

The Co-57 flood source image was obtained under the same imaging conditions as mentioned before. The IU and DU were calculated for the central field of view (CFOV) and also for an area similar in size to that used to calculate the uniformity of the printed flood sources.

The uniformity was also evaluated by obtaining X- and Y-profiles through one of the printed flood source images. The X-profile represented the count profile perpendicular to the long axis of the printed lines and the Y-profile direction was parallel with the individual lines printed on the phantom. The profiles selected were 5 pixels wide, representing a width of approximately 30 mm. A camera-independent method was also used to evaluate the uniformity of three of the printed flood source phantoms. A collimated 50 mm diameter NaI(Tl) crystal scintillation detector connected to a multi-channel analyzer (MCA) system, (Figure 4.) was used for the evaluation. The face of the crystal was shielded with a 25 mm thick lead collimator with a single 6mm diameter hole centred on the crystal. The collimated detector was manually scanned across the printed phantom.

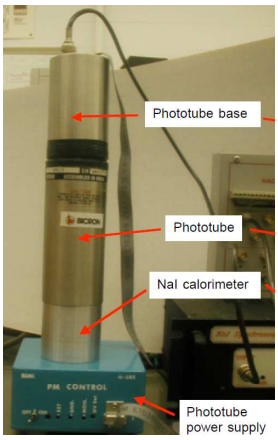

Figure 4.3: *A collimated scintillation detector connected to multi-channel analyzer system.*

A 15% energy window was centred on the 140 keV Tc-99m photo-peak on the spectra obtained from the MCA. The MCA was set to acquire 10 000 counts in the selected window and the acquisition time was noted. Accordingly, the count rate was calculated. For each phantom 30 readings spaced equally across the area of the phantom were obtained. The count rates were decay corrected and an IU value calculated. No filtering was applied to the data before calculating the IU value.

4.2.3.3 Composite flood sources

All the above paper flood sources were printed on A4-sized sheets. In certain cases, however, larger flood sources might be required. A A3-sized source could for instance be required for a large FOV camera. An A3-sized composite flood source was thus created by combining two A4-sized flood sources. Three A3-sized composite sources were constructed for evaluation. Images of the A3-sized composite flood sources were acquired with similar parameters as in Section 4.2.3.2. The IU and DU were calculated for each source.

4.2.3.4 Optimal flood source

One of the limitations of a uniform transmission source is that the same activity is used across the whole range of tissue thicknesses of the patient. A constraint for a transmission

source is that the radiation yield must be adequate to produce sufficient count rates across the patient. A high yield from the equally distributed activity is needed from a uniform transmission source to provide sufficient counts across the patient. This high yield can cause substantial dead time losses at the edges of the gamma camera detector, where the uniform source irradiates only the periphery of the body and attenuation is low or null. Therefore for transmission imaging the optimum flood source would be one that yields a constant signal-to-noise ratio across the entire width of the target object. The ease of creating an optimum flood source was illustrated by using a cylindrical phantom, 20 cm in diameter, as a target object. A uniform flood source (185 MBq) was printed on A3 size paper as describe before and attached to the flood source frame of the gamma camera. The water filled cylindrical phantom (Figure 4.4) was placed on the collimator of the detector. A transmission image was acquired in a 128 × 128 matrix with a total of 9 million counts.

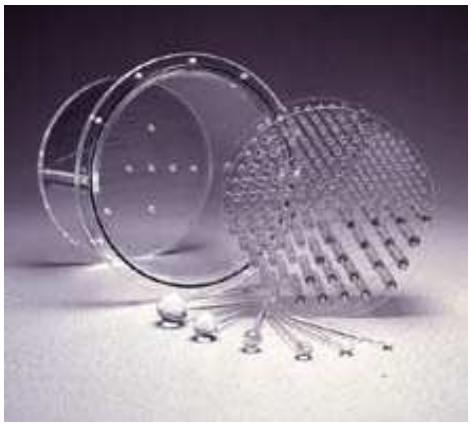

Figure 4.4: *The empty water phantom.*

The transmission image was converted to JPEG image format and imported in CorelDRAW®. The colour display of the acquired transmission image was inverted and the inverted image was printed with a mixture of radioactive ink on A3 size paper. The printed source of the inverted transmission image was attached to the flood source frame and the water filled cylindrical phantom was position between the flood source and the detector of the gamma camera. A transmission image of the phantom (128 × 128 matrix) was acquired until a maximum pixel count of 10 000 counts was reached. A profile was drawn in the X-direction through the acquired transmission image.

4.3 Results

4.3.1 Characteristics of the flood source

4.3.1.1 Amount of ink and radioactivity deposited

The average mass of ink used per flood source phantom (area 22.8 × 16.7 cm^2) was 956 mg ± 3.2%. The mass of ink deposited per unit area was therefore 2.511 $mg.cm^{-2}$. Table 4.1 shows the mass (m_t) and the activity (A_c) of the radioactive ink in the cartridge, the activity in the cartridge and the predicted amount of activity (*PA*) that will be printed per flood source phantom for each measurement set. The measured activity (*MA*) per phantom, as well as the percentage difference between the *PA* and *MA* (*PA*–*MA*%) for each printed phantom are also included in Table 4.1. The results are shown for the two data sets for both refills. The average and standard deviation for phantoms 2 to 4 are also shown for each batch. The standard deviation (St Dev) calculated for the *MA* for print 2 to 4 of the different batches were all acceptable. The average *MA* also compared well with the *PA*. The results obtained with the first printed phantom in the different sets were not always optimal. A difference of more than 10% between the *PA* and *MA* was observed for the first printed phantoms in set 1 (Refill 1) as well as for set 2 (Refill 1). This was due to the fact that the cartridge was not completely empty when the first radioactive ink was added to the cartridge. There is a small chamber at the bottom of the cartridge that contains approximately 300 mg of ink. This chamber does not empty even if no more ink is available for printing. The ink in this chamber does not mix with the radioactive ink originally added to the cartridge. The predicted activity that will be printed is therefore not accurate for the first print after the cartridge has been filled with radioactive ink. The prediction thereafter is accurate, since the remainder of the radioactive ink is uniformly mixed.

Table 4.1: *A comparison between predicted (PA) and measured activity (MA) printed on different flood sources.*

	Set 1			
	Refill 1	*PA–MA* (%)	Refill 2	*PA–MA* (%)
m_t (g):	5.92		6.38	
A_c (MBq):	339.62		407.26	
PA (MBq)	53.35		63.01	
MA (MBq)				
Print 1	26.12	−51.0	61.20	−2.9
Print 2	48.88	−8.4	64.75	2.8
Print 3	53.02	−0.6	64.30	2.1
Print 4	52.95	−0.8	64.30	2.1
Avg(2–4)	51.62	−3.3	64.45	2.3
St Dev(2–4)	2.37	4.4	0.26	0.4

	Set 2			
	Refill 1	*PA–MA* (%)	Refill 2	*PA–MA* (%)
m_t (g):	4.99		5.28	
A_c (MBq):	335.81		421.65	
PA (MBq)	64.42		74.26	
MA (MBq)				
Print 1	41.55	−35.5	71.97	−3.1
Print 2	65.53	1.7	78.55	5.8
Print 3	66.16	2.7	78.85	6.2
Print 4	65.60	1.8	74.20	0.1
Avg(2–4)	65.75	2.1	77.19	4.0
St Dev(2–4)	0.35	0.6	2.61	3.5

The average percentage difference between *PA* and *MA* excluding the first printed phantom for all the data obtained from the four refills was 0.8 ± 3.5%. The first printed phantoms of the second batches show a more accurate prediction of the activity printed for each phantom compared to the first batches. This is due to the fact that the chamber at the front

of the cartridge still contains radioactive ink from the previous time the cartridge was filled. From the results shown in Table 4.1 it is recommended that the first printout be discarded since the correct amount of activity is not deposited in the phantom and this print will also not be uniform since the initial ink printed is not mixed with radioactivity.

In our opinion, that in the case where flood sources need to be printed to evaluate the extrinsic uniformity of the gamma camera or for being used as transmission sources, an accuracy of the predicted activity of less than 10% is sufficient in order to obtain the required count rate on the camera. This accuracy can be obtained with the printed phantoms.

4.3.1.2 Uniformity of printed flood sources

The five printed Tc-99m flood sources that were used for this evaluation were obtained after proper mixing has taken place in the cartridge. The IU and DU obtained with the NEMA method (Co-57 flood source) for the useful field of view (UFOV) was 4.11% and 2.68%, respectively. The IU (2.10%) of the central area of the Co-57 flood source corresponds well with the average IU of all the printed flood sources (2.29 ± 0.67%). Similar results were obtained for the DU (Co-57 flood source: 1.50%; printed flood source: 1.50 ± 0.23%).

Figure 4.5 shows the X- and Y-profiles obtained through one of the flood source images. Good uniformity across the phantom is achieved in the X- and Y-direction. The average IU obtained from the scintillation detector collimated to 6 mm was 3.2 ± 1.3%. Inherent to this value is a 2% error due to counting statistics (10 000 counts were acquired for each reading). Since no filtering was applied to the data before calculating the IU it can be assumed that the uniformity due to printing variations is in the order of 1.2%.

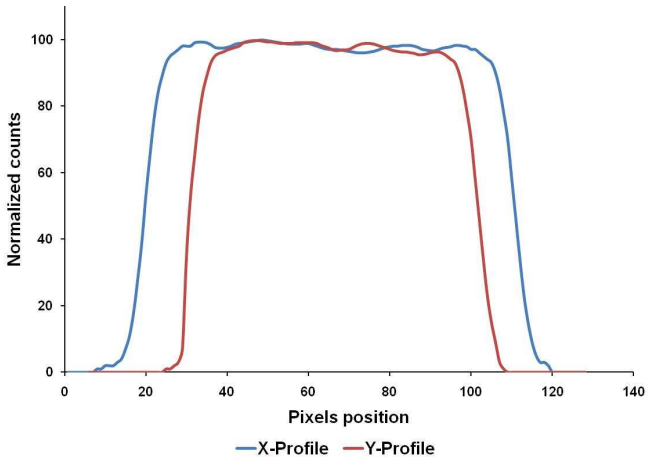

Figure 4.5: *X- and Y-profiles obtained through one of the flood source images.*

The uniformity obtained by Larsson *et al.* (2000) for circular printed phantoms (diameter 95mm) was calculated as the standard deviation of the pixel count variation. They reported a standard deviation of 1.2%.

4.3.1.3 Composite flood sources

Table 4.2 shows the IU and DU values obtained from the A3-sized composite flood source images.

Table 4.2: *Integral uniformity (IU) and differential uniformity (DU) values obtained for the three A3-sized composite flood phantoms.*

	IU (%)	DU (%)
Composite phantom 1	3.54	1.89
Composite phantom 2	3.27	2.28
Composite phantom 3	3.20	1.30
Average ± standard deviation	3.34 ± 0.18	1.82 ± 0.49

Although the IU and DU for the joined composite were slightly higher than the average values for A4-printed flood sources in Section 4.3.1.2, the values were still acceptable when compared to the uniformity values of the NEMA protocol using the Co-57 flood source (IU 4.1% and DU 2.68%). The better uniformity values with the printed flood

source can be explained by the smaller area that is covered by these sources. The Co-57 flood source covered the whole detector, while the A3-sized printed flood source covered 68% of the detector.

4.3.1.4 Optimum flood source

Figure 4.6.(a) shows the transmission image of the water filled cylindrical phantom acquired with a uniform printed flood source.

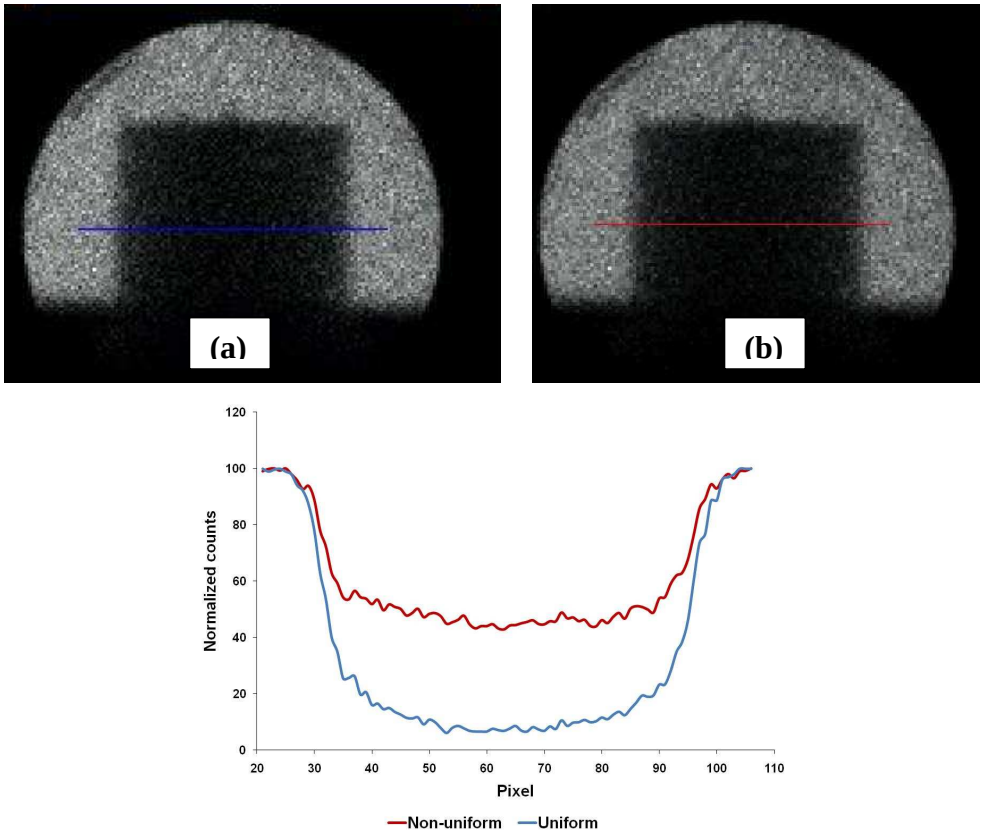

Figure 4.6: *Transmission image of a water filled cylindrical phantom and its corresponding count rate profile obtained through the transmission image in the X-direction acquired with a gamma camera fitted with a (a) uniform and (b) non-uniform printed flood source.*

It is evident from the corresponding X- profile of the uniform water phantom that too few counts were recorded in pixels in the central part of the transmission image. This emphasizes the problem encountered with uniform line or flood sources with too few counts in the central areas of the transmission image as describe by Celler *et al.* (1998).

From the X-profile obtained from the transmission image of the water filled cylindrical phantom acquired with a non-uniform printed flood source shown in Figure 4.6.(b) it is evident that more counts were obtained in central part of the transmission image. This was achieved by depositing higher amounts of activity in the central part of the printed non-uniform flood source.

4.4 Discussion

It was found that the activity for the first printed flood source after refilling the cartridge could not be predicted accurately. Therefore the first flood source printed after refilling the cartridge was discarded and the subsequent printed flood sources were used. The deposition of the amount of radioactivity for these subsequent printed flood sources could be predicted to an acceptable level. This indicates that the activity printed was reproducible. The uniformity of the printed sources compared well to the uniformity values obtained with a Co-57 flood source indicating acceptable printing uniformity. This was confirmed by the X-profile and Y-profile through the image of a printed flood source that was comparable with one another. The camera-independent method using the scintillation detector indicated an IU of 1.3%. We recommend that an independent method like this should be used to evaluate the uniformity of the phantoms. This is essential if it is required to use the phantoms for obtaining uniformity correction maps for SPECT imaging where a 2.0% uniform flood source is required.

It was also shown that joining two A4-size phantoms to create a larger composite phantom does not significantly affect the uniformity attained. It should therefore be possible to create any size phantom, suggesting that routine uniformity corrections could also be performed on any gamma camera using such printed phantoms. The uniformity of a 95 mm diameter circular printed radioactive phantom was reported (Larsson *et al.*, 2000); however a camera-independent measured uniformity value was not reported. The creation of composite phantoms was also not discussed. We have demonstrated that affordable phantoms can easily be created in any department where a standard PC and inkjet printer

are available to evaluate system uniformity and resolution. We have not experienced any contamination of radioactivity. Due to the half-life of Tc-99m (6.02 h), these phantoms need to be printed on a need-to-have basis. Long-lived radio-nuclides may be considered, however special radiation safety precautions should then be followed. Since this method appears to be very versatile it should in principle be possible.

In this study it has been demonstrated that any distribution of activity in the flood source can be attained by using an inkjet printer fitted with a cartridge filled with a mixture of ink and radioactivity. A non-uniform flood source can shorten the transmission acquisition time and lower the radiation dose to the patient. The advantages of a non-uniform transmission source has led to the design of the multiple line source (MLS) configuration by Celler *et al.* (1998). The MLS configuration has illustrated the important advantage of a non-uniform transmission source by reducing the problem encountered by uniform transmission sources when too few counts are recorded in some pixels of the transmission scan. Limitations of the MLS system are that its activity distribution is fixed; it is not readily available and cannot be fitted to all gamma cameras. This has led to a more flexible design by Kojima *et al.* (2004) which is less expensive and could be fitted to most gamma cameras. Creating a non-uniform printed flood source with an inkjet printer has certain advantages over the above mentioned methods. Firstly it allows for low cost, high quality production of radioactive flood sources. Secondly it enables the user to simply alter the activity distribution of the printed transmission source to provide a more uniform transmission image. Problems associated with the use of an uncollimated transmission source are the added scattered events that will lead to broad beam attenuation coefficient values and additional radiation dose to the patient. These problems encountered with uncollimated transmission sources shall be the purpose of the study in the next chapter.

4.5 References

Bailey DL, Hutton BF, Walker PJ (1987). Improved SPECT using simultaneous emission and transmission tomography. *J Nucl Med;* **28:** pp844–851.

Cao Z, Tsui BM (1992). Performance characteristics of transmission imaging using a uniform sheet source with parallel-hole collimation. *Med Phys;***19:** pp1205–1212.

Celler A, Sitek A, Stoub E, Hawman P, Harrop R, Lyster D (1998). Multiple line source array for SPECT transmission scans: simulation, phantom and patient studies. *J Nucl Med*; **39:** pp2183–2189.

Kojima A, Matsumoto M, Tomiguchi S, Katsuda N, Yamashita Y, Motomura N (2004). Accurate scatter correction for transmission computed tomography using an uncollimated line array source. *Ann Nucl Med;* **18:** pp45–50.

Larsson SA, Jonsson C, Pagani M, Johansson L, Jacobson H (2000). A novel phantom design for emission tomography enabling scatter- and attenuation-'free' SPECT imaging. *Eur J Nucl Med;* **27:** pp131–139.

Nuyts J, Dupont P, Van den Maegdenbergh V, Vleugels S, Suetens P, Mortelmans L (1995). A study of the liver-heart artifact in emission tomography. *J Nucl Med;* **36:** pp133–139.

National Electrical Manufacturers Association (NEMA) (2001). *Performance Measurements of Scintillation Cameras.* (Washington, D.C. National Electrical Manufacturers Association).

Zaidi H, Hasegawa B (2003). Determination of the attenuation map in emission tomography. *J Nucl Med;* **44:** pp291–315.

Chapter 5

Evaluation of an Uncollimated Printed Paper Transmission Source used under Scatter Limiting Conditions

5.1 Introduction

In order to apply the correction accurately, attenuation maps containing detailed information about the density distribution in the body are required. Attenuation maps can be obtained of the person or object being imaged by using transmission imaging. Transmission images can be obtained with either an external radionuclide source or computed tomography (CT) with an X-ray source (Delpon *et al.*, 2003; Fleming *et al.*, 2003). It is important to realise that the X-rays emitted in CT are polychromatic and the attenuation coefficient depends on the photon energy. The CT numbers have to be converted to the gamma-ray linear attenuation coefficients of interest by a table look-up method. Another matter for consideration is that CT generally has a higher spatial resolution and is reconstructed using a finer image matrix than Single Photon Emission Computed Tomography (SPECT) images. Therefore the CT images require down-sampling to the same image matrix size as the emission image. Another disadvantage is that the CT and emission images are acquired sequentially which allow for possible image misalignment which can lead to image artefacts.

In this study the use of a novel printed external radionuclide source as transmission source will be examined. Several types of systems with transmission hardware modifications and external sources have emerged for clinical implementation as discussed in Chapter 3.

Limitations of the radionuclide transmission systems discussed in Chapter 3 in Section 3.3.1 include: (i) regions of the body outside the field of view (FOV) leading to truncation artefacts, (ii) high source activity needed for collimated sources, (iii) complicated electronic equipment needed to separate transmission and emission images and (iv) insufficient counting statistics in the transmission image in an acceptably short imaging time.

This investigation proposes the use of an uncollimated flood transmission source. The flood source is obtained by printing a Tc-99m ink solution onto a sheet of paper using an inkjet printer as proposed by Van Staden *et al.* (2007). Printed radioactive sources were used by Larsson *et al.* (2000) in order to obtain scatter and attenuation free SPECT images. An evaluation of such a printed flood source was given in Chapter 4.

The potential advantages of a printed paper transmission source are firstly that the intensity distribution of the radioactive source can be modified to be suitable for a specific patient. This will result in a more uniform transmission image of the patient. An important advantage of this configuration is that the distribution of activity in the source system is tailored to the attenuation in the human body minimising the problem encountered when too few counts are recorded in some pixels of the transmission scan. A non-uniform radioactive distribution was printed on paper in Chapter 4 and used as transmission source for a cylindrical water phantom. An increased count rate was obtained in the central areas of the phantom. The second advantage of the printed radioactive source is that it can be manufactured at low cost to evaluate the use of different activity distributions in the transmission source as have been shown in Chapter 4. An optimal activity distribution can then be identified.

In this study Tc-99m will be used for the preliminary evaluation of a uniform transmission source; however, a long life radionuclide may be used once the required non-uniform configuration has been determined. This will however not be implemented as part of this study. The advantage of an uncollimated transmission source is that older existing gamma cameras can be easily modified to allow attachment of the printed transmission source,

since the source construction is light. Furthermore the photon-flux detected with an uncollimated transmission source is much higher than when collimation is used.

The disadvantages associated with the use of an uncollimated transmission source however include firstly the additional radiation dose to the patient compared to using a collimated source (Cao and Tsui, 1992). Secondly, in order to apply an appropriate attenuation correction it is important to calculate the attenuation coefficient values for narrow beam geometry. When using an uncollimated transmission source there may be added scattered events that will lead to broad beam attenuation coefficient values. The effect of the distance between the uncollimated transmission source and the detector on the amount of scatter being observed has not been investigated in literature. However a scatter correction can be applied to the transmission data as proposed by Kojima *et al*. (2004) if necessary. This will be investigated in Chapter 6.

This study hypothesizes that the scatter will decrease if the transmission source is placed further from the patient. By increasing the distance between the transmission source and the detector using a short phantom/patient detector distance, the source geometry will approach narrow beam geometry.

When an uncollimated flood source is used; photons reaching the patient from different angles will penetrate the patient and reach the collimator (photons (i) and (ii) in Figure 5.1.(a)). Photons reaching the detector at angles larger than the collimator resolution will be absorbed by the collimator and will not be detected. However, the photons that will be absorbed by the collimator if no interaction in the patient occurs can pass the collimator. They can be detected if they are scattered in the patient so that their direction is changed to be within the resolution angle of the collimator (Figure 5.1.(a) photons (i) and (ii); Figure 5.1.(b) photon (ii))). If the source patient distance is increased, the number of photons emerging from the source at angles larger than the collimator resolution, which can interact with the patient, will decrease (Figure 5.1.(a) and Figure 5.1.(b), photon (i)). Therefore by

increasing the source patient distance or decreasing the detector phantom/patient distance, the scatter contribution in the image is decreased.

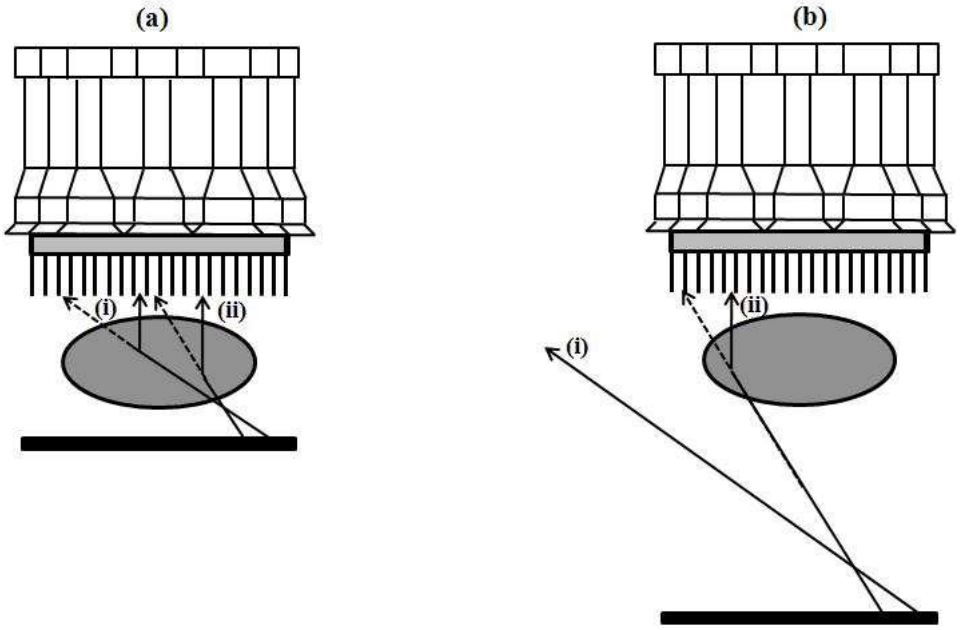

Figure 5.1*: Explanation of the hypothesis that the scatter will decrease if the transmission source is placed further from the patient. In (a) the transmission source is placed closer than in (b).*

In this study the planar performance characteristics of an uncollimated radioactive paper transmission source were evaluated by comparing its performance characteristics to that of a collimated radioactive paper transmission source. The hypothesis that the scatter will decrease if the uncollimated transmission source is placed further from the patient and the patient placed close to the detector was tested. The scatter contribution in the data obtained with the uncollimated transmission source was evaluated by reviewing the energy spectra obtained from the transmission data, the calculated attenuation coefficient values and the scatter percentages that was determined. This was done at different combinations of detector phantom distances, detector source distances and phantom source distances. The image resolution and detection efficiency were measured for the uncollimated transmission source images as well as for the collimated transmission source images. All

the evaluations were performed for planar studies only as the results will be directly applicable to SPECT. SPECT evaluation will be performed in Chapter 7.

5.2 Material and methods

Data was acquired using a GE Starcam 400AT (General Electric Medical Systems, Milwaukee) gamma camera fitted with a low energy all purpose (LEAP) collimator. The gamma camera was equipped with an Alfanuclear acquisition and processing station (Alfanuclear SAIYC, Buenos Aires). A collimator uniformity correction consisting out of 120 000 000 counts in a (128×128) image matrix was acquired using a water bath containing 555 MBq Tc-99m. All subsequent images were acquired with the LEAP collimator uniformity correction applied to the data. The LEAP collimator instead of the low energy high resolution collimator was selected for the preliminary evaluation due to the higher counting efficiency. A source holder equipped with a printed transmission source was supported on a bed parallel to the detector of the gamma camera, (Figure 5.2).

Figure 5.2*: A source holder equipped with a printed transmission source supported on the bed parallel to the detector fitted with a low energy all purpose collimator. The Perspex attenuation sheets are shown on the patient support.*

A uniform printed flood source was obtained as explained in Chapter 4 (Van Staden *et al.*, 2007). Approximately 370 MBq Tc-99m was deposited onto a paper sheet using an ink-jet

printer to produce the paper transmission source. These paper sources were laminated to prevent contamination. The IM512P acquisition software (Alfanuclear SAIYC, Buenos Aires) allows the acquisition of the energy spectrum for each pixel. Transmission data were acquired using an uncollimated as well as a collimated printed flood source. The latter incorporated a low energy high sensitivity (LEHS) collimator that was placed on top of the transmission source on the source holder. All measurements were repeated three times.

Scatter contribution in the uncollimated transmission data.

The performance of the transmission source was evaluated for different phantom and source positions in relation to the detector distance by obtaining three different data sets. In each data set one of the three distances (detector phantom distance, detector source distance or phantom source distance) was kept constant and the other two distances varied.

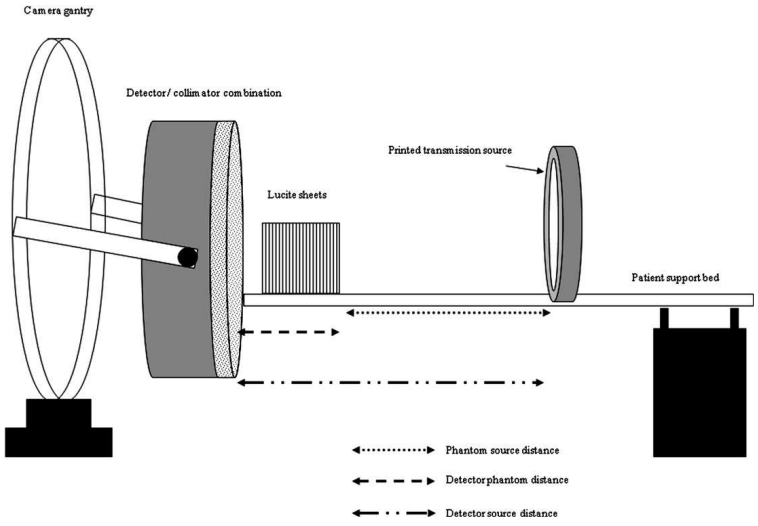

Figure 5.3: *A source holder equipped with a printed transmission source supported on the bed parallel to the detector fitted with a low energy all purpose collimator. The Perspex attenuation sheets are shown on the patient support table.*

For Data Set 1 the phantom was kept close to the detector and the source was moved in steps of 20 cm away from the detector. During the measurement of Data Set 2 the source was placed at a fixed distance of 80 cm from the detector and the phantom was moved in

steps of 20 cm away from the detector, closer to the source. For Data Set 3 the phantom and source were kept in contact with one another, thus the phantom source distance was kept at 0 cm. The detector phantom distance, as well as the detector source distance was increased in steps of 20 cm by moving the phantom and the source simultaneously. The different distance measurements for each data set are given in Table 5.1.

Table 5.1: *Distance measurements as obtained for each data set.*

Data Set	Description of Distance	Measurement Distances (cm)			
Data Set 1	Detector Phantom Distance	20	20	20	20
	Detector Source Distance	20	40	60	80
	Phantom Source Distance	0	20	40	60
Data Set 2	Detector Phantom Distance	20	40	60	80
	Detector Source Distance	80	80	80	80
	Phantom Source Distance	0	20	40	60
Data Set 3	Detector Phantom Distance	20	40	60	80
	Detector Source Distance	20	40	60	80
	Phantom Source Distance	0	0	0	0

5.2.1 Energy spectra

Energy spectra data for Tc-99m photons (140 keV) transmitted through various thicknesses (0 – 20 cm) of attenuating material were acquired for the different data sets mentioned in Table 5.1. In each instance a 2-dimentional energy spectrum data image was acquired in a 128 × 128 image matrix. Thus an energy spectrum was acquired in every pixel of the image. The energy spectrum data were acquired in 0.5 keV channels for 0 keV to 500 keV. Only information from 40 keV to 180 keV was considered. The attenuating material consisted of 19 Perspex plates each with a dimension of 20 × 20 cm^2 and a thickness of 1.07 cm. A single energy spectrum for each image was obtained representing

a region with size 9×9 cm^2 in the central area of the Perspex plates. The energy spectra of the different pixels in that region were summed in order to get good statistical information. The energy spectra for each data set were corrected for decay and acquisition time. Similar spectral data matrices were also obtained with the collimated transmission source for Data Set 1.

The difference between the spectra obtained from the uncollimated transmission source and the collimated transmission source was calculated for each energy channel for Data Sets 1, 2 and 3. Both spectra were obtained with the phantom (20 cm of Perspex plates) between the transmission source and the camera detector. The sum of the square of these differences (from 40 keV to 180 keV) was obtained in order to evaluate the contribution of scatter to the energy spectra. Similarly the sum of the square of the differences was obtained for the total counts in the 20% energy window region (126 – 154 keV) in order to evaluate the contribution of scatter in the 20% energy window. This information was obtained from the spectra acquired for all three data sets mentioned before.

5.2.2 Scatter percentage

The total counts in a 20% energy window were obtained from each acquired spectrum as mentioned in Section 5.2.1. The spectrum obtained with no attenuating medium was assumed to contain only primary counts ($P(0)$). The attenuated primary counts $P(d)$ at different thicknesses d were calculated using the narrow beam geometry attenuation coefficient value for Tc-99m through Perspex (μ) as determined with the collimated transmission source.

$$P(d) = P(0)\, exp(-\mu d) \tag{5.1}$$

The scattered counts $S(d)$ in the 20% energy window were obtained by subtracting the calculated primary counts $P(d)$ from the total observed counts $T(d)$.

$$S(d) = T(d) - P(d) \quad (5.2)$$

From Equations (5.1) and (5.2) the energy spectra of scattered photons for various Perspex thicknesses were calculated. The scattered counts were obtained by subtracting the calculated primary counts from the total observed counts. The scatter percentage in the 20% energy window was calculated as the ratio of scattered to total counts and expressed as a percentage for Data Sets 1, 2 and 3.

5.2.3 Attenuation coefficient

The spectra obtained as described in Section 5.2.1 were used to determine the attenuation coefficients for Perspex from the three data sets. The total counts in a 20% energy window were plotted against the thickness of Perspex for each spectrum obtained. An exponential function was fitted to the counts at increasing thicknesses and attenuation coefficient values calculated from these functions. An attenuation coefficient value was also obtained for the collimated transmission source with the setup as in Data Set 1. This latter value should correspond to the "narrow beam geometry" attenuation coefficient value.

5.2.4 Spatial resolution

The image resolution was evaluated by acquiring transmission images of a 2 mm thick lead strip as proposed by Cao and Tsui (1992). The lead strip was placed at depths of 1 cm, 10 cm and 18 cm in the Perspex phantom when measuring the resolution in the scatter medium. These distances correspond with the lead detector distance, since the phantom was placed against the detector (detector phantom distance = 20 cm). These measurements were repeated with the collimated transmission source with the lead strip at a lead detector distance of 10 cm. The phantom consisting of 20 cm Perspex plates was used as the scattering medium. From these images the derivative of the transmission edge response function was determined to calculate the full width at half maximum (FWHM) and the full width at tenth maximum (FWTM) for each configuration.

5.2.5 Detection efficiency

Images of the flood source were acquired with no scatter medium placed between the gamma camera and the source. Images were acquired in a 20% Tc-99m window at 5 cm, 10 cm, 15 cm, 20 cm, 25 cm and 30 cm distances from the gamma camera for 120 s with the collimated as well as the uncollimated source. The relative detection efficiency was calculated as the ratio of the counts obtained with the uncollimated source to counts obtained with the collimator.

5.2.6 Absorbed dose rate

An ionisation chamber was used to measure the entrance absorbed dose rate (*EAD* rate) from a printed collimated flood source containing 78 MBq Tc-99m. It was measured at detector source distances of 20 cm, 40 cm, 60 cm and 80 cm in front of a 20 cm Perspex phantom (Data Set 1). The measured dose rates were adjusted to a transmission source activity of 370 MBq suggested for clinical use with a collimated transmission source (Delpon *et al*., 2003). The *EAD* rate was then converted to a total *EAD* taking decay into account and assuming that the total acquisition time for a clinical planar study will be limited to 5 min. Furthermore, the total *EAD* for an acquisition period of 5 min with a collimated transmission source was measured to serve as a reference for comparing the doses without a source collimator and is indicate as EAD_{ref}.

5.3 Results

All results are given as an average of three repeated measurements. See Appendices A, B and C for the average and standard deviation values of the results.

5.3.1 Energy spectra

Figure 5.4 shows the average energy spectra obtained for the uncollimated transmission source through 20 cm of Perspex at different detector source distances (20 cm, 40 cm, 60 cm and 80 cm) and a fixed detector phantom distance of 20 cm (Data Set 1). The spectrum obtained for the collimated transmission source, 80 cm from the detector, attenuated through 20 cm of Perspex is also shown (C-80 cm). All the energy spectra for the three data sets were normalised to 100 at 150 keV in order to demonstrate the scatter component in the spectra.

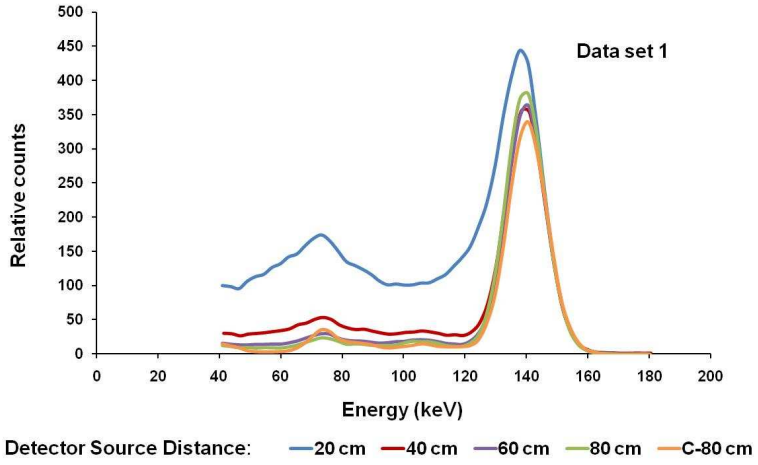

Figure 5.4: *Energy spectra (normalised to 100 at 150 keV) obtained with 20 cm of Perspex as attenuating medium. The spectra for Data Set 1 at different detector source distances of the uncollimated source as well as the spectrum obtained with the collimated source at a detector source distance of 80 cm (C-80 cm) are shown for the detector phantom distance fixed at 20 cm.*

It can be seen from Figure 5.4 that the scatter contribution in the spectra increases with decrease in detector source distance (also a decrease in phantom source distance) for the uncollimated transmission source. The spectra obtained with the detector source distances of 60 cm and larger compare well with the spectrum of the collimated source. The relative counts of the 60 cm and 80 cm spectra were however slightly higher than those of the C-80

cm spectrum. This can be explained due to the fact that small angle Compton scatter will contribute to the counts in the 20% energy window region (126 – 154 keV).

Figure 5.5 shows energy spectra obtained for the uncollimated transmission source through 20 cm of Perspex at a fixed detector source distance of 80 cm (Data Set 2) with different detector phantom distances (20 cm, 40 cm, 60 cm, 80 cm). The spectrum obtained for the collimated transmission source, 20cm from the detector, attenuated through 20 cm of Perspex is also shown (C-20 cm).

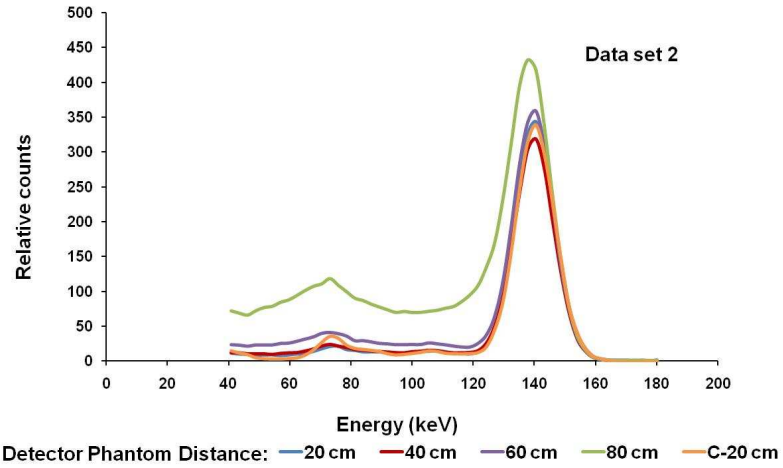

Figure 5.5: *Energy spectra (normalised to 100 at 150 keV) are shown for Data Set 2 at different detector phantom distances with the detector source distance fixed at 80 cm. The spectrum obtained from the collimated source at a distance of 80 cm and the detector phantom distance at 20 cm is also shown (C-20 cm).*

It can be seen from Figure 5.5 that the scatter contribution in the spectra increases with decrease in detector phantom distance or a decrease in phantom source distance for the uncollimated transmission source.

Figure 5.6 shows the average energy spectra obtained for the uncollimated transmission source through 20 cm of Perspex at different detector phantom distances (20 cm, 40 cm, 60 cm and 80 cm) and a fixed phantom source distance of 0 cm (Data Set 3). The spectrum obtained for the collimated transmission source, 80cm from the detector, attenuated through 20 cm of Perspex is also shown (C-20 cm).

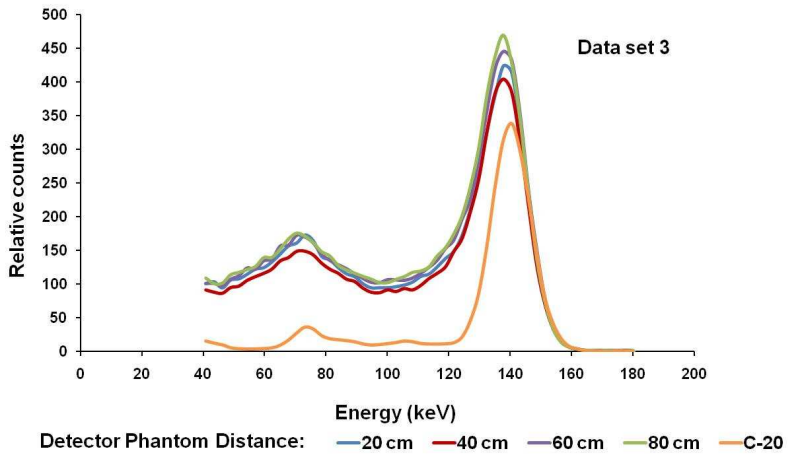

Figure 5.6: *Energy spectra (normalised to 100 at 150 keV) obtained with different detector phantom distances with the phantom source distance at 0 cm are shown here (Data Set 3). The spectrum obtained from the collimated source at a distance of 80 cm and the detector phantom distance at 20 cm is also shown (C-20 cm).*

It can be seen from Figure 5.6 that the scatter contributions in the spectra did not change with decrease in detector-source distance for the uncollimated transmission source. The scatter contribution in the spectra was significant in all cases. The phantom source distance was 0 cm at all instances.

The results in Figure 5.4 – 5.6 shows that the phantom source distances are the main determinant of the scatter component.

Figure 5.7 shows the sum of the square of the differences between the spectra (from 40 keV to 180 keV) obtained with the collimated and uncollimated transmission source at different detector source distances and a fixed detector phantom distance of 20 cm (Data Set 1). These differences are indicated by the dashed line, (------). Similarly the sum of the square of the differences were obtained for the channels in the 20% energy window (126 – 154 keV), indicated by the solid line, (——). The smallest differences were obtained at detector source distances larger than 60 cm indicating best correspondence with the collimated transmission source.

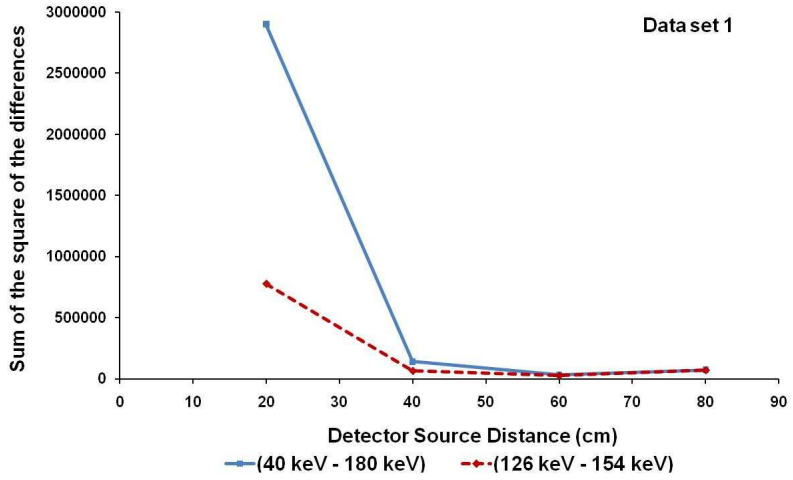

Figure 5.7: *Sum of the square of the differences between the spectra obtained with the collimated and uncollimated transmission source at different detector source distances.*

Figure 5.8 shows a similar graph for different detector phantom distances, for a detector source distance of 80 cm (Data Set 2).

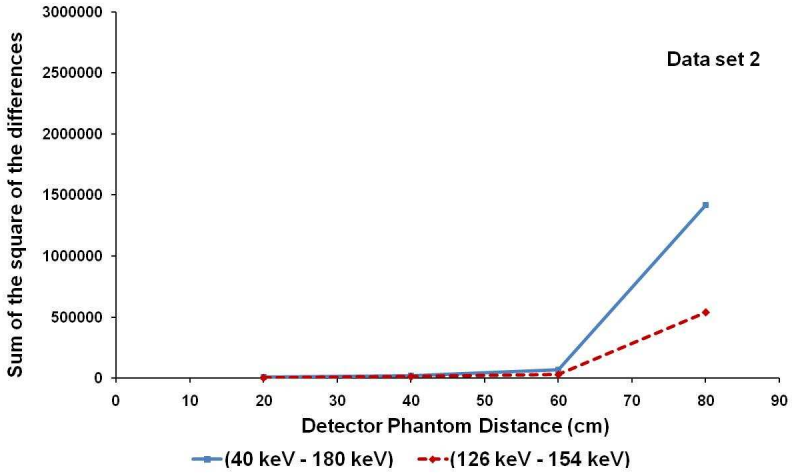

Figure 5.8: *Sum of the square of the differences between the spectra obtained with the collimated and uncollimated transmission source at different detector phantom distances.*

The largest difference was obtained at the detector phantom distance of 80 cm indicating a large scatter contribution; this corresponds to a phantom source distance of 60 cm.

5.3.2 Scatter percentage

Examples of measured energy spectra (normalised to 100 at 140 keV) at detector source distances of 20 cm for thicknesses of 3 cm and 18 cm of Perspex are shown in Figure 5.9.(a) and Figure 5.9.(b) respectively.

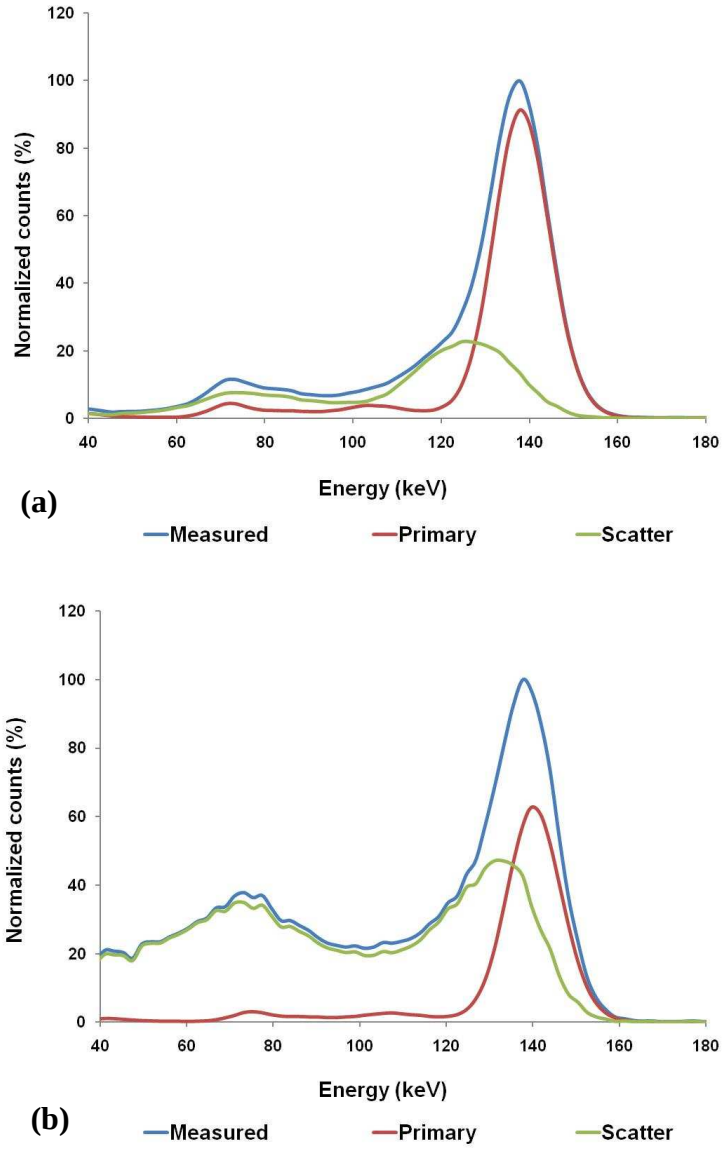

Figure 5.9: *Examples of measured energy spectra (**blue**) (normalised to 100 at 140 keV) with calculated primary (**red**) and scatter spectra (**green**) for (a) 3 cm and (b) 18 cm thicknesses of Perspex.*

Primary and scatter spectra calculated from the measured energy spectra (as explained in Section 5.2.2) show a scatter spectrum with the peak energy between 130 and 132 keV generated primarily from first order Compton scattered photons.

The scatter percentage in the 20% energy window was calculated for Data Set 1. The averages and standard deviations of the results for the three separate measurements for the uncollimated transmission source for various detector source distances (DSD) are shown in Appendix A, Table A1.

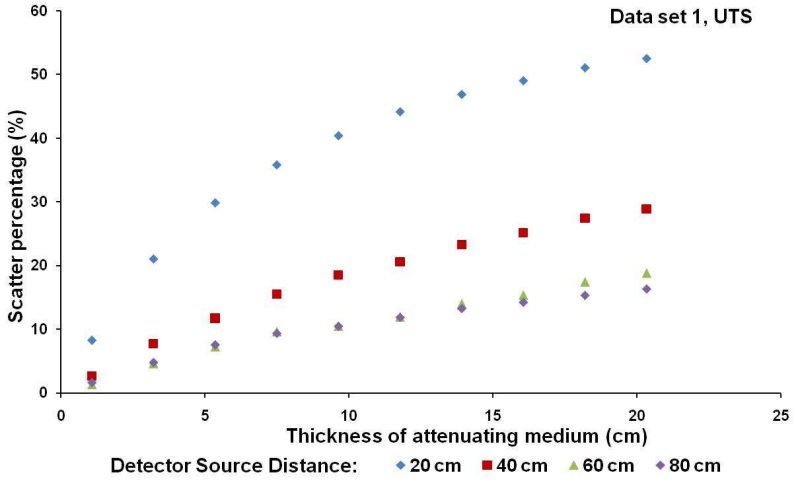

Figure 5.10: *Scatter percentage (%Sc) as a function of thickness of attenuating medium for Data Set 1. Values are given for various detector source distances for the uncollimated transmission source.*

Figure 5.10 shows the average results. It is clear that larger detector source distances result in a smaller scatter percentage in the uncollimated transmission image. For 0 cm detector phantom distance the uncollimated scatter percentage for ~20 cm Perspex is 52.4 ± 0.5% and 16.3 ± 0.3% for the 20 cm and 80 cm source detector distances.

The results for the three separate measurements for the Scatter Percentage (%Sc) in the 20% energy window for Data Set 2 for the uncollimated transmission source for thicknesses of Perspex (0 – 20 cm) are shown in Figure 5.11 and are tabulated in Appendix

A, Table A2. Figure 5.11 shows scatter percentages for the 80 cm detector source distance for ~20 cm Perspex. When imaging the transmission source at larger distances from the camera, the experimental setup approached narrow beam geometry as we hypothesized and explained in Figure 5.1.

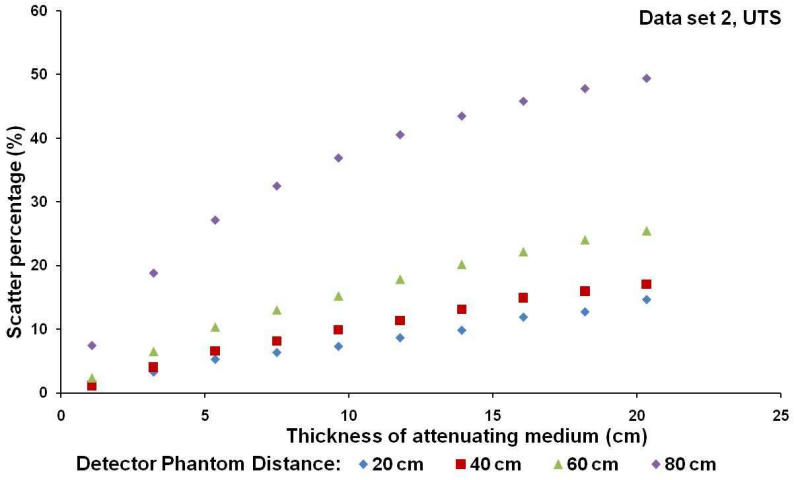

Figure 5.11: *Scatter percentage (%Sc) as a function of thickness of attenuating medium for Data Set 2. Values are given for various detector phantom distances for the uncollimated transmission source.*

Figure 5.11 shows larger detector phantom distances result in a smaller scatter percentage in the 20% energy window for the uncollimated transmission image. The uncollimated scatter percentages at 20 cm Perspex are 49.4 ± 3.1% % and 14.7 ± 0.9% % for the source at a fix distance of 80 cm from the detector and detector phantom distances of 20 cm and 80 cm respectively, (Data Set 2).

The results for the three separate measurements for the Scatter Percentage (%Sc) in the 20% energy window for Data Set 3 for the uncollimated transmission source for thicknesses of Perspex (0 – 20 cm) are shown in Figure 5.12 and are tabulated in Appendix A, Table A3.

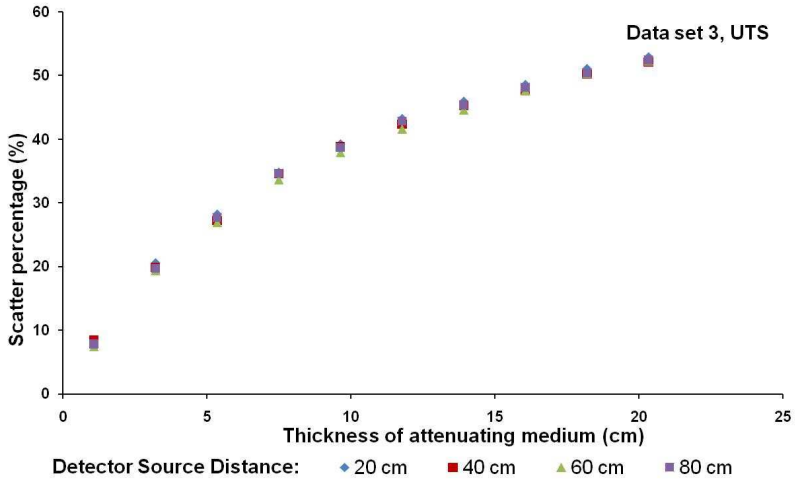

Figure 5.12: *Scatter percentage (%Sc) as a function of thickness of attenuating medium for Data Set 3. Values are given for various detector source distances for the uncollimated transmission source.*

Figure 5.12 shows the scatter contribution stays constant with increasing detector source distance, while keeping the phantom close to the source (phantom source distance 0 cm), (Data Set 3). For 0 cm phantom source distance the uncollimated scatter percentage for ~20 cm Perspex is 52.9% and 52.4% for the 20 cm and 80 cm detector source distances, (Data Set 3). Figure 5.11 and Figure 5.12 confirms the results obtained in Sections 5.3.1 that there is an increase in the scatter percentage in the 20% energy window with an increase in the detector phantom distance or a decrease in the phantom source distance.

The results for the three separate measurements for the Scatter Percentage (%Sc) in the 20% energy window for Data Set 1 for the collimated transmission source for thicknesses of Perspex (0 – 20 cm) are shown in Figure 5.13 and are tabulated in Appendix A, Table A4.

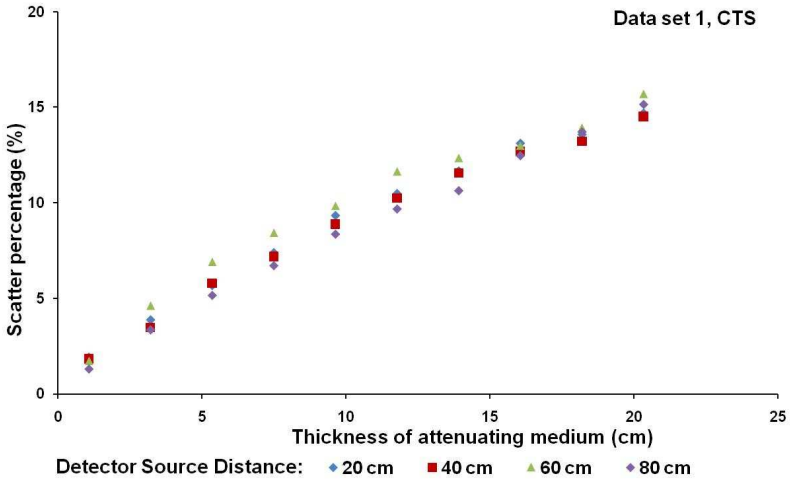

Figure 5.13: *Scatter percentage as a function of thickness of attenuating medium. Values are given for various detector source distances for the for the collimated transmission source.*

The results for the three separate measurements for the Scatter Percentage (%Sc) in the 20% energy window for Data Set 1 for the collimated transmission source for thicknesses of Perspex (0 – 20 cm) are shown in Figure 5.13 and are tabulated in Appendix A, Table A4. For 0 cm detector phantom distance the collimated scatter percentage for ~20 cm Perspex is 14.7 ± 1.0% and 15.2 ± 0.6% for the 20 cm and 80 cm source detector distances. Figure 5.13 confirms the results obtained in Sections 5.3.1 that there is no increase in the scatter percentage in the 20% energy window with an increase in the detector source distance or a decrease in the phantom source distance for a collimated transmission source.

5.3.3 Attenuation coefficient

The attenuation coefficient value increased with an increase in detector source distance for the uncollimated source in Data Set 1. The attenuation coefficient values changed from 0.141 ± 0.003 cm^{-1} to 0.168 ± 0.003 cm^{-1}, (Figure 5.12). The results for the three separate measurements for the attenuation coefficient values (cm^{-1}) as a function of detector source distances (DSD) for the uncollimated and collimated transmission source (UTS) for Data Sets 1 and 3 are shown in Appendix B, Table B1, Table B3 and Table B4. This is indicative of a decrease in scatter with an increase in the detector source distance. However the

"narrow beam geometry" attenuation coefficient value (0.170 ± 0.001 cm^{-1}), obtained from the collimated transmission data, is in good agreement to the published narrow beam attenuation coefficient (Brown *et al.*, 2008) of 0.167 cm^{-1}.

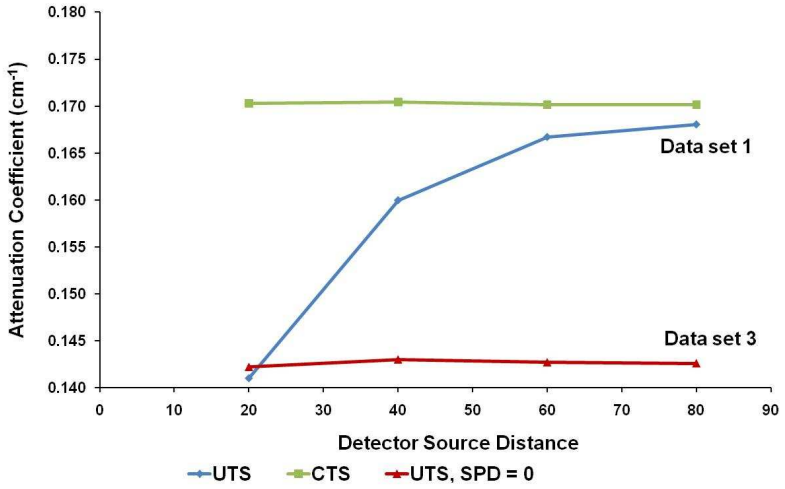

Figure 5.14: *Attenuation coefficient values (cm^{-1}) as a function of detector source distances for the uncollimated transmission source (UTS) for Data Sets 1 and 3. Results for the collimated transmission source (CTS) are also shown.*

The attenuation coefficient values determined for Data Set 3 is also shown in Figure 5.14. The phantom source distance was fixed at 0 cm. The average attenuation coefficient for the different detector source distances was 0.143 ± 0.001cm^{-1}. These values imply a large amount of scatter is present since the attenuation coefficient for Tc-99m through Perspex obtained with the LEHS collimator is 0.170 ± 0.001 cm^{-1}.

The average and standard deviations of the results for the three separate measurements for the attenuation coefficient values (cm^{-1}) as a function of detector source distances for the uncollimated and collimated transmission source for Data Set 2 are shown in Appendix B, Table B2 and Table B5. Figure 5.15 shows a decrease in the attenuation coefficient value with an increase in the detector phantom distance (0.171 – 0.144 cm^{-1}); indicating the influence of the increase in scatter contribution in Data Set 2.

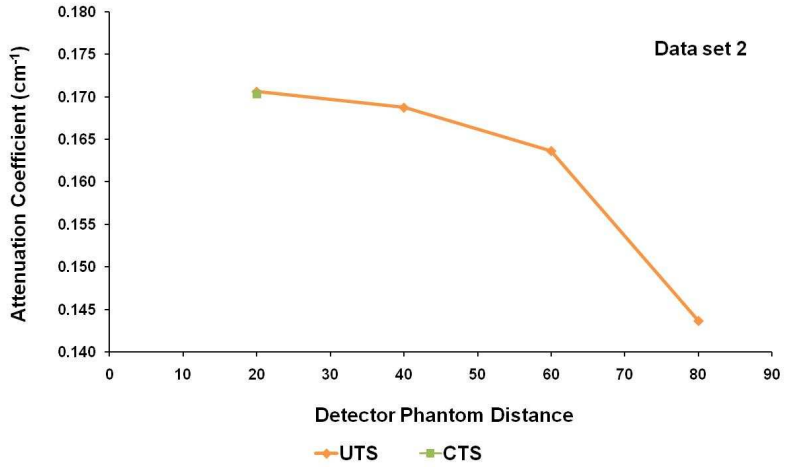

Figure 5.15: *Attenuation coefficient values (cm^{-1}) as a function of detector phantom distances for the uncollimated (UTS) as well as the collimated (CTS) transmission source for Data Set 2.*

These results confirm that scatter decreases with an increase in the detector phantom distance. For detector phantom distances of 60 cm and more, the attenuation coefficients for the collimated and uncollimated transmission sources were comparable (0.170 *vs.* 0.170).

5.3.4 Spatial resolution

The results for the spatial resolution expressed as FWHM obtained with the uncollimated as well as the collimated transmission source are shown in Figure 5.16.(a). The average and standard deviation results for three separate measurements for the spatial resolution with an uncollimated as well as collimated transmission source obtained for transmission images for different detector source distances with no scatter medium as well as with scatter medium placed between the detector and the transmission source are shown in Appendix C, Table C1 and Table C2. The FWHM values are shown for different detector source distances with no scatter medium as well as with scatter medium placed between the detector and the transmission source. The error bars on the graphs indicate twice the standard deviation of the three measurements obtained at each detector source distance.

No error bars are shown for the values obtained with the collimated transmission source since these measurements were not repeated.

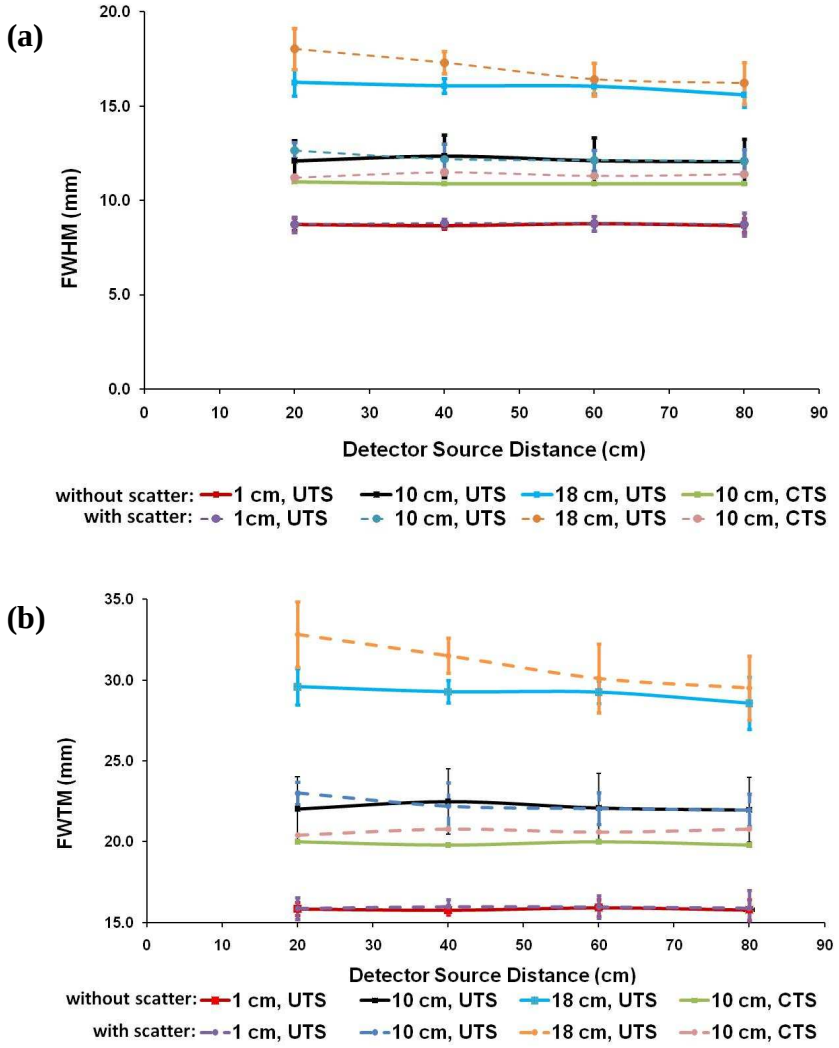

Figure 5.16: *Resolution results with an uncollimated (UTS) as well as a collimated transmission source (CTS) obtained for transmission images acquired using a 2 mm thick lead strip. (a) The FWHM and (b) FHTM values are shown for different detector source distances (DSD) with no scatter medium as well as with scatter medium placed between the detector and the transmission source. Error bars are displayed as twice the standard deviation of the three repeated measurements.*

At a lead edge detector distance of 1 cm there was no difference in the resolution values with an increase in detector source distance. The additional scatter medium had no

influence at this distance on the resolution values. At a lead detector position of 10 cm no difference was seen in the resolution values with an increase in detector source distance when no scatter medium was present and the uncollimated transmission source was used. The FWHM shows a minor deterioration at a detector source distance of 20 cm when scatter medium was added (12.6 mm vs. 12.1 mm when no scatter medium was added). The resolution values obtained with the uncollimated transmission source and a lead detector distance of 10 cm, at all source detector distances shows a slight increase in comparison to the values obtained with the collimated transmission source. This average difference obtained for the FWHM values was 1.2 mm without scatter medium. When scatter was added this average difference was 0.9 mm. FWTM values ranged from 15.9 mm to 29.3 mm when no scatter was present and from 16.1 mm to 31.1 mm with scatter present. The FWTM values (Figure 5.16.(b)) showed a similar trend to the FWHM values displayed in Figure 5.16.(a). These results correspond to similar findings obtained by Cao and Tsui (1992). However the influence of different detector source distances was not evaluated by Cao and Tsui (1992). At the lead position of 18 cm there was a significant difference between the resolution values with and without the scatter medium present. There was a marked decrease in the difference with an increase in the detector source distance. From the results mentioned it can be concluded that the resolution of the transmission images obtained with the uncollimated transmission source with scatter medium present, improved with an increase in the detector source distance. The resolution values obtained with the uncollimated transmission source were also comparable to the resolution values obtained with the collimated transmission source. This was caused by a marked decrease in the resolution values with an increase in the detector source distance, while the values without the scatter medium remained constant.

5.3.5 Detection efficiency

Figure 5.17 shows the detection efficiency for the uncollimated source as well as the collimated source. The collimated transmission source at a distance of 5 cm was used as the reference value.

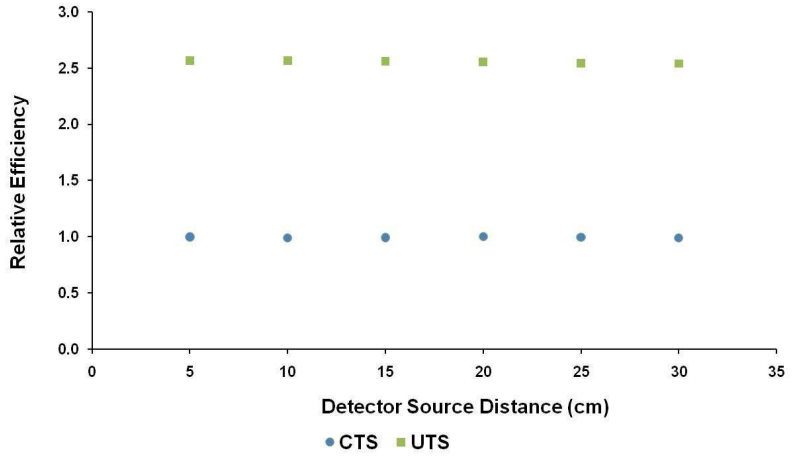

Figure 5.17: *Relative detection efficiency as a function of detector source distances for the uncollimated (UTS) as well as for the collimated transmission source (CTS).*

From Figure 5.17 it is evident that the detection efficiency for the uncollimated source was 2.5 times higher than for the collimated source. This will result in shorter transmission imaging times for the same image quality.

5.3.6 Absorbed dose rate

The entrance absorbed dose rate for the collimated source remained constant at all detector source distances (2.857 mGy/h), and this resulted in an EAD_{ref} of 0.237 mGy for a 370 MBq Tc-99m collimated source acquired for 5 min. Acquisition time was 5 min for the collimated and 2 min for the uncollimated transmission source.The EAD rate and sensitivity adjusted EAD (SEAD) for a 2 min acquisition time using the uncollimated source are given in Table 5.2.

Table 5.2: *Entrance absorbed dose (EAD) rate, sensitivity adjusted EAD (SEAD) and relative EAD (READ) for the uncollimated transmission source.*

DSD (cm)	*EAD* rate (μGy/h)	*SEAD* (μGy)	*READ* ($SEAD/EAD_{ref}$)
20	919.55	30.30	131.12
40	305.99	10.08	43.63
60	62.31	2.05	8.88
80	26.32	0.87	3.75

The dose rate from the uncollimated source at a detector source distance of 80 cm is only 3.75 times higher than that of the collimated transmission source.

5.4 Discussion

In this study, the hypothesis that the scatter will decrease if the uncollimated transmission source is placed further from the phantom and the phantom placed close to the detector was tested. The optimum detector source and detector phantom distances using a novel uncollimated radioactive paper transmission source were evaluated for application during planar transmission image acquisition. Results were compared to values obtained with a collimated transmission source. Although the evaluation was done for planar imaging it is also applicable to the projections acquired during SPECT data acquisition. The printed transmission source could easily be attached to an existing gamma camera since no additional heavy collimator or modification was required.

The results obtained from the acquired energy spectra with the collimated and uncollimated transmission source and the scatter percentage indicate that for the uncollimated transmission source and detector phantom distance of 20 cm, the scatter contribution increases with a decrease in detector source distances. The results suggest that the uncollimated transmission source would be most effective at distances of 60 cm and further from the detector in order to minimise the detection of scattered photons. The scatter can

be kept to a minimum if the phantom is close to the detector. When an uncollimated transmission source is used under different conditions, the scatter present would result in an underestimation of the attenuation and therefore an overestimation of activity quantification during emission imaging.

The presence of scatter also reduces image spatial resolution. By using the uncollimated source at detector source distances ≥ 60 cm and detector phantom distances ≥ 40 cm scatter is reduced and image quantification and spatial resolution should approach that obtained with the collimated transmission source. It was shown when the detector source and phantom source distances are increased to 60 cm and 40 cm respectively, the attenuation coefficient for the uncollimated transmission source increased to 0.168 ± 0.002 cm^{-1} in comparison to the value of 0.170 ± 0.001 cm^{-1} for the collimated transmission source. An increase in the detector source distance resulted in an improvement in the resolution values when measured in a scatter medium at the lead detector distances of 10 and 18 cm. Therefore, at detector source distances of 60 cm and larger the resolution using an uncollimated transmission source compares well with the resolution using a collimated transmission source. The FWHM difference is 0.9 mm. This is considered as acceptable for transmission imaging with the purpose of applying an attenuation correction to emission. The influence of the detector source distance on the resolution, as obtained with the uncollimated transmission source, was not studied by Cao and Tsui (1992).

It was shown that the detection efficiency of the uncollimated transmission source was nearly constant when the detector source distance (Data Set 1) was moved from 0 cm to 30 cm. The detection efficiency of the uncollimated transmission source was 2.5 times higher than that obtained with the collimated transmission source. Therefore, the uncollimated transmission source could acquire the same number of image counts 2.5 times faster than the collimated transmission source. The reduction in the transmission acquisition time will thus also reduce the absorbed entrance dose. The entrance absorbed dose resulting from using an uncollimated transmission source will be 3.75 times larger than obtained from a collimated source acquired for the same number of counts, but is still

acceptably low. The EAD for the uncollimated transmission source to acquire the same number of counts as with a collimated scan will be 0.877 mGy at a detector source distance of 80 cm. The published CT dose from SPECT/CT imaging is more than 4.6 mGy (Hamann *et al.*,2008) and can vary from 6 to 14 mSv (Buck *et al.*, 2008).

Potential advantages of a printed paper transmission source are firstly that the intensity distribution of the radioactive source can be modified to be suitable for a specific patient. This will result in a more uniform transmission image of the patient. An important advantage of the use of the printed paper transmission source configuration is that the distribution of activity in the source system is tailored to the attenuation in the human body, minimizing the problem encountered when too few counts are recorded in some pixels of the transmission scan (Celler *et al.*, 1998). Secondly the printed radioactive source can be manufactured at low cost to evaluate the use of different activity distributions in the transmission source. An optimal activity distribution can then be identified. In this study Tc-99m was used for the preliminary evaluation of a uniform transmission source; however, a long life radionuclide may be used once the required non-uniform configuration has been determined. Thirdly the advantage of an uncollimated transmission source is that older existing gamma cameras can be easily modified to allow for the attachment of the printed transmission source, since the source construction is light. Fourthly the photon-flux detected with an uncollimated transmission source is much higher than when collimation is used. The use of an uncollimated transmission source, due to the low cost, ease of implementation, the higher detection efficiency and low absorbed entrance radiation dose, is an appealing alternative source to be used during transmission imaging. The findings of this study for planar imaging should also apply to SPECT, since SPECT reconstruction uses planar acquired images as input data. Similar information is not available from previously published data.

5.5 References

Brown S, Bailey DL, Willowson K, Baldock C (2008). Investigation of the relationship between linear attenuation coefficients and CT Hounsfield units using radionuclides for SPECT. *Appl Radiat Isot;* **66:** pp1206–1212.

Buck AK, Nekolla S, Ziegler S, Beer A, Krause BJ, Herrmann K, Scheidhauer K, Wester HJ, Rummeny EJ, Schwaiger M, Drzezga A (2008). SPECT/CT. *J Nucl Med;* **49:** pp1305–1319.

Cao Z, Tsui BMW (1992). Performance characteristics of transmission imaging using a uniform sheet source with parallel-hole collimation. *Med Phys;* **19:** pp1205–1212.

Celler A, Sitek A, Stoub E,Hawman P, Harrop R, Lyster D (1998). Multiple line source array for SPECT transmission scans: simulation, phantom and patient studies. *J Nucl Med;* **39:** pp2183–2189.

Delpon G, Ferrer L, Lisbona A, Bardiès M (2003). Impact of scatter and attenuation corrections for iodine-131 two-dimensional quantitative imaging in patients. *Cancer Biother Radiopharmaceut;* **18:** pp191–199.

Fleming JS, Conway JH, Bolt L, Holgate ST (2003). A comparison of planar scintigraphy and SPECT measurement of total lung deposition of inhaled aerosol. *J Aerosol Med;* **16:** pp9–19.

Hamann M, Aldridge M, Dickson J, Endozo R, Lozhkin K, Hutton BF (2008). Evaluation of a low-dose/slow rotating SPECT-CT system. *Phys Med Biol*; **53:** pp2495–2508.

Kojima A, Matsumoto M, Tomiguchi S, Katsuda N, Yamashita Y, Motomura N (2004). Accurate scatter correction for transmission computed tomography using an uncollimated line array source. *Ann Nucl Med*; **18:** pp45–50.

Larsson SA, Jonsson C, Pagani M, Johansson L, Jacobsson H (2000). A novel phantom design for emission tomography enabling scatter- and attenuation-‘‘free’’ single-photon emission tomography imaging. *Eur J Nucl Med;* **27:** pp131–139.

Van Staden JA, du Raan H, Lötter MG, van Aswegen A, Herbst CP (2007). Production of radioactive quality assurance phantoms using a standard inkjet printer. *Phys Med Biol*; **52:** pp329–337.

Chapter 6

Evaluation of Scatter Corrected Transmission Images

6.1 Introduction

The use of an uncollimated flood source for transmission imaging was proposed in Chapter 5. The flood source was obtained by printing a Tc-99m ink solution onto a sheet of paper using an inkjet printer as proposed by Van Staden *et al*. (2007). When using an uncollimated transmission flood source, unwanted added scattered events in the acquired transmission data, may lead to broad beam attenuation coefficient values. These unwanted scattered events in the transmission data can be reduced by increasing the detector phantom distance (Van Staden *et al.*, 2010). Reducing the unwanted scatter photons from the transmission data by increasing the detector phantom distance is limited due to the design of the gantry systems of many Single Photon Emission Computed Tomography (SPECT) gamma cameras. Therefore the removal of unwanted scatter photons from the transmission data acquired with an uncollimated flood source by employing a scatter correction technique to the transmission data is a simple but practical method for obtaining "narrow beam geometry" attenuation coefficient values for SPECT gamma cameras (Kojima *et al.*, 2004**b**).

The aim of this part of the study was to evaluate the planar performance characteristics of an uncollimated printed transmission source after applying a scatter correction to the acquired data. The planar performance characteristics of the uncollimated scatter corrected transmission data were compared to the planar performance characteristics of the collimated transmission data. The application of two different scatter correction methods, the Triple Energy Window (TEW) and the Photon Energy Recovery (PER) scatter correction methods were compared as part of this study. All the evaluations were performed for planar studies only as the results will be directly applicable to SPECT. The measurement of tomographic transmission data will be performed in Chapter 7.

6.2 Material and methods

Data were acquired using a GE Starcam 400AT gamma camera fitted with a low energy all purpose (LEAP) collimator as discussed in Chapter 5, Section 5.2. All measurements were repeated three times.

6.3 Energy spectra

Energy spectra data for Tc-99m photons (140 keV) transmitted through various thicknesses (0 – 20 cm) of attenuating material were acquired at various detector source distances (20 cm, 40 cm, 60 cm and 80 cm) and at a detector phantom distance of 20 cm (Data Set 1). The acquisition of the energy spectra was discussed in Chapter 5, Section 5.2.

Data were obtained for the collimated transmission source at a detector source distances of 20 cm, 40 cm, 60 cm and 80 cm and at a detector phantom distance of 20 cm (similar to Data Set 1 in Chapter 5). The attenuating material consisted of 19 Perspex plate each with a dimension of 20×20 cm^2 and a thickness of 1.07 cm. A single energy spectrum for each image was obtained representing a region with size 10×10 cm^2 in the central area of the Perspex plates. Energy spectra similar to that in Chapter 5 were obtained. The energy spectra of the different pixels in that region were summed in order to get good statistical information. All the acquired spectra data were corrected for Tc-99m time decay.

The data acquisition mode enable the user to acquire energy spectra data that comprise out of ~ 0.5 keV energy channels from 0 keV to 500 keV. The summation of these energy channels allows the user the freedom to set any number of energy channels between 1 and 52 in the range of 126 – 154 keV as well as set these energy windows to the required energy window width.

6.4 Scatter percentage determination

6.4.1 Expected scatter percentage

The scatter percentage defined as the ratio of scattered counts to the total counts in the 20% energy window was calculated for different thicknesses of Perspex and expressed as a percentage as was discussed in Chapter 5, Section 5.2.4 and is referred to as the expected scatter percentage. The scatter contributions in the 20% energy window were also obtained by applying two scatter correction algorithms, the TEW and PER algorithms, to the acquired data. The scatter percentages calculated using these algorithms are referred to as the estimated scatter percentages.

6.4.2 Scatter percentage determination following TEW correction

An energy spectrum for each transmission image of different thicknesses of Perspex representing a region with size 10×10 cm^2 was obtained according to Section 6.3. This energy spectrum consisted of summed energy spectra of pixels in the 10×10 cm^2 region. The TEW scatter correction method was used to estimate the scatter contribution in the energy spectra. The estimate scatter contribution was compared with the expected scatter value (Section 6.3) to determine the accuracy of the scatter estimation with the TEW scatter correction method (Ogawa *et al.,* 1991). The TEW was discussed in Chapter 3, Section 3.5.2.1. For single-photon isotope studies the sub-energy window W_{right} to the right of the photo-peak can be ignored (Ichihara *et al.,* 1993). Thus, for the modified TEW scatter correction only two energy windows W_{left} and $W_{photopeak}$, centred on E_{left} = 121 keV and $E_{photo\text{-}peak}$ = 140 keV respectively were set for each summed energy spectrum, (Figure 6.1).

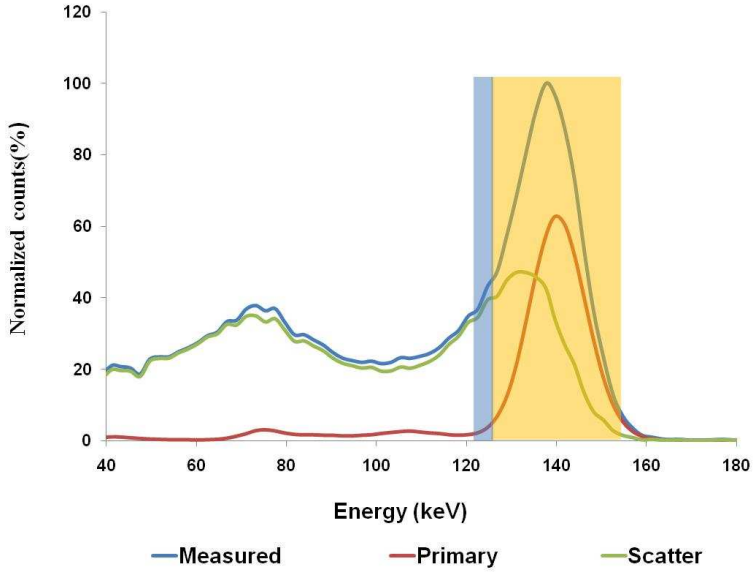

Figure 6.1: *Energy spectrum with the two energy windows W_{left} (**blue**) and $W_{photo\text{-}peak}$ (**yellow**).*

The TEW scatter correction estimates the number of scattered photons within the photo-peak window by using the number of counts acquired in the two energy windows W_{left} and $W_{photo\text{-}peak}$ as explained in Chapter 3, Section 3.5.2.1. The width (W) of the photo-peak and left sub-energy window was set to 20% (28 keV) and 7% (9 keV) respectively (Kojima *et al.*, 2004**a**). The scattered counts ($C_{scatter}$) were estimated according to Equation (6.1) where $C_{photo\text{-}peak}$ and C_{left} represent the counts in the photo-peak and left sub-energy window respectively.

$$C_{scatter} = K \times \left(\frac{C_{left}}{W_{left}} \right) \times W_{photo-peak} \qquad (6.1)$$

The subtraction factor K in Equation (6.1) was set to 0.5 as was initially proposed by Ogawa *et al.* (1991). The TEW scatter correction was also evaluated with K equals to 1.0 as suggested by Kojima *et al.* (2004**b**) for transmission imaging with an uncollimated flood source. The primary counts in the photo-peak window, $C_{primary}$ were estimated by using, Equation (6.2).

$$C_{primary} = C_{total} - C_{scatter} \tag{6.2}$$

with C_{total} the total number of counts in the photo-peak window (126 keV to 154 keV). The TEW estimated scatter percentage in the 20% energy window was calculated as the ratio of estimated scattered to total counts and expressed as a percentage as discussed in Section 6.4.1.

6.4.3 Scatter percentage determination following PER correction

Energy spectra for transmission data acquired with an uncollimated flood source for detector source distances of 20 cm, 40 cm, 60 cm and 80 cm for different thicknesses of Perspex were obtained as described in Section 6.3. Three different pre-selected sub-energy window settings namely (i) 52 windows of 0.5 keV, (ii) 9 windows of 3 keV and (iii) 3 windows of 11 keV for the photo-peak (126 keV to 154 keV) were selected.

The PER was used to estimate the scatter contribution in the energy spectra. The estimated scatter contribution was compared with the expected scatter value (Section 6.3) to determine the accuracy of the scatter estimation with the PER scatter correction method (Hannequin and Mas, 1998). The detected acquired transmission energy spectrum (*DES*) was assumed to be a combination of energy components and energy impulse response functions (*EIR*) as explained in Chapter 3, Section 3.5.2.2. From Equation (3.8) the *DES* was expressed as:

$$DES(E) = \sum_{e=l}^{h} a_e EIR_e(E) \tag{6.3}$$

where *l=116 keV* and *h=140 keV* were photo-peaks of the lowest and highest *EIRs* contributing to the photo-peak energy window; a_e was the *e-th* energy component and *E*, the sub-energy window width used to sample the energy spectrum, was allocated values of 0.5 keV, 3 keV and 11 keV. The reconstructed energy spectrum (*RES*) was calculated by using the Gaussian

distribution of the *EIR* of the GE Starcam 400AT gamma camera according to Equation (6.4).

$$ {}^{m}RES = \sum_{e=l}^{h} {}^{m}a_{e} EIR_{e} \qquad (6.4) $$

Only the *EIRs* from 116 to 140 keV that contribute significantly to the spectral acquisition window were included in the summation. The square of the difference between the *RES* and *DES* was used to determine the optimum solution for the equation.

From the solution of *RES* the estimated primary and scattered energy spectra could be determined. The PER estimated scatter percentage for a 20% energy window was calculated for different thicknesses of Perspex for detector source distances of 20 cm, 40 cm, 60 cm and 80 cm as the ratio of estimated scattered to total counts and expressed as a percentage as discussed in Section 6.4.1.

6.5 Attenuation coefficient determination

6.5.1 Attenuation coefficient

Attenuation coefficient values were determined as explained in Chapter 5, Section 5.2.3. Energy spectra obtained at various detector source distances ranging from 20 cm to 80 cm were used to determine the attenuation coefficient values for Perspex. The total counts in a 20% energy window were plotted against the thickness of Perspex for each acquired energy spectrum. An exponential function was fitted to the counts at increasing thicknesses. The values calculated from these exponential functions are the uncollimated attenuation coefficient values. Attenuation coefficient values were also obtained for the collimated transmission source at detector source distances of 20 cm, 40 cm, 60 cm and 80 cm. These values should correspond to the "narrow beam geometry" attenuation coefficient value for Tc-99m through Perspex which is 0.170 cm^{-1} and are referred to as the collimated attenuation coefficient values.

6.5.2 Attenuation coefficient determination following TEW correction

The TEW attenuation coefficient values were calculated from the estimated primary counts after subtracting the estimated scatter counts, obtained from the TEW scatter correction, from the total counts of each energy spectrum for various thicknesses (0 – 20 cm) of Perspex as explained in Section 6.5.1. These calculated values were determined at each detector source distance ranging from 20 cm to 80 cm and would be referred to as the TEW estimated attenuation coefficient values.

6.5.3 Attenuation coefficient determination following PER correction

The PER attenuation coefficient values were calculated from the estimated primary counts after subtracting the estimated scatter counts, obtained from the PER scatter correction, from the total counts of each energy spectrum for various thicknesses (0 – 20 cm) of Perspex as explained in Section 6.5.1. These calculated values were determined at each detector source distance ranging from 20 cm to 80 cm and would be referred to as the PER estimated attenuation coefficient values.

6.6 Results

The average results of three measurements are always reported unless stated differently. The average and standard deviation of the results of the three individual measurements are available in Appendix D, E, F and G.

6.7 Energy spectra

Figure 6.2 shows energy spectra acquired with an uncollimated flood source for thicknesses of 0 cm, 5 cm, 12 cm and 20 cm of Perspex for detector source distances of 20 cm and a

fixed detector phantom distance of 20 cm. These acquired energy spectra for the various thicknesses of Perspex were normalized to 100 at 140 keV.

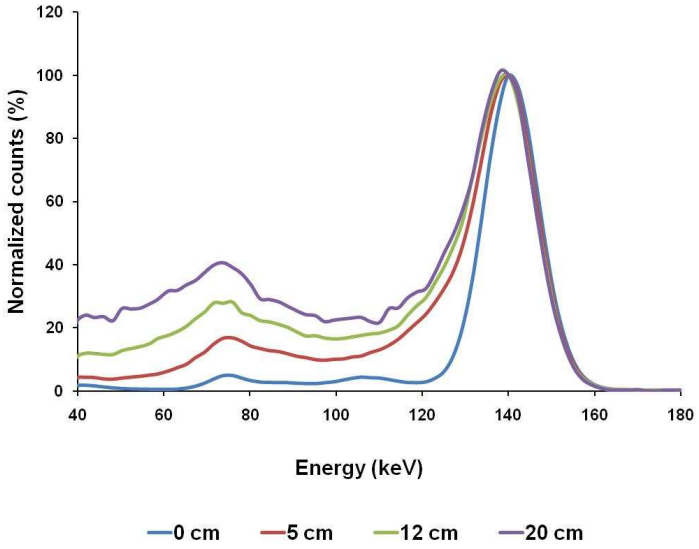

Figure 6.2: *Energy spectra normalized to 100 at 140 keV for Tc-99m photons transmitted through various thicknesses of Perspex at a detector source distance of 20 cm and detector phantom distance of 20 cm.*

From Figure 6.2 it is clear that for a detector source distance of 20 cm the scatter contribution increases with an increase in the thickness of the Perspex material from 0 cm to 20 cm.

Figure 6.3 shows the average energy spectra obtained for the uncollimated transmission source through 0 cm, 5 cm, 12 cm and 20 cm of Perspex at a detector source distance of 80 cm and a fixed detector phantom distance of 20 cm. Energy spectra were normalized to 100 at 140 keV. From Figure 6.3 it is clear that for a detector source distance of 80 cm the scatter contribution did not increase with an increase in the thickness of the Perspex material.

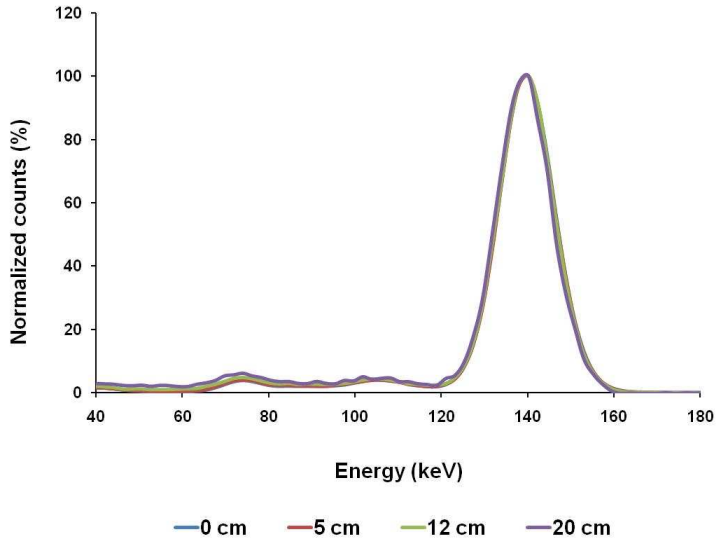

Figure 6.3: *Energy spectra normalized to 100 at 140 keV for Tc-99m photons transmitted through various thicknesses of Perspex at a detector source distance of 80 cm and detector phantom distance of 20 cm.*

Figure 6.4 shows the primary and expected scattered energy spectra calculated from the measured energy spectrum transmitted through 20 cm of Perspex at a detector source and a detector phantom distance of 20 cm.

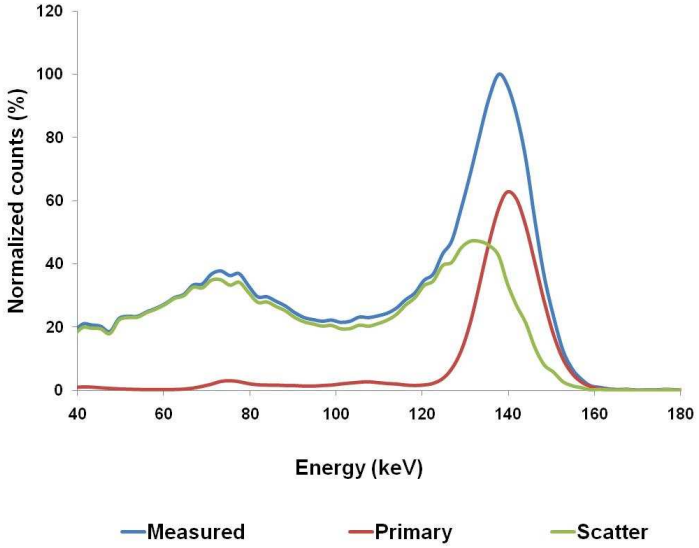

Figure 6.4: *Primary and scattered energy spectra obtained from the total energy spectrum transmitted through 20 cm of Perspex for a detector source and a detector phantom distance of 20 cm.*

The measured energy spectrum was normalized to 100 at 140 keV. It was also note from Figure 6.4 that the peak position of the measured energy spectrum acquired for 20 cm of Perspex shifted from 140 keV to 138 keV. This peak shift can be attributed to the numerous first order scatter events which were detected at 20 cm of Perspex at a detector source distance of 20 cm.

6.8 Scatter percentage determination

6.8.1 Expected scatter percentage

The expected scatter percentages obtained for energy spectra acquired using an uncollimated transmission flood source is shown in Figure 6.5. These are the same results as were shown in Chapter 5, Figure 5.10, Data Set 1, Appendix A, Table A1.

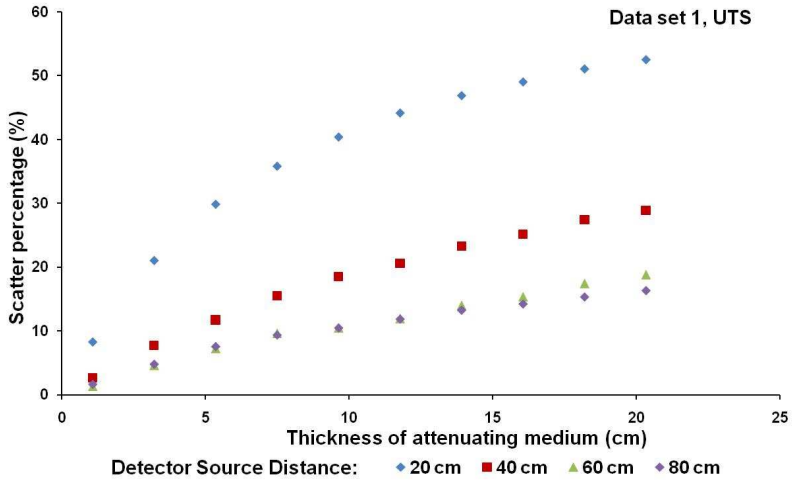

Figure 6.5: *Expected scatter percentage obtained for energy spectra acquired using an uncollimated transmission source (UTS). The values are given for detector source distances of 20 cm, 40 cm, 60 cm and 80 cm for Perspex of different thicknesses (0 - 20 cm) placed between the detector and the transmission source.*

The results were obtained for detector source distances ranging from 20 cm to 80 cm for different thicknesses of Perspex (0 – 20 cm). The Perspex plates were placed between the detector and the uncollimated transmission flood source. The data obtained show an

increase in the expected scatter percentage with an increase in the thickness of Perspex. It is also evident from Figure 6.5 that the expected scatter percentages increased as the detector source distances decreased. The expected scatter percentage was below 19% when the detector source distance was increased to 60 and 80cm. The maximum standard deviation obtained for the expected scatter percentage that was calculated for the three data sets that were repeated was 1.9% indicating a good reproducibility in the measurement. See Appendix A, Table A1.

6.8.2 Scatter percentage determination following TEW correction

Expected and estimated scatter percentages calculated with the TEW scatter correction are shown in Figure 6.6 and are tabulated in Appendix D, Table D1 and Table D2. The expected scatter percentages are the same as the results shown in Figure 6.5.

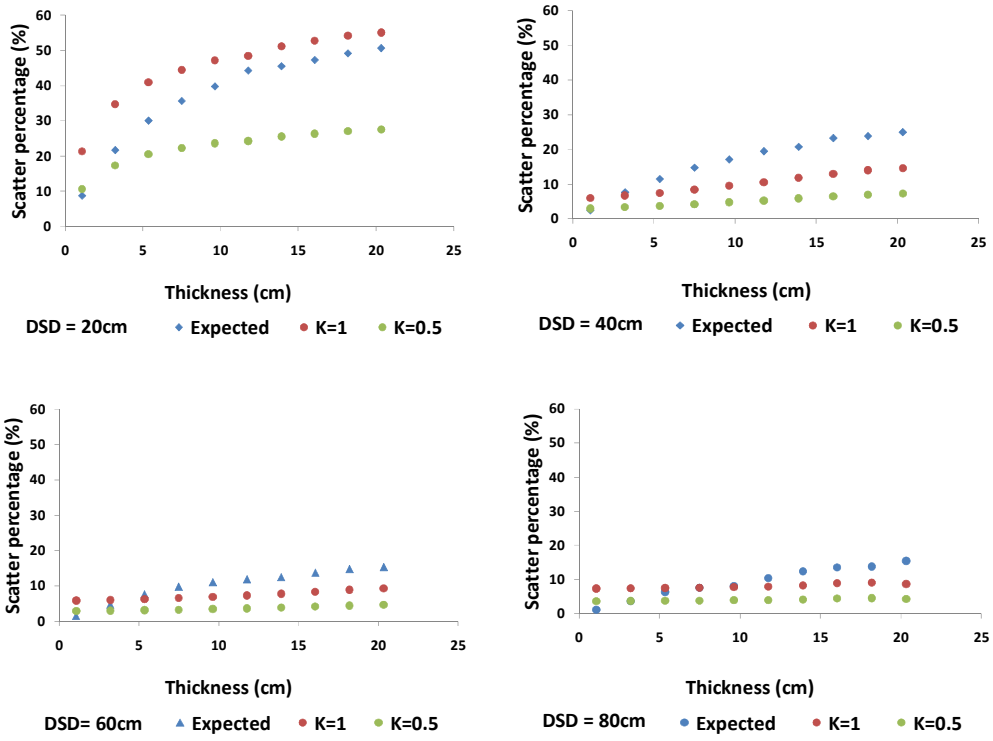

Figure 6.6: *Expected and TEW estimated scatter percentages calculated for correction factors K=0.5 and K= 1.0 for different thicknesses of Perspex for detector source distances (DSD) of 20 cm, 40 cm, 60 cm and 80 cm respectively.*

The TEW estimated scatter percentages were calculated for K=0.5 and K=1.0 for thicknesses of Perspex ranging from 0 cm to 20 cm for detector source distances of 20 cm, 40 cm, 60 cm and 80 cm respectively. For K=0.5 the largest absolute difference between the expected and TEW estimated scatter percentages were 23%, 17%, 13% and 9% for 20 cm, 40 cm, 60 cm and 80 cm of the Perspex respectively. The corresponding values for the differences between the expected and TEW estimated scatter percentages for K=1.0 were 13%, 10%, 8% and 5%. From the results it is clear that for all the detector source distances the absolute differences between the TEW estimated scattered percentages and the expected scattered percentages are smaller when K was set to 1.0. The small standard deviations (< 2.9) for the TEW estimated scatter percentage obtain from three separate measurements when K was set equal to 0.5 and 1.0 show that the both these techniques present reproducible scatter estimates for detector source distances of 20 cm, 40 cm, 60 cm and 80 cm, Appendix D, Table D1 and Table D2.

6.8.3 Scatter percentage determination following PER correction

Expected and estimated scatter percentages calculated with the PER scatter correction are shown in Figure 6.7 and are tabulated in Appendix E, Table E1, Table E2 and Table E32. The expected scatter percentages are the same as the results shown in Figure 6.5. The PER estimated scatter percentages were calculated for 52, 9 and 3 energy windows for varying thicknesses (1–20 cm) of Perspex for detector source distances of 20 cm, 40 cm, 60 cm and 80 cm respectively. When 52 and 9 sub-energy windows of width 0.5 keV and 3 keV each were selected over the photo-peak (126 – 154 keV) the largest absolute difference between the expected and estimated scatter percentages were 10%, 4%, 11% and 10% (using 52 windows) and 12%, 3.5%, 13%, and 10% (using 9 windows) for detector source distances of 20 cm, 40 cm, 60 cm and 80 cm respectively. When only 3 sub-energy windows of width 11 keV each was selected over the photo-peak the largest difference between the expected and estimated scatter percentages were 20%, 7%, 9%, 5% for detector source distances of 20 cm, 40 cm, 60 cm and 80 cm.

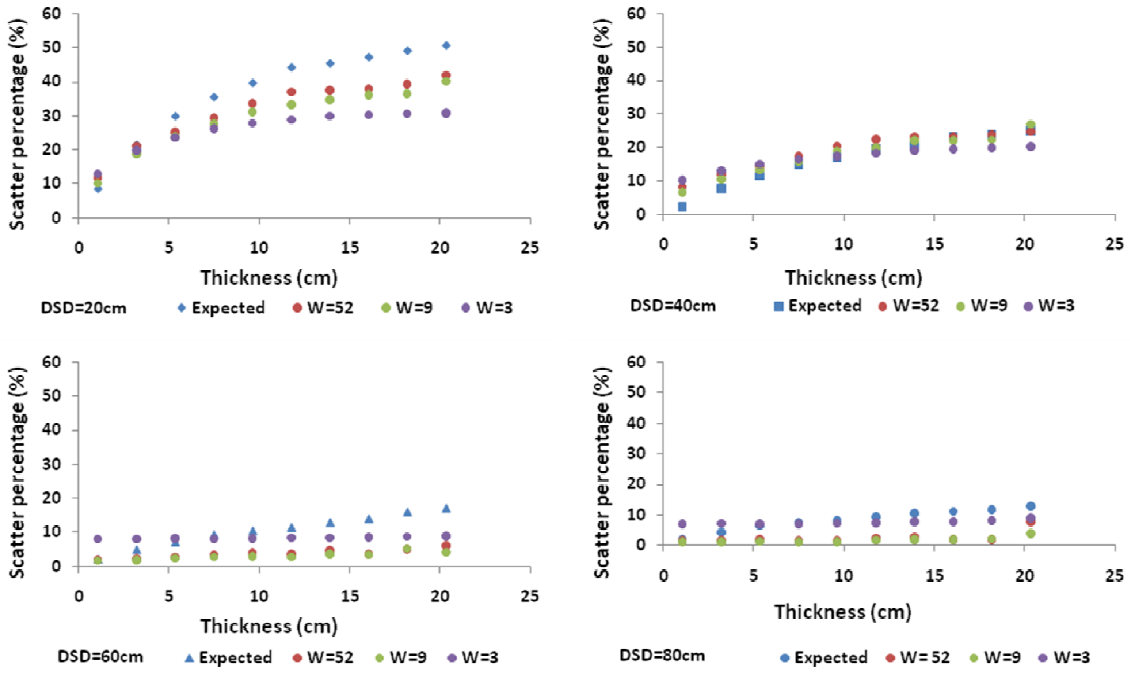

Figure 6.7: *Expected and PER estimated scatter percentages using 52, 9 and 3 energy windows (W) respectively. These scatter percentages obtained for different thicknesses of Perspex (0 – 20 cm) are shown for detector source distances (DSD) of 20 cm, 40 cm, 60 cm and 80 cm respectively.*

The large standard deviations (< 15.0) obtained for the PER estimated scatter percentage from the three separate measurements show a large variance in the technique when 52, 9 and 3 pre-selected sub-energy windows were selected Appendix E, Table E1, Table E2 and Table E3. This large variance in the PER technique indicate that the technique is more unstable than the TEW technique.

6.9 Attenuation coefficient determination

6.9.1 Attenuation coefficient

The attenuation coefficient values were calculated from the average of three separate measurements. The attenuation coefficient values obtained for detector source distances of

20 cm, 40 cm, 60 cm and 80 cm for different thicknesses (0 – 20 cm) of Perspex placed between the detector and the uncollimated transmission source are shown in Figure 6.8.

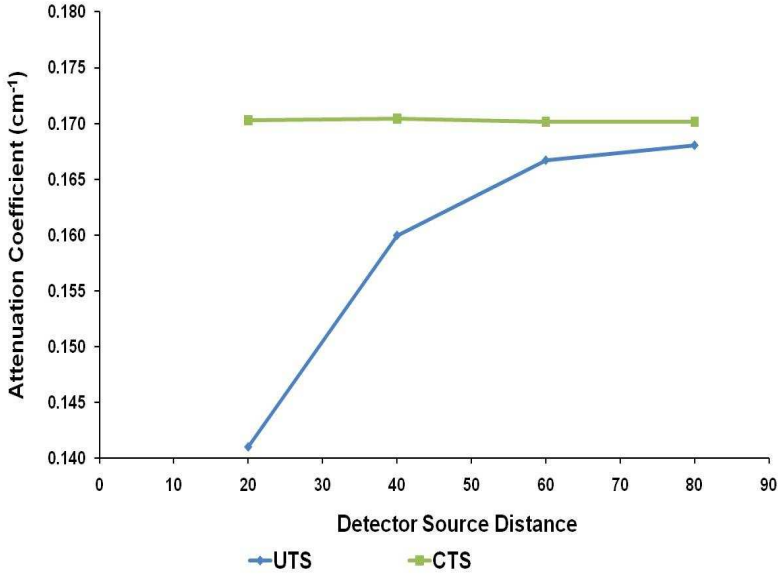

Figure 6.8: *Uncollimated, uncorrected (UTS) and collimated transmission source (CTS) attenuation coefficient values (μ) for energy spectra acquired using an uncollimated as well as a collimated transmission source. The values are given for different detector source distances with Perspex placed between the detector and the transmission sources.*

Results obtained with the collimated transmission source are also shown in Figure 6.8. The results for the three separate measurements for the attenuation coefficient values (cm^{-1}) for the uncollimated and collimated transmission source for Data Sets 1 are shown in Appendix B, Table B1 and Table B4. From Figure 6.8 it is evident that the attenuation coefficient values for the uncollimated transmission source increase with an increase in the detector source distance. For the collimated transmission source the attenuation coefficient values are constant and are independent of the source detector distance. The dependency of the attenuation coefficient values from the detector source distance can be attributed to the scatter contribution which decreases as the source detector distance of the uncollimated transmission source increases as was discussed in Section 6.3.2.1.

6.9.2 Attenuation coefficient determination following TEW correction

Figure 6.9 shows the TEW (K=0.5 and K=1.0) estimated attenuation coefficient values (μ) obtained for the uncollimated transmission source through 20 cm of Perspex at different detector source distances (20 cm, 40 cm, 60 cm and 80 cm) and a fixed detector phantom distance of 20 cm (data set 1). Results for data set 1 obtained with the collimated transmission source are also shown in Figure 6.9.

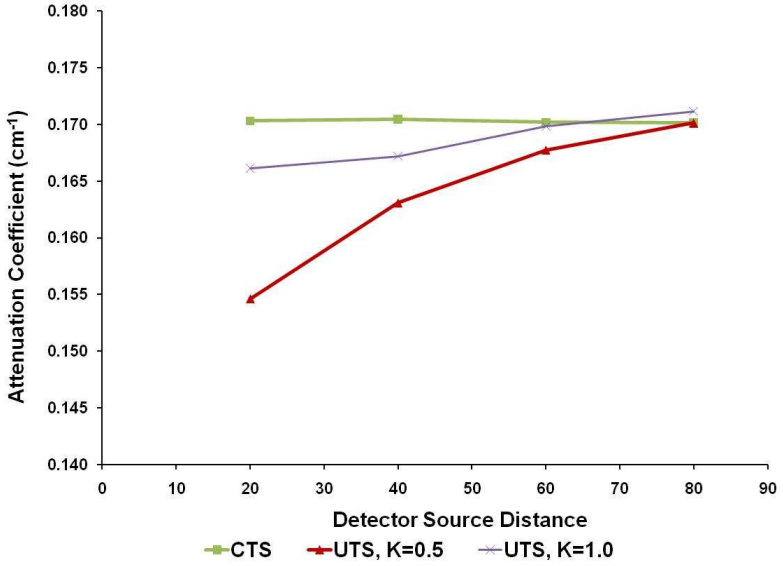

Figure 6.9: *Collimated transmission source (CTS) and TEW estimated attenuation coefficient values (μ) for energy spectra acquired using a collimated as well as an uncollimated transmission source. The values are given for different detector source distances with Perspex placed between the detector and the transmission source.*

The results for the average for the three separate measurements for the TEW estimated attenuation coefficient values (cm^{-1}) calculated for the correction factors K=0.5 and K=1.0 for the uncollimated (UTS) as well as the collimated transmission source for data sets 1 are shown in Appendix F, Table F1 and Table F2 and Appendix B, Table B1 respectively. From Figure 6.9 it is evident that the TEW estimated attenuation coefficient values (K = 0.5) underestimate the collimated attenuation coefficient values (0.170 ± 0.001 cm^{-1}) at detector source distances of 20 cm (0.155 ± 0.002 cm^{-1}), 40 cm (0.163 ± 0.003 cm^{-1}) and 60 cm (0.168 ± 0.002 cm^{-1}). It can be seen from Figure 6.9 that this underestimation of the

collimated attenuation coefficient value was absent at a detector source distance of 80 cm (0.170 ± 0.004 cm^{-1}).

From Figure 6.9 it can be seen that the TEW attenuation coefficient values (K = 1.0) obtained at detector source distances of 20 cm (0.166 ± 0.001 cm^{-1}) and 40 cm (0.167 ± 0.001 cm^{-1}) underestimate the collimated attenuation coefficient values. This underestimation of the collimated attenuation coefficient value was absent at detector source distances of 60 cm (0.170 ± 0.001 cm^{-1}) and 80 cm (0.171 ± 0.001 cm^{-1}).

These results confirm what was reported by Kojima *et al*. (2004**b**) that transmission imaging with an uncollimated transmission source provides accurate attenuation coefficient values when the TEW scatter correction method was used with a subtraction factor K equal to 1.0.

6.9.3 Attenuation coefficient determination following PER correction

Figure 6.10 shows the PER estimated attenuation coefficient values (μ) obtained after applying the PER scatter correction for 52, 9 and 3 sub-energy energy windows to the acquired uncollimated transmission data. These attenuation coefficient values were obtained for detector source distances of 20 cm, 40 cm, 60 cm and 80 cm respectively. Results for the collimated transmission source are also shown in Figure 6.10. The results for the three separate measurements for the PER estimated attenuation coefficient values (cm^{-1}) calculated for 52, 9 and 3 pre-selected sub-energy windows for the uncollimated (UTS) as well as the collimated transmission source for Data Sets 1 are shown in Appendix G, Table G1, Table G2 and Table G3 and Appendix B, Table B1 respectively. The attenuation coefficient values were calculated from the average of 3 separate measurements.

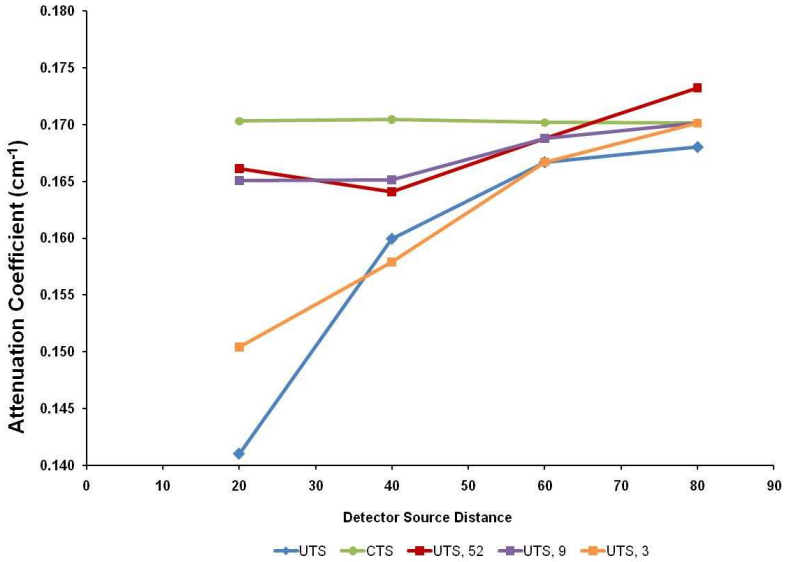

Figure 6.10: *Collimated (CTS) and PER estimated attenuation coefficient values (μ) obtained for energy spectra acquired using a collimated as well as an uncollimated transmission source. PER results are given for selecting 52, 9 and 3 windows respectively The values are given for different detector source distances with Perspex placed between the detector and the transmission source.*

From Figure 6.10 it is clear that the PER estimated attenuation coefficient values (W = 3) underestimate the collimated attenuation coefficient values (0.170 ± 0.001 cm^{-1}) at detector source distances of 20 cm (0.150 ± 0.003 cm^{-1}), 40 cm (0.158 ± 0.005 cm^{-1}) and 60 cm (0.167 ± 0.003 cm^{-1}). At a detector source distance of 80 cm (0.170 ± 0.004 cm^{-1}) the underestimation of the collimated attenuation coefficient value by the PER estimated attenuation coefficient value was absent, (Figure 6.10).

It can be seen from Figure 6.10 that the PER estimated attenuation coefficient values (W = 9) underestimate the collimated attenuation coefficient values at detector source distances of 20 cm (0.165 ± 0.004 cm^{-1}), 40 cm (0.165 ± 0.003 cm^{-1}) and 60 cm (0.169 ± 0.004 cm^{-1}). At a detector source distance of 80 cm (0.170 ± 0.005 cm^{-1}) the PER estimated attenuation coefficient value was in good agreement with the collimated attenuation coefficient value.

The PER estimated attenuation coefficient values obtained for 52 pre-selected sub-energy windows at detector source distances of 20 cm, 40 cm and 60 cm were 0.166 ± 0.004 cm^{-1},

0.164 ± 0.003 cm^{-1} and 0.169 ± 0.004 cm^{-1} respectively, (Figure 6.10). At a detector source distance of 80 cm the PER estimated attenuation coefficient value (0.173 ± 0.008 cm^{-1}) overestimated the collimated attenuation coefficient.

6.10 Discussion

In this study the possibility of using an uncollimated flood source along with an appropriate scatter correction technique for planar transmission imaging was evaluated.

A number of studies have shown that transmission computed imaging could be done successfully with uncollimated flood or sheet sources (Malko *et al.,* 1986; Bailey, 1987). The advantage of this configuration is that the flood source fully irradiates the detector and requires no source motion. Uncollimated flood or sheet sources have the disadvantage that a high number of scattered photons are acquired in the transmission data due to the broad-beam imaging conditions. The attenuation coefficient values obtained from the uncollimated flood source would be lower than the values calculated from a collimated flood source. This limitation can be overcome by collimating the transmission source to produce a geometry that more accurately represents narrow beam geometry (Cao and Tsui, 1992). By using a collimated flood source the advantage of a higher photon flux along with little or no modifications to the gantry of the gamma camera would be lost. For this reason a number of studies have been done to try and solve the problem of using an uncollimated flood source for transmission imaging (Kojima *et al.,* 2004**b**; Malko *et al.,* 1986; Bailey, 1987; Cao and Tsui, 1992).

In a study done by Van Staden *et al.* (2010) it was shown that for an uncollimated transmission source at a distance of 60 cm from the gamma camera detector and 40 cm from a phantom (~20 cm in diameter) the scatter contribution to the acquired transmission image was negligible. Unfortunately for transmission computed tomography these acquisition parameters are not always feasible due to limitations in the design of gamma cameras. Therefore instead of increasing the detector source distance, a scatter correction

could be used to remove unwanted scattered photons from the transmission images acquired with an uncollimated flood source (Kojima *et al.,* 2004**b**). Two scatter correction techniques, the TEW and PER, were used in this study to evaluate the accuracy of scatter estimations as well as the attenuation coefficient values after applying these scatter corrections to the acquired transmission data. Kojima *et al.* (2004**b**) successfully employed the TEW scatter correction technique to remove unwanted scattered photons from the transmission images which were acquired with an uncollimated transmission line source array. Unwanted scatter photons were removed successfully from the acquired transmission images by employing a subtraction factor K equal to 1.0 instead of the usual 0.5 as proposed by Ogawa *et al.* (1991). No clear explanation was provided by Kojima *et al.* (2004**b**) for the more accurate scatter estimation that was obtained when the subtraction factor K equal to 1.0 instead of 0.5 was used. Another limitation of the study done by Kojima *et al.* (2004**b**) was that all the measurements were done at a fix detector source distance as well as at a fix source phantom distance.

In this study we have used an uncollimated printed flood source along with the TEW and PER scatter correction techniques to conduct transmission imaging at detector source distances which ranges from 20 cm to 80 cm. The accuracy of the two scatter correction techniques were evaluated by comparing the expected and estimated scatter percentages as well as the expected and estimated attenuation coefficients after applying the scatter corrections to the acquired transmission data. The expected scatter and attenuation coefficient values were calculated by using an attenuation coefficient value obtained from a collimated transmission flood source.

From Figure 6.2 it is clear that the uncollimated printed source causes a large number of scattered photons in the transmission images at a detector source distance of 20 cm. The ratio of the scatter photons to the primary photons increased as the thickness of the Perspex increased from 0 cm to 20 cm of Perspex and this increase in the ratio of the scattered to the primary photons could give inaccurate attenuation coefficient values. This increase in scatter with increase in the thickness of the attenuating medium was absent at a fix source

detector distance of 80 cm as shown in Figure 6.3. A scatter energy peak between 134 keV and 136 keV within the photo-peak of Tc-99m was formed at a detector source distance of 20 cm. At a detector source distance of 20 cm the photo-peak position shifted from 140 keV to 138 keV due to the large number of small angle scattered events that were generated as the 140 keV photons pass through the Perspex. A large number of these small angle scattered photons have passed through the LEAP collimator and were accepted within the photo-peak window.

From Figure 6.5 it is clear that the expected scatter percentages have increased as the detector source distances decreased for thicknesses ranging from 0 cm to 20 cm of Perspex. From these results it is evident that a scatter correction is needed to correct for unwanted scattered photons that were included in the acquired transmission images.

The largest absolute difference between the expected and TEW estimated scatter percentage (23%) was observed when the subtraction factor K was set to 0.5 at a detector source distance of 20 cm for 20 cm of Perspex. By setting the subtraction factor K equal to 1.0 the corresponding difference between the expected and the TEW estimated scatter percentage at a detector source distance of 20 cm was 13% for 20 cm of Perspex. This smaller absolute difference between the expected and the TEW estimated scatter percentage when the subtraction factor K was raised from (K = 0.5) to (K = 1.0) is in accordance with what Kojima *et al*. (2004**b**) reported when they used an uncollimated line array source along with the TEW scatter correction. From the previous results it is evident that for transmission imaging with an uncollimated flood source at a detector source distance of 20 cm the TEW scatter correction (K = 0.5) underestimate the number of scatter photons which were included in the transmission image. This underestimation of the number of scatter photons by the TEW scatter correction technique can be contributed to the large number of small angle scattered photons which were generated and accepted within the photo-peak window at a detector source distance of 20 cm. We found that the conventional TEW scatter correction technique with K = 0.5 was not sufficient to compensate for unwanted scatter photons included in transmission data using the

uncollimated printed flood source and proposed the use of a subtraction factor K = 1.0 for transmission imaging.

For the PER scatter correction technique at detector source distances of 20 cm, 40 cm and 60 cm there were no significant differences between the expected scatter percentage and the PER estimated scatter percentage values calculated with 52 and 9 pre-selected sub-energy windows. At detector source distances of 20 cm and 40 cm, where large numbers of scatter photons were present in the acquired transmission images, the PER estimated scatter percentages with 52 and 9 pre-selected sub-energy windows compared favourable to the expected scatter percentage values. When only 3 pre-selected sub-energy windows were selected the PER estimated scatter percentage underestimated the measured expected scatter percentage with 20% at a detector source distance of 20 cm. This large underestimation between the expected and TEW estimated scatter percentage at a detector source distance of 20 cm can be contributed to the instability of the PER scatter technique when only 3 energy windows were selected over the photo-peak window.

From the results in this study it is evident that when a subtraction factor K = 0.5 was selected the TEW scatter correction underestimated the scatter contribution in the transmission images acquired with an uncollimated flood source. This underestimation of the amount of scatter in the acquired transmission images at detector source distances of 20 cm and 40 cm has provided estimated attenuation coefficient values of (μ = 0.155 cm^{-1}, μ = 0.163 cm^{-1}) which were lower than the attenuation coefficient value (μ = 0.170 cm^{-1}) as determined with a collimated flood source as described in Chapter 5. At detector source distances of 60 cm and 80 cm the underestimation of the collimated attenuation coefficient value by the estimated attenuation coefficient values were absent due to the small amounts of scatter photons which were present and corrected for by the TEW scatter correction technique. By applying the TEW scatter correction method with a subtraction factor K=1.0 the accuracy of the attenuation coefficient values obtained from the acquired transmission images showed an improvement from 0.155 cm^{-1} to 0.166 cm^{-1} and 0.163 cm^{-1} to 0.167 cm^{-1} for detector source distances of 20 cm and 40 cm respectively. These

attenuation coefficient values compare favourably with the value for Tc-99m through Perspex (μ =of 0.170 cm^{-1}) which was calculated for the collimated transmission flood source. At a detector source distance of 60 cm the underestimation of the estimated attenuation coefficient value was absent.

PER attenuation coefficient values calculated from the primary energy spectra at detector source distances of 20 cm and 40 cm with 9 and 52 pre-selected sub-energy windows were slightly lower than the value for Tc-99m through Perspex (μ =of 0.170 cm^{-1}) which was calculated for the collimated transmission flood source. For 3 pre-selected sub-energy windows the PER attenuation coefficient value obtained at 20 cm detector source distance was lower than the value for Tc-99m through Perspex (μ =of 0.170 cm^{-1}) obtained for the collimated flood source. At detector source distances of 60 cm and 80 cm the PER attenuation coefficient values obtain with 52, 9, and 3 pre-selected sub-energy windows were in good agreement with the values obtained for the collimated flood source.

This study showed that scattered photons can successfully be removed from transmission images acquired with an uncollimated printed flood source by applying an appropriate scatter correction technique to the acquired data. The adjustment which was made to the subtraction factor from K = 0.5 to K = 1.0 for the TEW scatter correction technique has led to an improvement in the estimated scatter percentage and TEW attenuation coefficients values obtained after applying the TEW scatter correction to the acquired transmission images. From the results of the PER scatter correction technique it was evident that when only 3 pre-selected sub-energy windows was used over the photo-peak for scatter estimation an underestimation of the collimated attenuation coefficient value was obtained. Although 9 pre-selected sub-energy windows over the photo-peak has provided a more acceptable estimation of the scatter percentage and PER attenuation coefficient values, hardware and software limitation to the acquisition and processing workstations of old gamma cameras as well as poor counts statistics can hamper the successful implementation of the PER scatter correction technique on these workstations.

In the next chapter the modified TEW scatter correction with a subtraction factor (K = 1.0) will be used along with an uncollimated printed transmission flood source to investigate the accuracy of an uncollimated flood source during transmission computed tomography. Non-uniform radioactive distributions of the printed transmission flood source will also be investigated in order to shorten the transmission acquisition time and/or solve the problem encountered with poor statistical counts during scatter subtraction.

6.11 References

Bailey DL, Hutton BF, Walker PJ (1987). Improved SPECT using simultaneous emission and transmission tomography. *J Nucl Med;* **28:** pp844–851.

Cao Z, Tsui BMW (1992). Performance characteristics of transmission imaging using a uniform sheet source with parallel-hole collimation. *Med Phys;* **19**: pp1205–1212.

Hannequin P, Mas J (1998). Photon energy recovery: a method to improve the effective energy resolution of gamma cameras. *J Nucl Med;* **39**: pp555–562.

Ichihara T, Ogawa K, Motomura N, Kubo A, Hashimoto S (1993). Compton scatter compensation using the triple-energy window method for single-and dual-isotope SPECT. *J Nucl Med*; **34**: pp2216–2221.

Kojima A, Kawanaka K, Nakaura T, Shiraishi S, Utsunomiya D, Katsuda N, Tomiguchi S, Yamashita Y, Matsumoto M, Motomura N, Ichihara T (2004**a**). Attenuation correction using combination of a parallel hole collimator and an uncollimated non-uniform line array source. *Ann Nucl Med*; **18**: pp385–390.

Kojima A, Matsumoto M, Tomiguchi S, Katsuda N, Yamashita Y, Motomura N (2004**b**). Accurate scatter correction for transmission computed tomography using an uncollimated line array source. *Ann Nucl Med;* **18**: pp45–50.

Malko JA, Van Heertum RL, Gullberg GT, Kowaisky WP (1986). SPECT liver imaging using an iterative attenuation correction algorithm and an external flood source. *J Nucl Med*; **27**: pp701–705.

Ogawa K, Harata Y, Ichihara T, Kubo A, Hashimoto S (1991). A practical method for position-dependent Compton-scatter correction in single photon emission CT. *IEEE Trans Med Imag;* **10:** pp408–412.

Van Staden JA, du Raan H, Lötter MG, van Aswegen A, Herbst CP (2007). Production of radioactive quality assurance phantoms using a standard inkjet printer. *Phys Med Biol;* **52**: pp329–337.

Van Staden JA, du Raan H, Lötter MG, Herbst CP, van Aswegen A, Rae WI (2010). Evaluation of an uncollimated printed paper transmission source used under scatter limiting conditions. *Phys Med;* **27**: pp11–20.

Chapter 7

Attenuation Correction in SPECT using an Uncollimated Printed Flood Source

7.1 Introduction

Single Photon Emission Computed Tomography (SPECT) can be used extensively in diagnostic nuclear medicine for qualitatively assessing radiopharmaceutical distributions in vivo (Blokland *et al.*, 1992; Tsui *et al.*, 1994). A major limitation on both qualitative and quantitative SPECT is inaccuracy due to incorrect compensation for attenuated photons (Ficaro *et al.*, 1996). Initially attenuation correction algorithms were based on the assumption that the body is a uniform attenuation medium (Chang, 1978; Glick and Xia, 1997). Although these algorithms are easy to implement they are not suitable for non-uniform regions of the body (King *et al.*, 1996). To correct for attenuation in these non-uniform parts of the body exact information about the attenuation coefficients for a specific radionuclide and tissue type must be known.

The need to perform transmission computed tomography (TCT) in our clinic has led to the development of an in-house transmission system for the existing gamma cameras in our clinic. It was shown that a transmission system which employs an uncollimated transmission flood source can be implemented with minor gamma camera modifications and would fit on most gamma cameras. In a study done by Van Staden *et al.* (2007) it has been demonstrated that high quality flood sources can be created with a standard inkjet printer. An important advantage of a printed paper transmission source is that the activity distribution can be modified to be patient specific. This patient specific activity distribution would provide a more uniform transmission image of the patient than a uniform transmission source. A more uniform transmission image from an uncollimated non-uniform printed flood source would lessen the problem encountered with uniform transmission flood sources when too few counts are recorded in some pixels of the

transmission scan. A printed radioactive source can also be manufactured at low cost to evaluate the use of different activity distributions in the transmission source. Tc-99m would be used for the preliminary evaluation; however a long life radionuclide may be used once a suitable, non-uniform source distribution has been determined. Although major advantages such as low cost, minor or no camera modifications and high yield of an uncollimated transmission source are well known the major limitation of an uncollimated transmission source is the scattered photons in the transmission data and the higher radiation dose to the patient (Cao and Tsui, 1992). If such an uncollimated transmission source is employed for TCT imaging, accurate scatter correction is needed to obtain quantitative SPECT values (Ogawa *et al.*, 1997). Although Van Staden *et al.* (2010) has shown that the scatter contribution in a phantom in planar studies can be limited by increasing the distance from the uncollimated transmission source to the imaging object or applying a scatter correction, these phenomena has not been tested by us in TCT studies.

The aim of this study was to evaluate the transmission images acquired using an uncollimated printed non-uniform radioactive transmission source fixed onto a commercial rotating dual-head gamma camera. The imaging characteristics and calculated attenuation coefficients were investigated in phantom studies by altering the source phantom distance and/or applying a scatter correction to the transmission images.

7.2 Material and methods

The transmission flood source was constructed from a solution of 3 ml of black ink and 0.4 ml of Tc-99m mixed to a concentration of about 123 MBq/ml. This mixture was administered into the ink container of the inkjet printer (Hewlett-Packard DeskJet 1220 C) as explained in Chapter 4, Section 4.2.1. The major constraint of a uniform transmission flood source is that too few counts are often recorded in some pixels in the centre of a patient's transmission image. This was partly overcome by depositing higher amounts of activity at the centre of the printed flood source to create a non-uniform transmission flood source as explained in Chapter 4, Section 4.2.3.4. This non-uniform distributed activity

would provide a higher photon yield at the centre of the FOV, where the attenuation from the scanned object is normally greater. The non-uniform flood source was printed on an A3 size, 297×420 mm^2 paper. The dimensions of the printed area of the non-uniform flood source were 10×420 mm^2. A uniform flood source with similar dimensions as the non-uniform flood source was also constructed.

Acquisition of transmission data

TCT data was acquired with a dual-headed gamma camera (Siemens MultiSPECT II, Hoffman Estate, Chicago, IL) linked to a nuclear medicine computer system (Siemens ICON Power PC8100), (Figure 7.1).

Figure 7.1: *A Siemens MultiSPECT II tomographic camera with affixed transmission source.*

This dual-headed gamma camera is utilize in our clinic for SPECT studies and was therefore used for the evaluation of TCT data acquired with a printed flood source. The printed transmission flood source was attached to the low energy, high resolution (LEHR), parallel-hole collimator of one of the 180° fixed dual-head detectors (transmission detector). The transmission detector was switched off and not used to acquire data. All TCT studies were acquired with the opposite detector (acquisition detector) using a 128 × 128 word matrices through 360°, (Figure 7.2).

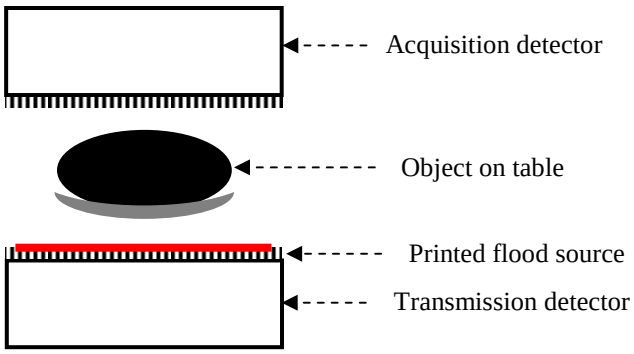

Figure 7.2: *A tomographic dual-head gamma camera with a transmission source attached to the collimator of the transmission detector. A transmission image is acquired with the opposite (acquisition) detector.*

The pixel size of the imaging matrix was 4.8 mm. The transmission data was acquired in 64 projections as this is what is clinically being used for SPECT studies. The acquired transmission data was corrected for scatter by employing the Triple Energy Window (TEW) (Ogawa *et al*., 1991) technique (20% main energy window at 140 keV, 7% lower sub-energy window and 0% upper sub-energy window) with a subtraction factor (K = 1.0) as proposed by Kojima *et al.* (2004) and confirmed from planar transmission data in Chapter 6. To obtain an attenuation map consisting of attenuation coefficients for Tc-99m, two separate transmission image sets were acquired with the acquisition detector. The first set of images was acquired with the object of interest in the FOV of the gamma camera. This set of images is referred to as the transmission image set. The second set of images was acquired with no object in the FOV of the gamma camera. This image set is referred to as the reference image set.

Processing of transmission data

Each transmission projection was corrected for scatter by using the TEW scatter correction method as explained in Chapter 3, Section 3.5.3. These scattered corrected transmission projections were converted to line integral projections using Equation (3.3) as describe in Chapter 3, Section 3.3.1. Using the ordered subsets expectation maximization reconstruction method described in Chapter 2, Section 2.5.1 the sum of the attenuation coefficients along each line of response were then reconstructed to obtain a reconstructed

image consisting of attenuation coefficients. Sixteen subsets and one iteration were used to reconstruct the images.

7.2.1 Planar uniformity with system rotation

For most tomographic gamma cameras, an extrinsic uniformity correction map for each collimator is acquired and applied to all the acquired tomography images. The photomultiplier tubes within the detector of the gamma camera are sensitive to changes of heat, drifting electronics, instable power supply as well as the magnetic field of the earth (Hines *et al*., 2000). Photomultiplier tubes performance characteristics can therefore change as a function of angle of the gamma camera detector which can lead to changes in uniformity with rotation. Changes in uniformity with rotation can introduce non-uniformities in the reconstructed images. A test for the assessment of the stability of uniformity with gantry rotation was done by attaching a uniform printed sheet source to the collimator of one of the detectors of the MultiSPECT II gamma camera. Sixteen projections were acquired over a 360° circular orbit in a 64 × 64 acquisition matrix. For each projection image 9 million counts were acquired, resulting in a statistical error of ~2% per pixel. The uniformity as well as the variation in the total counts in each projection was calculated to determine the stability of the gamma camera with rotation. The integral and differential uniformity figures for each of the 16 projection images were calculated as prescribe by NEMA (2001).

7.2.2 Resolution of the reconstructed TCT images

The system resolution was evaluated by using a Perspex cylindrical phantom (Data Spectrum Corp., Chapel Hill, NC) with a diameter of 22 cm, (Figure 7.3). This phantom provided a means of evaluating the reconstructed TCT resolution of the printed transmission flood source. The phantom was imaged without water which created an air-to-Perspex object contrast. The inserts of the phantom consisted of five different size solid spheres and rods. The diameters of the five spheres were 12.7 mm, 15.9 mm, 19.1 mm,

25.4 mm and 31.8 mm. The 88 mm long rods were arranged in six pie-shaped sectors, with each sector having the same diameter. The rod diameters were 4.8 mm, 6.4 mm, 7.9 mm, 9.5 mm, 11.1 mm and 12.7 mm, and the centre-to-centre spacing between the rods was twice the diameter.

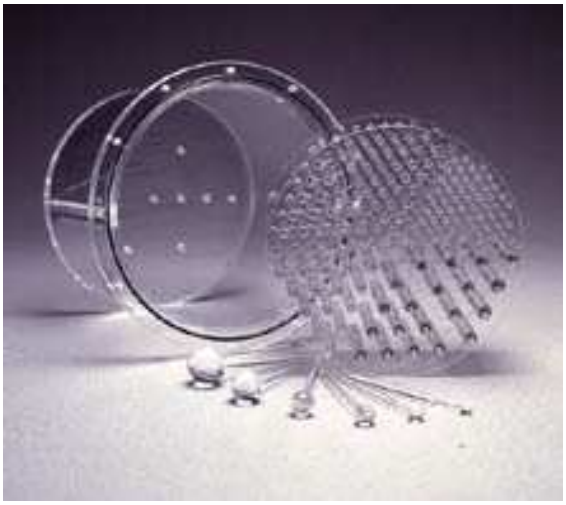

Figure 7.3: *A Perspex cylindrical phantom (Data Spectrum Corp., Chapel Hill, NC) containing solid rod and spheres inserts.*

To evaluate transverse resolution, the phantom was oriented with the rods parallel to the axis of rotation (AOR) of the detector. The phantom was attached onto a steel pole and positioned parallel to the AOR at the centre of rotation (COR) of the camera. A 185 MBq non-uniform flood source, printed as describe in Chapter 4. Section 4.2.1, was attached to the collimator of the transmission detector. Data were acquired with the transmission and acquisition detector at different positions as indicated in Table 7.1.

The transmission detector with the non-uniform flood source was position at a distance of 30 cm from the COR. Two sets of transmission images of the Perspex rod phantom were acquired with the dual-head gamma camera as described in Section 7.2 with the acquisition detector set at fixed distances of 30 cm (Data Set 1-1and 15 cm Data Set 1-2) respectively from the COR.

Table 7.1: *Distance measurements as obtained for each data set.*

TCT Data Set	Transmission Detector with transmission source	Acquisition Detector
Data Set 1-1	30 cm from the COR	30cm from the COR
Data Set 1-2	30 cm from the COR	15 cm from the COR
Data Set 2-1	15 cm from the COR	30cm from the COR
Data Set 2-2	15 cm from the COR	15 cm from the COR

The count rates for all the tomographic acquisitions did not exceed that which would produce an 8% dead time loss. The time per projection was set at 20s per projection and was adjusted to give the same total counts in the first projection for all configurations. A primary energy window of 15% centred over the Tc-99m photo-peak was used. As the phantom was imaged without water to provide good object contrast no transmission scatter lower sub-energy window was utilized for this experiment. All projections were corrected using linearity and energy correction files.

Reference transmission images, without the phantom and table pallet, were also acquired for each transmission acquisition detector distance as described above. The time per projection for the reference scans was the same as for the transmission images. Transmission projections were converted to attenuation projections and reconstructed as explained in Chapter 3, Section 3.3.1.

7.2.3 The contribution of scattered photons in TCT images

The scatter contribution from the uncollimated printed transmission source was evaluated with a Perspex phantom (Data Spectrum Corp., Chapel Hill, NC) similar to the phantom described in Section 7.2.2. For this experiment the inserts of the Perspex phantom were removed and the cylindrical phantom (22 cm in diameter) was filled with water. To evaluate the contribution of scattered photons, the tightly sealed, water filled cylindrical

phantom was attached onto a steel pole and positioned parallel to the AOR at the COR of the SPECT camera, (Figure 7.4).

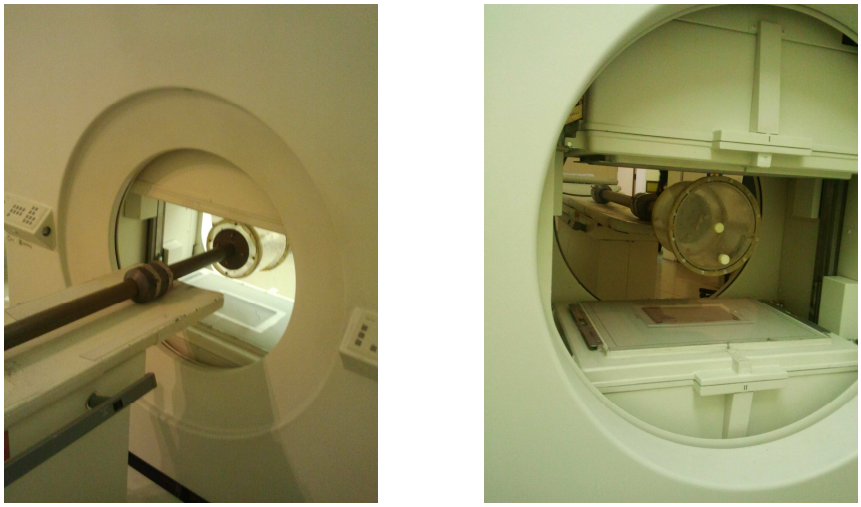

Figure 7.4: *A water filled cylindrical phantom attached onto a steel pole and positioned parallel to the AOR at the COR of the gamma camera.*

A 185 MBq non-uniform flood source, printed as described in Section 7.2.2, was attached onto the collimator of the transmission detector. Two sets of transmission images of the water filled phantom were acquired with the acquisition detector set at a fixed distance of 15 cm from the COR. For each acquisition the transmission detector with the flood source was set at a fixed distances of 15 cm and 30 cm respectively from the COR as describe in Section 7.2.2 and similar to Data Set 2-2 and Data Set 1-2 as described in Table 7.1. The time per projection was set at 30 s per projection. For these transmission images a primary energy window of 20% centred over the Tc-99m (140 keV) photo-peak as well as a lower sub-energy window of 7% centred over 126 keV were used as explained in Chapter 3, Section 3.5.3.

Reference transmission images, without the phantom and table pallet, were also acquired for each transmission-acquisition detector distance as described in Section 7.2.2. The time per projection for the reference scans were the same as for the transmission images. Each transmission projection was corrected for scatter by applying the TEW scatter correction

technique (K = 1.0) to the acquired transmission images as explained in Chapter 3, Section 3.5.3. These scatter corrected transmission images were then converted to attenuation projections and reconstructed as explained in Chapter 3, Section 3.3.1.

For the two transmission-acquisition detector configurations, a reconstructed transaxial slice 4.8 mm thick was created, through which a 1 cm thick profile was drawn. The mean attenuation coefficient in a large circular ROI (500 pixels) drawn in the centre of the transmission images was obtained and the error expressed as the standard deviation of the attenuation coefficient.

7.2.4 TCT of a human head phantom

The accuracy of the attenuation coefficients of a human head phantom was evaluated by using the head portion of the RANDO phantom (Alderson Research Laboratories Inc., Stamford, CT). This phantom consist of 2 cm thick slices of a human adult dried skull, filled with and surrounded by tissue-equivalent material (Alderson Research Laboratories), (Figure 7.5).

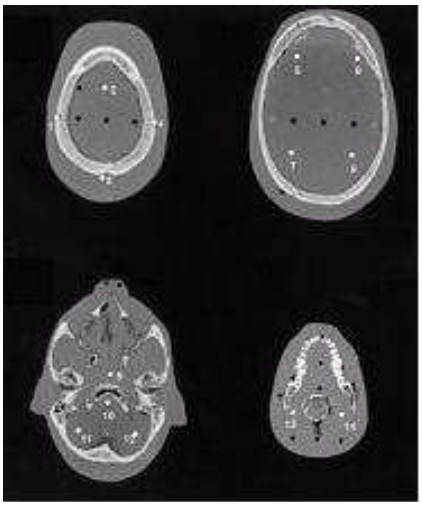

Figure 7.5: *Transaxial computed tomography scans of head and neck portion of RANDO anthropomorphic phantom.*

A 185 MBq non-uniform flood source, printed as described in Section 7.2.2, was attached onto the collimator of the transmission detector. A set of transmission images of the head portion of the phantom was acquired with the acquisition detector set at a fixed distance of 15 cm and the transmission detector with the flood source set at 30 cm from the COR as described in Section 7.2.2 and similar to Data Set 1-2 as described in Table 7.1. The time per projection was set at 30 s per projection and a primary energy window as well as a lower sub-energy window were used as explained in Section 7.2.3.

Reference transmission images, without the phantom and table pallet, were also acquired similar to Data Set 1-2 as described in Table 7.1. The time per projection for the reference scans were the same as for the transmission images. Each transmission projection was corrected for scatter and these scatter corrected transmission images were converted to attenuation projections and reconstructed as explained in Section 7.2.3.

For the transmission-acquisition detector configuration, a transverse slice of one pixel thick (4.8 mm) was created. The mean attenuation coefficient of the brain tissue was measured from ROIs drawn on five transverse images. The error is expressed as the mean standard deviation of the attenuation coefficients within the ROIs.

7.3 Results

7.3.1 Planar uniformity with system rotation

The average uniformity parameters of the flood field images obtained at 16 different angles using a uniform printed Tc-99m flood source was calculated according to NEMA for the central field of view (CFOV). The integral uniformity was 5.27 ± 1.30% for the printed Tc-99m flood source. The standard deviation indicates a small angular variation of the uniformity. The total counts were obtained for each projection and normalized to the counts of the first projection. The average of the total counts for the different projections

was 100.50 ± 0.26% for the Tc-99m study. The small standard deviation indicates that the gamma camera was stable with rotation.

7.3.2 Resolution of the reconstructed TCT images

The tomographic resolution was evaluated after reconstruction of images obtained with the DeLuxe 5000 Data spectrum phantom. The transaxial images of the resolution phantom are shown in Figure 7.6.

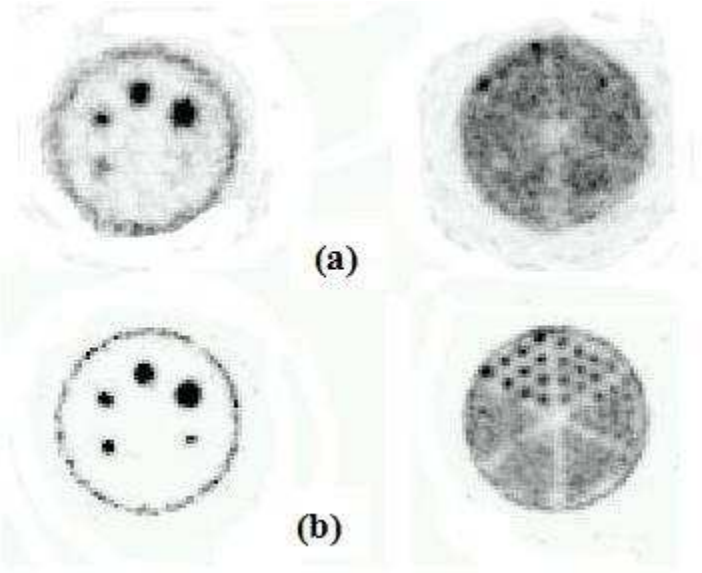

Figure 7.6: *(a) The transaxial images of the solid Perspex spheres and rods obtained with the transmission detector set at a distance of 30 cm and the acquisition detector at a distance of (a) 30 cm (Data Set 1-1) and (b) 15 cm (Data Set 1-2) from the COR.*

With both the transmission and acquisition detectors at distances of 30 cm from the COR (Data Set 1-1) four of the five solid Perspex spheres of the resolution phantom were visible Figure 7.6.(a). The smallest visible sphere has a diameter of 12.7 mm. At these transmission-acquisition detector distances none of the six sectors of the Perspex rods could be distinguished. All five solid Perspex spheres were visible when the transmission detector was kept at a fix distance of 30 cm and the acquisition detector was moved to a fix distance of 15 cm from the COR (Data Set 1-2), (Figure 7.6.(b)). With the acquisition

detector at a fix distance of 15 cm from the COR, all six sectors could be distinguished (Figure 7.6.(b)). The rods with diameters of 9.5 mm , 11.1 mm and 12.7 mm could be identified separately (Figure 7.6.(b)). This inferior resolution which was obtained with an increase in the acquisition detector distance from the COR corresponded with the results that were founded by Cao and Tsui, (1992) for planar transmission imaging and was confirmed by the resolution results obtained in Chapter 5, Section 5.3.4.

From these results it is evident that TCT resolution with an uncollimated flood source is dependent upon the distance between the object and the acquisition detector and not the distance between the transmission source and the object as was reported by Cao and Tsui, (1992).

7.3.3 The contribution of scattered photons in TCT images

The first set of acquired transmission projections with the transmission detector set at a distance of 15 cm from the COR (Data Set 2-1) was converted to attenuation projections and reconstructed as explained in Section 7.2.3. For the 4.8 mm thick reconstructed slice a mean attenuation coefficient of 0.103 ± 0.011 cm^{-1} for water was obtained (—), (Figure 7.7). This measured mean attenuation coefficient for water was lower than the published value of 0.149 cm^{-1} for 140 keV photons (Brown *et al.*, 2008) but it compares favourably with the attenuation coefficient value for water (0.093 cm^{-1}) obtained for an uncollimated transmission flood source as published by Bailey *et al.* (1987). This significant difference between the measured and published attenuation coefficient value for water can be attributed to the large number of scattered photons which were generated and accepted in the photo-peak window at small source phantom distances.

The next step was to apply the TEW scatter correction (K = 1.0) to the transmission images acquired with the transmission detector set at a fix distance of 15 cm from the COR (Data Set 2-1). These scatter corrected transmission images were converted to attenuation projections and reconstructed as explained in Section 7.2.3. A mean attenuation

coefficient of 0.148 ± 0.013 cm^{-1} was obtained for a reconstructed transaxial slice of width 4.8 mm (—), (Figure 7.7). This measured mean attenuation coefficient for water compare favourably with the narrow beam linear attenuation coefficient value for water for 140 keV photons (0.149 cm^{-1}) as reported by Brown *et al.*, (2008).

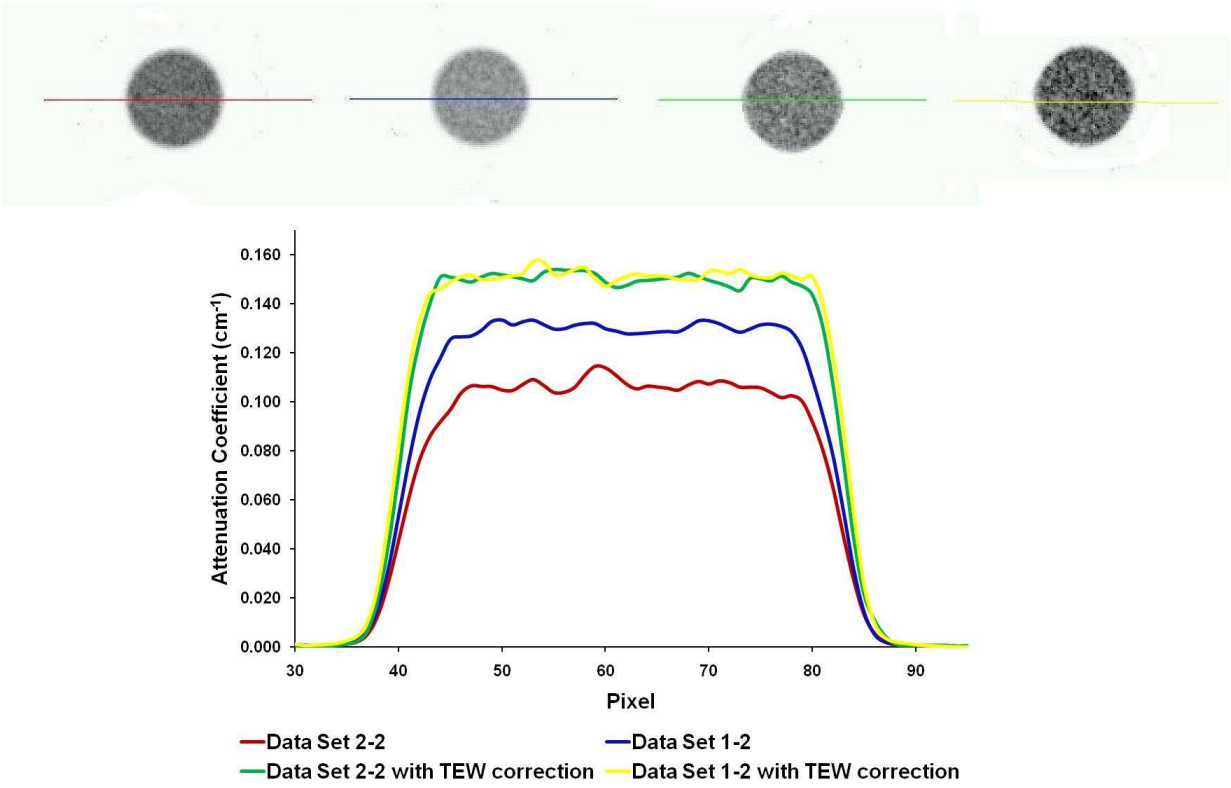

Figure 7.7: *Reconstructed attenuation coefficient images of the water filled cylindrical phantom along with profiles through the images using an uncollimated, non-uniform, printed sheet source at detector source distances of 15 cm (Data Set 2-2) and 30 cm (Data Set 1-2) and the acquisition detector at a distance of 15cm with and without the TEW scatter correction.*

For the second set of acquired transmission projections with the transmission detector set at a fix distance of 30 cm from the COR (Data Set 1-1) the mean attenuation coefficient obtained for water for the 4.8 mm thick reconstructed transaxial slice was 0.126 ± 0.010 cm^{-1} (—), (Figure 7.7).. Although this attenuation coefficient value was lower than the published narrow beam linear attenuation coefficients value for water for 140 keV photons (Brown *et al.*, 2008), it compares favourably with the attenuation coefficient value

for water obtained for an uncollimated transmission flood sources as published by Bailey *et al.* (1987).

The TEW scatter correction with a subtraction factor K set equal to 1.0 was applied to the transmission images acquired at a set distance of 30 cm from the COR (Data Set 1-1). These scatter corrected transmission images were converted to attenuation projections and reconstructed as explained in Section 7.2.3. A mean attenuation coefficient of $0.149 \pm 0.011\ cm^{-1}$ was obtained for a 4.8 mm thick reconstructed slice of the water phantom (—**)**, (Figure 7.7). This measured mean attenuation coefficient for water compare favourably with the attenuation coefficient value for water ($0.149\ cm^{-1}$) as reported by Brown *et al.*, (2008) which was obtained with a collimated Tc-99m source.

7.3.4 TCT of a human head phantom

The mean attenuation coefficients for the brain tissue of the head of the RANDO phantom for Data Set 2-1 measured from ROIs drawn on five transverse images of one pixel thick was $0.159 \pm 0.01\ cm^{-1}$. This measured mean attenuation coefficient for brain tissue was lower than the published value for brain tissue ($0.161\ cm^{-1}$) for 140 keV photons (ICRU report, 1989). The percentage difference of 1.2% between the measured attenuation coefficient value and the value documented by ICRU is similar to the percentage difference (2%) which was reported by Brown *et al.*, (2008) for attenuation coefficient values measured with 140 keV photons. This underestimation of the attenuation coefficient value for brain tissue at 140 keV can be due to the limited energy resolution of the gamma camera and the partial energy deposition of gamma rays which produces background noise.

7.4 Discussion

Accurate attenuation maps are important for quantitative SPECT imaging. The feasibility of using an uncollimated printed flood source to determine accurate attenuation maps for

transmission imaging was evaluated in this chapter. In this study we have presented a new design for a transmission source and evaluated the quality of the attenuation maps generated with this source. An important advantage of this uncollimated printed transmission system is that it can be used with single- or dual-head SPECT gamma camera systems and little or no modifications to the gantry system of the gamma camera is required. The low cost non-uniform printed source for the transmission system can be constructed with an inkjet printer and will provide a high photon yield due to no source collimation. A high photon yield will allow the user to lower the source activity or conduct fast transmission imaging.

The small standard deviations that were obtained for the uniformity values during tomography indicate a small angular variation of the uniformity values. These small standard deviations indicate that the detector was stable with rotation.

The tomographic spatial resolution results obtained with the uncollimated transmission flood source are comparable to the resolution results obtained by Du Raan *et al.*, (2000) with a scanning line source with parallel hole collimation. All five spheres as well as three of the six sectors containing the Perspex rods were visible with the emission detector at a fix distance of 15 cm from the COR. The tomographic spatial resolution has deteriorated when the emission detector distance increased from 15 cm to 30 cm from the COR. At 30 cm none of the Perspex spheres or rods were visible. From these results it is clear that the tomographic spatial resolution for TCT with an uncollimated flood source is dependent on the distance of the emission detector from the phantom (detector phantom distance) and not of the transmission detector from the phantom (detector source distance). Similar spatial resolution results were reported by Cao and Tsui (1992) for planar transmission imaging.

The accuracy of the attenuation coefficient values acquired with TCT was evaluated for a cylindrical Perspex phantom filled with water. From the results, it was clear that the attenuation coefficient values of water obtained with TCT increased as the distance between the uncollimated transmission source and the Perspex phantom increased.

Although the attenuation coefficient values show an increase by increasing the distance between the transmission source and the Perspex phantom (detector phantom distance) the attenuation coefficient value for water as reported by Brown *et al.,* (2008) was still underestimated with the transmission detector at a fix distance of 30 cm from the COR. This underestimation of the attenuation coefficient value can be contributed to the limited effective source to phantom distance of 19 cm. There was however a marked increase ($0.103 \pm 0.011\ cm^{-1}$ vs. $0.126 \pm 0.010\ cm^{-1}$) in the attenuation coefficient values as the effective transmission source to phantom distance increased from 4 cm to 19 cm. This lower attenuation coefficient value of water for TCT at an effective source phantom distance of 19 cm obtained with an uncollimated flood source can be attributed to the number of scattered events which were present in the acquired transmission images at the source phantom distance of 19 cm. These results were similar to the results reported by Van Staden *et al.,* (2010) for attenuation coefficients values obtained for planar transmission imaging with an uncollimated printed flood source at source phantom distances < 40 cm.

This limitation of the distance between the transmission source and the object is a limitation to many commercial SPECT gamma cameras. This limited source phantom distance which can be obtained with most commercial SPECT gamma cameras has emphasized the need to perform accurate scatter correction to the transmission data acquired with uncollimated flood sources during TCT. The attenuation coefficient values for the water filled Perspex phantom acquired with the transmission detector at distances of 15 cm ($0.148 \pm 0.013\ cm^{-1}$) and 30 cm ($0.149 \pm 0.011\ cm^{-1}$) from the COR compared favourably to the value of water as reported by Brown *et al.,* (2008) after applying the TEW scatter correction (K = 1.0) to the transmission images.

After applying the TEW scatter correction technique with a subtraction factor K=1.0 to the transmission projections of the head portion of the RANDO phantom the mean attenuation coefficients for the brain tissue values were calculated. From these results it was evident that the attenuation coefficient values for the brain tissue were slightly underestimated.

This underestimation can be attributed to an underestimation of the scatter contribution in the transmission images acquired with an uncollimated flood source.

Although many different solutions to attenuation corrections have been proposed, practical obstacles exist in the routine clinical implementation of attenuation correction. One of the problems is that the geometry of SPECT detectors does not always lend itself to the performance of transmissions scans. Even if the geometry is accommodating, custom hardware modifications to the gantry are necessary in order to accommodate these transmission scans. Such hardware changes are often beyond the capability of many nuclear medicine departments due to the high cost involved. Furthermore the gantry of the gamma camera does not always permit major modifications. One proposal would be to use a transmission configuration that requires no modifications to the existing gantry system. In our clinic the gamma camera has dual imaging detectors fitted with high resolution parallel-hole collimators. It has been shown that the scatter contribution in the transmission images can be limited by increasing the phantom source distance. This scatter limitation by increasing the phantom source distance was not possible with the SPECT system used in this study due to the 180° fixed detectors. This scatter limited technique would be possible in a SPECT system with one detector or a SPECT system with an open gantry and would be worth investigating as an alternative for transmission imaging.

Our suggestion of using an uncollimated printed transmission source along with a modified version of the TEW scatter correction technique to conduct TCT was performed successfully in this study. Acquisition software which allows more pre-selected energy windows to be used would permit the user to employ alternative scatter correction techniques such as the PER technique described in Chapter 6. The transmission source has been primarily designed for SPECT imaging, but may be applied for planar imaging, or in quality control procedures.

7.5 References

Bailey DL, Hutton BF, Walker PJ (1987). Improved SPECT using simultaneous emission and transmission tomography. *J Nucl Med;* **28:** pp844–851.

Blockland KA, Reiber HC, Pauwels EK (1992). Quantitative analysis in single photon emission tomography (SPET). *Eur J Nucl Med;* **19:** pp47–61.

Brown S, Bailey DL, Willowson K, Baldock C (2008). Investigation of the relationship between linear attenuation coefficients and CT Hounsfield units using radionuclides for SPECT. *Appl Radiat Isot;* **66:** pp1206–1212.

Cao Z, Tsui BMW (1992). Performance characteristics of transmission imaging using a uniform sheet source with parallel-hole collimation. *Med Phys;* **19**: pp1205–1212.

Chang LT (1978). A method for attenuation correction in radionuclide computed tomography. *IEEE Trans Nucl Sci;* **25:** pp638–643.

Du Raan H, du Toit PD, van Aswegen A, Lötter MG, Herbst CP, van der Walt TN, Otto AC (2000). Implementation of a Tc-99m and Ce-139 scanning line source for attenuation correction in SPECT using a dual opposing detector scintillation camera. *Med Phys;* **27:** pp1523–1534.

Ficaro EP, Fessler JA, Shreve PD, Kritzman JN, Rose PA, Corbett JR (1996). Simultaneous transmission/emission myocardial perfusion tomography. Diagnostic accuracy of attenuation-corrected 99mTc-sestamibi single-photon emission computed tomography. *Circulation;* **93**: pp463–473.

Glick S, Xia W (1997). Iterative restoration of SPECT projection images. *IEEE Trans Nucl Sci;* **44**: pp204–211.

Hines H, Kayayan R, Colsher J, Hashimoto D, Schubert R, Fernando J, Simcic V, Vernon P, Sinclair R (2000). National electrical manufacturers association recommendations for implementing SPECT instrumentation quality control. *J Nucl Med;* **41**: pp383–389.

ICRU Report 44 (1989). Tissue substitutes in radiation dosimetry and measurement, 1989.

King MA, Tsui BM, Pan TS, Glick SJ, Soares EJ (1996). Attenuation compensation for cardiac single-photon emission computed tomographic imaging: Part 2. Attenuation compensation algorithms. *J Nucl Cardiol;* **3**: pp55–64.

Kojima A, Kawanaka K, Nakaura T, Shiraishi S, Utsunomiya D, Katsuda N, Tomiguchi S, Yamashita Y, Matsumoto M, Motomura N, Ichihara T. (2004). Attenuation correction

using combination of a parallel hole collimator and an uncollimated non-uniform line array source. *Ann Nucl Med*; **18**: pp385–390.

NEMA Standard Publication NU **1**, 2001. Performance Measurements of Scintillation Cameras.

Ogawa K, Harata Y, Ichihara T, Kubo A, Hashimoto S (1991). A practical method for position-dependent Compton-scatter correction in single photon emission CT. *IEEE Trans Med Imag;* **10**: pp408–412.

Ogawa K, Kubo A, Ichihara T (1997). Estimation of scattered photons in gamma ray transmission CT using Monte Carlo simulations. *IEEE Trans Nucl Sci;* **44**: pp1225–1230.

Tsui BM, Zhao X, Frey EC, McCartney WH. (1994). Quantitative single-photon emission computed tomography: basics and clinical considerations. *Semin Nucl Med*; **24**: pp38–65.

Van Staden JA, du Raan H, Lötter MG, van Aswegen A, Herbst CP (2007). Production of radioactive quality assurance phantoms using a standard inkjet printer. *Phys Med Biol;* **52**: pp329–337.

Van Staden JA, du Raan H, Lötter MG, Herbst CP, van Aswegen A, Rae WI (2010). Evaluation of an uncollimated printed paper transmission source used under scatter limiting conditions. *Phys Med;* **27**: pp11–20.

Summary

Several factors influence the quality of Single Photon Emission Tomography (SPECT) images. The most prominent of these are the effect of tissue attenuation and radiation scatter. Attenuation may lead to artefacts and quantitative inaccuracies in reconstructed images, occurrences that are particularly disturbing in clinical studies such as myocardial perfusion imaging because of the highly non-uniform composition of tissue in the thorax region. The importance of accurate compensation for attenuation effects in SPECT is already widely recognized and several studies have demonstrated that image quality can be considerably improved by incorporating attenuation correction into an iterative reconstruction method. The main aim of this study was the production and evaluation of an uncollimated printed transmission flood source along with a scatter correction for transmission imaging.

In our clinic there is currently no mechanism available for radionuclide transmission imaging and the need to perform transmission computed tomography (TCT) has forced us to investigate the possibility of developing a transmission system for the existing older generation gamma cameras in our clinic. Transmission flood sources for the available gamma cameras were designed and produced in-house by printing the sources on paper with a digital inkjet printer. Due to the negligible weight of a printed paper source, older existing gamma cameras can easily be customized to allow transmission imaging by using an uncollimated printed transmission flood source. By using a scatter correction or altering the distance between the transmission source and the patient the large number of scattered photons in the transmission data due to the uncollimated transmission flood source can be limited. The production process of the printed sources and their application for transmission imaging were evaluated in this study.

It was shown that the deposition of the amount of radioactivity for transmission sources could be predicted to an acceptable level. This is an indication that the amount of printed activity was reproducible. The uniformity of the printed sources compared well to the uniformity values obtained with a commercial Co-57 flood source indicating acceptable printing uniformity. It

was also shown that joining two printed A4-size phantoms to create a larger composite phantom does not significantly affect the uniformity attained. We have demonstrated that affordable flood sources can easily be created in any department where a standard PC and inkjet printer are available. It should therefore be possible to create any size and source distribution, suggesting that routine extrinsic uniformity corrections could be performed on gamma camera using such printed radioactive flood sources. In this study it has also been demonstrated that any distribution of radioactivity in the printed flood source can be attained by using an inkjet printer fitted with a cartridge filled with a mixture of ink and radioactivity.

The detector source and detector phantom distances where the least scatter and the best spatial resolution were obtained by using a novel uncollimated printed radioactive paper source were determined for planar transmission imaging. Although the evaluation focused on planar imaging it is also applicable to the projections acquired during SPECT data acquisition. As mentioned before the printed transmission source could easily be attached to an existing gamma camera since no additional heavy transmission collimation or major modification to the gantry of the gamma camera was necessary to perform transmission imaging. From the results obtained with the uncollimated transmission flood sources, the estimated scatter percentages indicated that the scatter contribution in the acquired energy spectra increased with a decrease in the detector source distance. It was shown that for the smallest possible detector phantom distance, the scattered photons in the acquired transmission image was limited at detector source distances greater than 60 cm. At these distances the attenuation coefficient value obtained for the uncollimated transmission source compared favourable to the value obtained with the collimated transmission source. From these results it is evident that transmission imaging with an uncollimated transmission source at detector source distances of less than 60 cm would result in an underestimation of the attenuation coefficient values due to the presence of a large number of scattered photons in the acquired transmission images. An underestimation of the attenuation coefficient values will result in an overestimation of activity during emission image quantification.

Although scatter lowers the contrast and deteriorates image quality, the planar spatial resolution values measured with an uncollimated printed flood source have shown a small improvement when the scatter was decreased by increasing the detector source distance from 20 cm to 80 cm. At these distances the spatial resolution values, measured with and without a scatter medium present, compared favourably with the values obtained using a collimated transmission flood source. The spatial resolution values obtained with an uncollimated printed flood source shown a marked deterioration with an increase in the detector phantom distance at fixed detector source distances (20 cm – 80 cm). The constant detection efficiency which was observed when the uncollimated transmission source was moved from 0 cm to 30 cm from the gamma camera detector was reduced with a factor of 2.5 when the source was collimated. An uncollimated non-uniform transmission source would provide higher detection efficiency than a uniform collimated flood source which would reduce the transmission acquisition time. A reduction in the transmission acquisition time is highly desirable in order to reduce the total imaging time and exposure to the patient.

From the above results it is clear that the scatter contribution in the transmission images acquired with an uncollimated flood source can be limited by increasing the detector source distance. A detector source distance larger than 60 cm is not always possible on all SPECT gamma cameras and therefore a possible solution to this problem would be to apply a scatter correction to the transmission data acquired with the uncollimated flood source. The Triple Energy Window (TEW) and Photon Energy Recovery (PER) scatter correction techniques were used to remove scattered events from the transmission data acquired with the uncollimated flood source.

The TEW scatter correction technique was modified by changing the subtraction factor K from 0.5 to 1.0. This resulted in more accurate scatter percentages as well as attenuation coefficient values after applying the TEW scatter correction technique to the transmission data.

The PER scatter correction technique was evaluated by selecting different numbers of sub-energy windows to obtain the energy spectrum. The selected sub-energy windows were always

selected to include the Tc-99 photo-peak. The numbers of selected sub-energy windows were 3, 9 and 52. Selecting only 3 sub-energy windows over the photo-peak resulted in an underestimation of the scatter contribution as well as the attenuation coefficient values obtained from the transmission data. Although an increase from 3 to 9 or 52 pre-selected sub-energy windows has led to more accurate scatter estimations and attenuation coefficients, larger differences between the three data sets were obtained when 9 or 52 sub-energy windows were selected. These larger differences between the three data sets show that the PER technique was more unstable than the TEW scatter correction method when more sub-energy windows were selected. The instability of the PER technique when more sub-energy windows were selected indicates that the technique is more sensitive to small variations in the energy signal of the gamma camera. Furthermore, due to computer software limitations it is difficult or even impossible to select large numbers (9 or 52) of sub-energy windows for SPECT data acquisition. Selecting larger number of sub-energy windows also resulted in reduced count statistics. Due to all the above mentioned problems it was decided to use the TEW scatter correction technique instead of the PER technique for SPECT data.

Finally the feasibility to perform TCT was evaluated by using an uncollimated non-uniform printed flood source along with a SPECT gamma camera. From the results obtained with the Deluxe Data Spectrum phantom with the resolution inserts it was clear that the tomographic resolution obtained with the uncollimated printed flood source was dependant on the distance of the acquisition detector from the phantom and not on the distance between the transmission source and the phantom. Although an increase in the phantom source distance has led to an improvement in the attenuation coefficient values, these values were still lower than the value reported in literature due to the number of scattered events present in the reconstructed slice. The underestimation of the scatter contribution and the attenuation coefficient values due to an inadequate phantom source distance is a limitation of many commercial SPECT gamma cameras. This underestimation of the attenuation coefficient values of the water filled phantom was corrected for by applying the TEW scatter correction with an adjusted subtraction factor (K = 1.0) to the transmission data acquired with an uncollimated printed flood source.

This study showed that accurate attenuation coefficient values could be obtained using an uncollimated non-uniform printed transmission source along with an appropriate scatter correction. These attenuation coefficient values were obtained from TCT imaging with the printed uncollimated flood source with no gamma camera modifications.

APPENDIX A

Scatter Percentage (%Sc) in a 20% energy window for the transmission source for various detector source distances for thicknesses of Perspex ranging from 0 to 20 cm. The average and standard deviation (Stdev) for 3 measurements are given for Data Set 1 (Table A1), Data Set 2 (Table A2) and the collimated data for Data Set 1 (Table A4). Data Set 3 was only measured once (Table A3).

TABLE A1: *Scatter Percentage (%Sc) in the 20% energy window for Data Set 1 for the uncollimated transmission source for various detector source distances (DSD) for thicknesses of Perspex (0 – 20 cm) was calculated as the ratio of scattered to total counts and expressed as a percentage.*

DSD (cm)	20		40		60		80	
Thickness (cm)	**%Sc**	**Stdev**	**%Sc**	**Stdev**	**%Sc**	**Stdev**	**%Sc**	**Stdev**
1.1	8.2	0.5	2.7	0.3	1.3	0.2	1.7	0.6
3.2	21.0	0.7	7.8	0.5	4.6	0.5	4.8	0.6
5.4	29.8	0.6	11.7	0.9	7.3	1.4	7.6	0.9
7.5	35.8	0.4	15.5	0.9	9.6	1.5	9.4	0.3
9.6	40.3	0.5	18.5	0.9	10.5	1.9	10.5	0.8
11.8	44.1	0.4	20.6	1.3	11.9	1.8	11.8	1.0
13.9	46.8	0.4	23.3	0.9	14.0	1.2	13.2	0.6
16.1	49.0	0.3	25.1	1.0	15.3	1.7	14.2	0.6
18.2	51.0	0.5	27.4	0.1	17.4	1.0	15.3	1.0
20.3	52.4	0.5	28.9	0.9	18.8	0.6	16.3	0.3

TABLE A2: *Scatter Percentage (%Sc) in the 20% energy window for Data Set 2 for the uncollimated transmission source for various detector source distances (DSD) for thicknesses of Perspex (0 – 20 cm) was calculated as the ratio of scattered to total counts and expressed as a percentage.*

DSD (cm)	20		40		60		80	
Thickness (cm)	**%Sc**	**Stdev**	**%Sc**	**Stdev**	**%Sc**	**Stdev**	**%Sc**	**Stdev**
1.1	1.1	0.2	1.1	0.4	2.3	0.5	7.4	0.3
3.2	3.3	0.7	4.1	0.2	6.5	0.6	18.8	0.7
5.4	5.3	0.1	6.6	0.3	10.3	0.6	27.1	1.1
7.5	6.4	0.8	8.1	0.8	13.0	1.6	32.5	2.0
9.6	7.3	1.5	9.9	1.2	15.2	1.6	36.9	2.3
11.8	8.7	0.7	11.4	0.2	17.8	1.3	40.5	2.2
13.9	9.9	0.9	13.1	0.4	20.2	1.1	43.5	2.4
16.1	11.9	1.0	14.9	0.9	22.2	1.2	45.8	2.8
18.2	12.8	0.6	16.0	0.3	24.0	1.9	47.8	3.2
20.3	14.7	0.9	17.1	0.1	25.5	1.3	49.4	3.1

TABLE A3: *Scatter Percentage (%Sc) in the 20% energy window for Data Set 3 for the uncollimated transmission source for various detector source distances (DSD) for thicknesses of Perspex (0 – 20 cm) was calculated as the ratio of scattered to total counts and expressed as a percentage.*

DSD (cm)	20	40	60	80		
Thickness (cm)	**%Sc**	**%Sc**	**%Sc**	**%Sc**	**Avg**	**Stdev**
1.1	8.1	8.4	7.5	7.8	8.0	0.4
3.2	20.5	19.8	19.4	19.7	19.9	0.5
5.4	28.2	27.2	26.9	27.7	27.5	0.6
7.5	34.8	34.5	33.6	34.7	34.4	0.5
9.6	39.2	38.8	37.9	38.7	38.7	0.6
11.8	43.2	42.3	41.6	42.8	42.5	0.7
13.9	45.9	45.3	44.6	45.3	45.3	0.5
16.1	48.5	47.7	47.6	48.1	48.0	0.4
18.2	51.0	50.2	50.4	50.4	50.5	0.4
20.3	52.9	52.1	52.3	52.4	52.4	0.3

TABLE A4: *Scatter Percentage (%Sc) in the 20% energy window for Data Set 1 for the collimated transmission source for various detector source distances (DSD) for thicknesses of Perspex (0 – 20 cm) was calculated as the ratio of scattered to total counts and expressed as a percentage.*

DSD (cm)	20		40		60		80	
Thickness (cm)	**%Sc**	**Stdev**	**%Sc**	**Stdev**	**%Sc**	**Stdev**	**%Sc**	**Stdev**
1.1	1.9	0.6	1.8	0.5	1.7	0.6	1.3	0.2
3.2	3.9	0.5	3.5	0.2	4.6	1.0	3.3	0.1
5.4	5.7	1.2	5.8	0.3	6.9	0.3	5.1	0.2
7.5	7.4	1.1	7.2	0.6	8.4	0.6	6.7	0.5
9.6	9.3	1.0	8.9	1.2	9.8	0.9	8.4	0.5
11.8	10.5	1.6	10.2	1.2	11.6	0.3	9.7	0.4
13.9	11.7	2.7	11.6	1.5	12.3	0.6	10.6	0.1
16.1	13.1	1.9	12.7	1.9	13.0	1.5	12.5	0.8
18.2	13.6	1.7	13.2	1.8	13.9	1.1	13.7	1.2
20.3	14.7	1.0	14.5	1.2	15.7	1.1	15.2	0.6

APPENDIX B

The attenuation coefficient values as a function of detector source distances (DSD) for the transmission source for various detector source distances. The average (Avg) and standard deviation (Stdev) for 3 measurements are given for Data Set 1 (Table B1), Data Set 2 (Table B2) and the collimated data for Data Set 1 (Table B4) and Data Set 3 (Table B6). Data Set 3 was only measured once (Table B3) and the collimated data for Data Set 2 (Table 5) was only measured for a detector source distance of 80 cm.

TABLE B1: *The attenuation coefficient values (cm^{-1}) as a function of detector source distances (DSD) for a detector phantom distance of 20 cm for the uncollimated transmission source (UTS) for Data Sets 1.*

DSD (cm)	Avg	Stdev	% Stdev
20	0.141	0.003	1.823
40	0.160	0.002	1.501
60	0.167	0.003	1.721
80	0.168	0.003	1.632

TABLE B2: *The attenuation coefficient values (cm^{-1}) as a function of detector phantom distances (DPD) for a detector source distance of 80 cm for the uncollimated transmission source (UTS) for Data Sets 2.*

DPD (cm)	Avg	Stdev	% Stdev
20	0.171	0.000	0.102
40	0.169	0.000	0.034
60	0.164	0.001	0.520
80	0.144	0.000	0.175

TABLE B3: *The attenuation coefficient values (cm^{-1}) as a function of detector source distances (DSD) for a source phantom distance of 0 cm for the uncollimated transmission source (UTS) for Data Sets 3.*

DSD (cm)	Avg
20	0.142
40	0.143
60	0.143
80	0.143

TABLE B4: *The attenuation coefficient values (cm^{-1}) as a function of detector source distances (DSD) for a detector phantom distance of 20 cm for the collimated transmission source (CTS) for Data Sets 1.*

DSD (cm)	Avg	Stdev	% Stdev
20	0.170	0.001	0.736
40	0.170	0.001	0.678
60	0.170	0.001	0.339
80	0.170	0.000	0.291

TABLE B5: *The attenuation coefficient values (cm^{-1}) at a detector phantom distance (DPD) of 20 cm for a detector source distance of 80 cm for the collimated transmission source (CTS) for Data Sets 2.*

DPD (cm)	Avg	Stdev	% Stdev
20	0.170	0.000	0.291

TABLE B6: *The attenuation coefficient values (cm^{-1}) as a function of detector source distances (DSD) for a source phantom distance of 0 cm for the collimated transmission source (CTS) for Data Sets 3.*

DSD (cm)	Avg	Stdev	% Stdev
20	0.170	0.001	0.736
40	0.170	0.001	0.678
60	0.170	0.001	0.339
80	0.170	0.000	0.291

APPENDIX C

Resolution results obtained with an uncollimated transmission source (UTS) and a collimated transmission source (CTS) obtained for transmission images acquired using a 2 mm thick lead strip. Average (Avg) and standard deviation (Stdev) for the full width half maximum (FWHM) and full width tenth maximum (FHTM) for 3 measurements are given for the uncollimated transmission source (Table C1) and the collimated transmission source (Table C2) for different detector source distances (DSD) with no scatter medium as well as with scatter medium placed between the detector and the transmission source.

TABLE C1: *Resolution results with an uncollimated transmission source (UTS) obtained for transmission images acquired using a 2 mm thick lead strip. The FWHM and FHTM values are shown for different detector source distances (DSD) with no scatter medium as well as with scatter medium placed between the detector and the transmission source.*

Uncollimated transmission source

	No scatter medium						**With scatter medium**					
	FWHM (mm)			**FWTM (mm)**			**FWHM (mm)**			**FWTM (mm)**		
	1	**10**	**18**	**1**	**10**	**18**	**1**	**10**	**18**	**1**	**10**	**18**
DSD (cm)												
20	8.8	12	16.4	15.9	21.8	29.8	8.8	12.7	18.2	16.0	23.1	33.0
40	8.7	12.2	16.1	15.8	22.2	29.4	8.8	12.1	17.4	16.0	22.0	31.6
60	8.8	11.9	16.1	16	21.8	29.3	8.8	12.2	16.5	16.1	22.2	30.1
80	8.7	11.9	15.7	15.9	21.7	28.8	8.8	12.2	16.3	16.1	22.1	29.6
	8.8	12.0	16.1	15.9	21.9	29.3	8.8	12.3	17.1	16.1	22.4	31.1
	0.1	0.1	0.3	0.1	0.2	0.4	0.0	0.3	0.9	0.1	0.5	1.5

TABLE C2: *Resolution results with an collimated transmission source (CTS) obtained for transmission images acquired using a 2 mm thick lead strip. The FWHM and FHTM values are shown for different detector source distances (DSD) with no scatter medium as well as with scatter medium placed between the detector and the transmission source.*

Collimated transmission source

(Lead sheet at 10cm from detector)

	No scatter medium		**With scatter medium**	
	FWHM (mm)	**FWTM (mm)**	**FWHM (mm)**	**FWTM (mm)**
m)				
20	11	20	11.2	20.4
40	10.9	19.8	11.5	20.8
60	10.9	20	11.3	20.6
80	10.9	19.8	11.4	20.8
	10.9	19.9	11.4	20.7
	0.0	0.1	0.1	0.2

APPENDIX D

Triple Energy Window (TEW) estimated Scatter Percentages (%Sc) calculated for different subtraction factors (K) in the 20% energy window for Data Set 1 for the uncollimated transmission source for various detector source distances (DSD) for thicknesses of Perspex (0 – 20 cm). The average and standard deviation (Stdev) for 3 measurements are given for K= 0.5 (Table D1) and K = 1.0 (Table D2).

TABLE D1: *TEW estimated Scatter Percentages (%Sc) calculated for subtraction factor K=1.0 in the 20% energy window for Data Set 1 for the uncollimated transmission source for various detector source distances (DSD) for thicknesses of Perspex (0 – 20 cm) was calculated as the ratio of scattered to total counts and expressed as a percentage.*

DSD (cm)	20		40		60		80	
Thickness (cm)	**%Sc**	**Stdev**	**%Sc**	**Stdev**	**%Sc**	**Stdev**	**%Sc**	**Stdev**
1.1	21.3	1.1	5.8	0.3	5.4	0.6	5.5	1.0
3.2	34.7	1.5	6.5	0.3	5.5	0.7	5.6	1.0
5.4	41.0	1.4	7.3	0.3	5.8	0.7	5.6	1.0
7.5	44.5	1.6	8.2	0.2	6.0	0.6	5.7	1.0
9.6	47.2	2.1	9.3	0.4	6.4	0.7	6.0	1.0
11.8	48.5	2.2	10.5	0.2	6.8	0.7	6.3	0.9
13.9	51.2	2.3	11.6	0.2	7.3	0.7	6.5	1.0
16.1	52.8	2.2	12.8	0.2	7.9	0.6	7.0	1.1
18.2	54.2	2.9	13.8	0.2	8.2	0.7	7.3	1.0
20.3	55.1	2.5	15.0	0.4	9.0	0.5	7.4	0.7

TABLE D2: *TEW estimated Scatter Percentages (%Sc) calculated for subtraction factor K=0.5 in the 20% energy window for Data Set 1 for the uncollimated transmission source for various detector source distances (DSD) for thicknesses of Perspex (0 – 20 cm) was calculated as the ratio of scattered to total counts and expressed as a percentage*

DSD (cm)	20		40		60		80	
Thickness (cm)								
1.1	10.7	0.5	2.9	0.1	2.3	0.3	2.7	0.5
3.2	17.4	0.7	3.2	0.2	2.4	0.3	2.8	0.5
5.4	20.5	0.7	3.6	0.2	2.5	0.3	2.8	0.5
7.5	22.2	0.8	4.1	0.1	2.7	0.3	2.9	0.5
9.6	23.6	1.1	4.6	0.2	2.8	0.4	3.0	0.5
11.8	24.3	1.1	5.2	0.1	3.0	0.3	3.1	0.4
13.9	25.6	1.1	5.8	0.1	3.2	0.4	3.2	0.5
16.1	26.4	1.1	6.4	0.1	3.6	0.3	3.5	0.5
18.2	27.1	1.4	6.9	0.1	3.8	0.3	3.7	0.5
20.3	27.5	1.2	7.5	0.2	4.2	0.3	3.7	0.3

APPENDIX E

Photon Energy Recovery (PER) estimated scatter percentages (%Sc) calculated for different pre-selected sub-energy windows (W) for a 20% energy window for the uncollimated transmission source for various detector source distances for different thicknesses of Perspex (0 – 20 cm). The average and standard deviation (Stdev) for 3 measurements are given for W= 52 (Table E1), W = 9 (Table E2) and W = 3 (Table E3).

TABLE E1: *PER estimated Scatter Percentages (%Sc) calculated for 52 sub-energy windows in the 20% energy window for Data Set 1 for the uncollimated transmission source for various detector source distances (DSD) for thicknesses of Perspex (0 – 20 cm) was calculated as the ratio of scattered to total counts and expressed as a percentage.*

DSD (cm)	20		40		60		80	
Thickness (cm)	**%Sc**	**Stdev**	**%Sc**	**Stdev**	**%Sc**	**Stdev**	**%Sc**	**Stdev**
1.1	11.7	1.2	8.2	3.4	2.0	1.4	1.5	2.9
3.2	21.1	1.6	12.0	7.2	2.3	1.3	1.8	3.3
5.4	25.1	1.7	14.5	8.5	2.7	0.8	1.9	3.6
7.5	29.3	2.1	17.3	10.0	3.5	0.9	1.4	2.6
9.6	33.7	0.8	20.4	13.6	4.0	2.0	1.4	2.6
11.8	37.0	1.8	22.5	12.7	3.7	1.2	2.3	4.2
13.9	37.4	1.1	23.1	14.0	4.6	2.6	2.8	5.0
16.1	37.9	0.5	23.4	14.2	3.6	0.9	2.0	3.5
18.2	39.3	3.2	23.9	13.4	5.0	3.7	2.0	2.9
20.3	42.0	2.7	24.8	15.1	6.1	3.8	7.9	3.6

TABLE E2: *PER estimated Scatter Percentages (%Sc) calculated for 9 sub-energy windows in the 20% energy window for Data Set 1 for the uncollimated transmission source for various detector source distances (DSD) for thicknesses of Perspex (0 – 20 cm) was calculated as the ratio of scattered to total counts and expressed as a percentage*

DSD (cm)	20		40		60		80	
Thickness (cm)	**%Sc**	**Stdev**	**%Sc**	**Stdev**	**%Sc**	**Stdev**	**%Sc**	**Stdev**
1.1	10.1	1.1	6.6	3.0	1.7	0.8	1.1	2.1
3.2	18.9	1.2	10.5	6.8	1.8	0.6	1.2	2.3
5.4	23.7	1.6	13.3	8.6	2.3	0.1	1.3	2.3
7.5	27.6	1.1	15.8	10.5	2.7	0.2	1.0	1.9
9.6	31.2	0.3	19.0	12.2	3.0	1.4	1.0	1.8
11.8	33.4	0.3	19.9	14.0	2.7	0.4	1.7	3.1
13.9	34.7	0.4	22.2	12.2	3.5	1.2	2.0	3.1
16.1	36.0	1.2	22.2	14.1	3.5	0.6	1.8	2.5
18.2	36.6	2.6	22.2	12.4	5.1	4.6	2.1	1.9
20.3	40.1	3.6	26.9	15.0	4.1	2.1	3.9	0.8

TABLE E3: *PER estimated Scatter Percentages (%Sc) calculated for 3 sub-energy windows in the 20% energy window for Data Set 1 for the uncollimated transmission source for various detector source distances (DSD) for thicknesses of Perspex (0 – 20 cm) was calculated as the ratio of scattered to total counts and expressed as a percentage*

DSD (cm)	**20**		**40**		**60**		**80**	
Thickness (cm)	**%Sc**	**Stdev**	**%Sc**	**Stdev**	**%Sc**	**Stdev**	**%Sc**	**Stdev**
1.1	13.0	0.4	10.3	2.1	8.0	0.7	7.1	1.2
3.2	19.8	0.5	13.2	5.6	8.0	0.5	7.2	1.2
5.4	23.6	0.6	15.1	7.6	8.1	0.3	7.0	1.0
7.5	26.2	0.6	16.5	8.9	8.0	0.4	7.0	1.2
9.6	27.8	0.5	17.5	9.8	8.1	0.4	7.2	0.9
11.8	28.9	0.4	18.3	10.2	8.4	0.5	7.4	1.1
13.9	29.9	0.3	19.2	10.6	8.3	0.2	7.7	0.7
16.1	30.2	0.3	19.6	10.6	8.6	0.3	7.9	0.6
18.2	30.7	0.7	20.0	10.5	8.7	0.4	8.3	0.7
20.3	30.8	0.5	20.3	10.4	8.9	0.1	8.9	0.3

APPENDIX F

The Triple Energy Window (TEW) estimated attenuation coefficient values as a function of detector source distances (DSD) calculated for different subtraction factors (K) for a detector phantom distance of 20 cm for the uncollimated transmission source (UTS) for Data Set 1. The average (Avg) and standard deviation (Stdev) for 3 measurements are given for K= 0.5 (Table F1) and K = 1.0 (Table F2).

TABLE F1: *The TEW estimated attenuation coefficient values (cm^{-1}) calculated for the subtraction factor K=0.5 as a function of detector source distances (DSD) for a detector phantom distance of 20 cm for the uncollimated transmission source (UTS) for Data Sets 1.*

DSD (cm)	Avg	Stdev	% Stdev
20	0.155	0.002	1.494
40	0.163	0.003	1.623
60	0.168	0.002	1.241
80	0.170	0.004	2.376

TABLE F2: *The TEW estimated attenuation coefficient values (cm^{-1}) calculated for the subtraction factor K=1.0 as a function of detector source distances (DSD) for a detector phantom distance of 20 cm for the uncollimated transmission source (UTS) for Data Sets 1.*

DPD (cm)	Avg	Stdev	% Stdev
20	0.166	0.001	0.754
40	0.167	0.001	0.691
60	0.170	0.001	0.340
80	0.171	0.001	0.289

APPENDIX G

The Photon Energy Recovery (PER) estimated attenuation coefficient values as a function of detector source distances (DSD) calculated for different pre-selected sub-energy windows (W) for a detector phantom distance of 20 cm for the uncollimated transmission source (UTS) for Data Set 1. The average (Avg) and standard deviation (Stdev) for 3 measurements are given for W= 52 (Table G1), W = 9 (Table G2) and W = 3 (Table G3).

TABLE G1: *The PER estimated attenuation coefficient values (cm^{-1}) as a function of detector source distances (DSD) for a detector phantom distance of 20 cm for the uncollimated transmission source (UTS) for Data Sets 1 calculated for 52 pre-selected sub-energy windows.*

DSD (cm)	Avg	Stdev	% Stdev
20	0.166	0.004	2.40
40	0.164	0.003	1.83
60	0.169	0.004	2.37
80	0.173	0.008	4.62

TABLE G2: *The PER estimated attenuation coefficient values (cm^{-1}) as a function of detector source distances (DSD) for a detector phantom distance of 20 cm for the uncollimated transmission source (UTS) for Data Sets 1 calculated for 9 pre-selected sub-energy windows.*

DPD (cm)	Avg	Stdev	% Stdev
20	0.165	0.004	2.42
40	0.165	0.003	1.81
60	0.169	0.004	2.36
80	0.170	0.005	2.94

TABLE G3: *The PER estimated attenuation coefficient values (cm^{-1}) as a function of detector source distances (DSD) for a detector phantom distance of 20 cm for the uncollimated transmission source (UTS) for Data Sets 1 calculated for 3 pre-selected sub-energy windows.*

DPD (cm)	Avg	Stdev	% Stdev
20	0.150	0.003	2.00
40	0.158	0.005	3.16
60	0.167	0.003	1.80
80	0.170	0.004	2.35

Abstract

Several factors influence the quality of Single Photon Emission Tomography (SPECT) images. The most prominent of these are the effect of tissue attenuation and scatter. Attenuation may lead to artefacts and quantitative inaccuracies in reconstructed images. These occurrences are particularly disturbing in clinical studies such as myocardial perfusion imaging because of the highly non-uniform composition of tissue in the thorax region. The importance of accurate compensation for attenuation effects in SPECT is already widely recognized and several studies have demonstrated that image quality can be improved by incorporating attenuation correction into an iterative reconstruction method. *The aim of this study was the production and evaluation of an uncollimated printed transmission flood source along with a scatter correction for transmission imaging in nuclear medicine.*

In this study a transmission flood source was designed and produced in-house by depositing a mixture of radioactive ink on a paper with a digital inkjet printer. The production process of the transmission source was evaluated by determining the reproducibility and image quality of the printed radioactive source. Planar transmission imaging was performed by using the in-house printed transmission source and a gamma camera. From the results obtained with the uncollimated transmission flood source, the estimated scatter percentages indicated that the scatter contribution in the acquired energy spectra increased with a decrease in the detector source distance. It was shown that for the smallest possible detector phantom distance, the scattered photons in the acquired transmission image was limited at detector source distances greater than 60 cm. At detector source distances greater than 60 cm the attenuation coefficient values obtained for the uncollimated transmission source compared favourable to the attenuation coefficient values obtained with a collimated transmission source. It is also clear from these results that transmission imaging with an uncollimated transmission source at detector source distances of less than 60 cm would result in an underestimation of the attenuation coefficient values. An underestimation of the attenuation coefficient values can result in an overestimation of activity during emission image quantification. By applying a modified version of the triple energy scatter correction to the transmission images acquired with the uncollimated printed

transmission source the scattered photons were successfully removed from the transmission images. The attenuation coefficient values obtained from these scatter corrected planar transmission images compared favourable to the attenuation coefficient values obtained with a collimated transmission source.

Finally the feasibility to perform transmission computed tomography by using an uncollimated non-uniform printed flood source along with a SPECT gamma camera was evaluated. From the results obtained it was clear that the tomographic resolution was dependant on the distance of the acquisition detector from the phantom. The attenuation coefficient values that were obtained from the reconstructed transmission images were lower than the value reported in the literature. The underestimation of the attenuation coefficient values were corrected for by applying the modified triple energy window scatter correction to the acquired transmission images.

This study showed that accurate attenuation coefficient values could be obtained using an uncollimated non-uniform printed transmission source along with an appropriate scatter correction. These attenuation coefficient values were obtained from TCT imaging with the printed uncollimated flood source with no gamma camera modifications.

Radioactive
Transmission
Emission
Scatter correction
Attenuation coefficient
Single Photon Emission Computed Tomography
Triple Energy Window
Photon Energy Recovery

Abstrak

Verskeie faktore beïnvloed die gehalte van Gerekenariseerde Enkel Foton Emissie Tomografie (GEFET) beelde. Die duidelikste van hierdie effekte is die effek van die weefsel attenuasie en foton verstrooiïng. Attenuasie kan lei tot artefakte en kwantitatiewe foute in gerekonstrueerde beelde. Die voorkomste van hierdie artefakte is veral beduidend in kliniese studies soos miokardiale perfusie beelding as gevolg van die nie-uniforme samestelling van die weefsel in die toraks area. Die belangrikheid van akkurate kompensasie vir attenuasie defekte in GEFET is wyd bekend en verskeie studies het getoon dat beeld kwaliteit verbeter kan word deur die integrasie van attenuasie korreksie in 'n iteratiewe rekonstruksie metode. *Die doel van hierdie studie was die produksie en evaluering van 'n ongekollimeerde gedrukte transmissie vloed bron tesame met ‘n verstrooïngskorreksie vir transmissie beelding in kerngeneeskunde.*

In hierdie studie is 'n transmissie vloed bron ontwerp en in-huis vervaardig deur die deponering van' n mengsel van radioaktiewe ink op 'n papier met behulp van 'n digitale inkspuit drukker. Die produksie proses van die gedrukte radioaktiewe bronne is geëvalueer deur die herbaarheid en die beeld kwaliteit van die bronne te bepaal. Planare transmissie beelding is uitgevoer deur gebruik te maak van die in-huis gedrukte transmissie bron en 'n gamma-kamera. Uit die resultate wat verkry is met die ongekollimeerde transmissie vloed bron kan gesien word dat die geskatte verstrooiïngs persentasies die verstrooiïngs bydrae in die versamelde energie spektra verhoog met 'n afname in die detektor bron afstand. Daar is ook aangetoon dat vir die kleinste moontlike detektor fantoom afstand, die verstrooide fotone in die transmissie beeld beperk was vir detektor bron afstande groter as 60 cm. By detektor bron afstande groter as 60 cm het die attenuasie koëffisiënt waardes vir transmissie beelde wat verkry was met die ongekollimeerde transmissie bron goed vergelyk met die waardes soos verkry met 'n gekollimeerde transmissie bron. Dit is ook duidelik uit hierdie resultate dat transmissie beelding met 'n ongekollimeerde transmissie bron vir detektor bron afstande van kleiner as 60 cm sal lei tot 'n onderskatting van die attenuasie koëffisiënt waardes. 'n Onderskatting van die attenuasie koëffisiënt waardes kan lei tot 'n oorskatting van die radioaktiwiteit in die emissie beeld tydens kwantifisering. Deur die toepassing van die gemodifiseerde weergawe van die drie energie venster verstrooiïngs tegniek

kan die verstrooide fotone suksesvol verwyder word vanaf die transmissie beelde wat opgeneem is met die ongekollimeerde transmissie bron. Die attenuasie koëffisiënt waardes wat verkry is vanaf hierdie verstrooiïngs gekorrigeer planare beelde het goed vergelyk met die attenuasie koëffisiënt waardes soos verkry met 'n gekollimeerde transmissie bron.

Ten slotte is die haalbaarheid van gerekenariseerde transmissie tomografie geëvalueer deur gebruik te maak van 'n ongekollimeerde nie-uniforme gedrukte transmissie bron tesame met 'n GEFET gamma kamera. Uit die resultate wat verkry was is dit duidelik dat die tomografiese resolusie afhanklik is van die afstand van die opname detektor vanaf die fantoom. Die attenuasie koëffisiënt waardes wat verkry is uit die gerekonstrueerde transmissie beelde was laer as die waarde wat in die literatuur gerapporteer is. Hierdie onderskatting van die attenuasie koëffisiënt waardes is gekorrigeer deur die gewysigde drie energie venster verstrooi tegniek toe te pas op die opgeneemde transmissie beelde.

Hierdie studie het getoon dat akkurate attenuasie koëffisiënt waardes verkry kan word met behulp van 'n ongekollimeerde nie-uniforme gedrukte transmissie bron tesame met 'n toepaslike verstrooiïgs tegniek. Akkurate attenuasie koëffisiënt waardes is verkry met behulp van gerekenariseerde transmissie tomografie beelding met die gedrukte ongekollimeerde vloed bron en geen gamma kamera modifikasies.